Phase Diagram and Real-Time Dynamics of the Semiclassical Kondo Lattice on a Zigzag Ladder

Dɪssᴇʀᴛᴀᴛɪᴏɴ

with the aim of achieving a doctoral degree
at the Faculty of Mathematics, Informatics and Natural Sciences
Department of Physics at the University of Hamburg

submitted by

Lena-Marie Woelk

Hamburg, June 2019

Acknowledgements

Abstract

The equilibrium phase diagram of the Kondo lattice model with classical spins on the so-called zigzag ladder, which is a minimal example of frustration in one dimension, is derived as a function of exchange coupling constant J and measure of frustration φ. It is found to contain the well-known antiferromagnetic phase, an incommensurate spiral phase with varying pitch angle, and a novel spin-dimerized phase. The results are compared to perturbation theory in both the strong and weak coupling limit and found to agree well, with the exception of the dimerized phase which is absent in the perturbative approaches. A comparison to results obtained by density-matrix renormalization group (DMRG) reveals many similarities to the quantum-mechanical model. Both models predict the existence of the dimerized phase, whereas the DMRG-phase diagram contains further features absent in the classical approximation.

Next, the real-time dynamics of the system is analyzed following a quench, i.e. a sudden change in parameter. Two qualitatively different energy regions are identified. For low quench energies, the system is non-ergodic and remains in the initial spin configuration for all times. The corresponding energy threshold is reminiscent of the Fermi-Pasta-Ulam (FPU) paradox known from classical dynamics. After exploring the (non-)integrability of the model, the ergodicity threshold is explained using a linear approximation in the equations of motion describing spin-wave-like excitations.

For higher quench energies, in particular when crossing the equilibrium phase boundary, the dynamics is ergodic. The time scale of thermalization is found to be highly energy-dependent. Starting from an initial spiral configuration, the gradual emergence of long range dimer order can be seen. Above a certain critical energy, however, this long range dimer order breaks down. This thermal transition is found stable in the limit of larger lattice sizes.

Kurzzusammenfassung

Das Gleichgewichtsphasendiagramm des Kondo Gitter Modells mit klassischen Spins auf der sogenannten Zickzack-Leiter, welche ein Minimalbeispiel für Frustration in einer Dimension ist, wird hergeleitet als Funktion der Austausch Kopplung J und Frustration φ. Es beinhaltet die bekannte antiferromagnetische Phase, eine inkommensurable Spiralphase mit variierendem Winkel und eine neuartige spin-dimerisierte Phase. Die Ergebnisse werden mit Störungstheorie sowohl im Limes starker als auch schwacher Kopplung verglichen und stimmen gut überein, mit Ausnahme der dimerisierten Phase, die von der Störungstheorie nicht beschrieben wird. Anschließend wird das Phasendiagramm verglichen mit Ergebnissen, die mit density-matrix renormalization group (DMRG) berechnet wurden. Es sind viele Gemeinsamkeiten zwischen semiklassischem und quantenmechanischem Modell festzustellen. Beide sagen die dimerisierte Phase vorher, allerdings beinhaltet das DMRG-Phasendiagramm noch andere Phänomene, die in der klassischen Approximation fehlen.

Dann wird die Echtzeitdynamik des Systems nach einem Quench, also der plötzlichen Änderung eines Parameters, analysiert. Es werden zwei qualitativ unterschiedliche Energiebereiche identifiziert. Für Quenches mit niedriger Energie ist das System nicht ergodisch und verbleibt für immer in der Anfangsspinkonfiguration. Die entsprechende Energieschwelle erinnert an das Fermi-Pasta-Ulam (FPU) Paradoxon, bekannt aus der klassischen Dynamik. Nach einer Untersuchung der (Nicht-) Integrabilität des Modells, wird die Ergodizitätsschwelle mithilfe einer linearen Näherung der Bewegungsgleichungen erklärt, die spinwellenartige Anregungen beschreibt.

Für Quenches mit höherer Energie, insbesondere wenn Phasengrenzen überquert werden, ist die Dynamik ergodisch. Die Zeitskala der Thermalisierung ist stark energieabhängig. Ausgehend von einer anfänglichen spiralen Spinordnung kann der graduelle Aufbau einer langreichweitigen Dimerisierungsordnung beobachtet werden. Oberhalb einer kritischen Energie bricht diese Ordnung jedoch zusammen. Dieser thermische Übergang ist stabil im Limes größerer Systeme.

Contents

1. Introduction

1.1. Emergence, Frustration and the Kondo Lattice

Studying a single water molecule does not convey the enormous complexity of the properties of a macroscopic body of water. It cannot be explained by considering solely one oxygen and two hydrogen atoms on their own, that the same lake can be used in summer for swimming and in winter for ice skating. Since John Dalton published his model of the atom as an indivisible entity in 1808 in his work *A New System of Chemical Philosophy*, much has been corrected and by looking closer and closer ever new fundamental particles were discovered. Still, even with all this knowledge, the interplay between many atoms together and the qualities, which result, often remain a mystery. As P.W. Anderson put it so eloquently in his famous 1972 paper *More is different*: "... we can see how the whole becomes not only more than but very different from the sum of its parts." [1]. This phenomenon of simple parts creating a complex reality is in fact very universal and examples can be found almost everywhere in physics, biology and even sociology. Many particles can organize to generate qualitatively different properties, a concept called *emergence*.

Any macroscopic material is composed of an innumerable amount of particles. The main focus of condensed matter physics is understanding the interplay between them and the puzzling properties which emerge as a result. Often, such as in the case of freezing water, this is closely connected to a disorder-to-order transition. A well known example is the magnetic phase, which appears when a paramagnetic metal is cooled down until the previously present spin-rotational symmetry is spontaneously broken, and all spins align to form, e.g., a ferromagnetic state. There are countless more examples of peculiar properties of matter arising as the result of correlated electrons - other ordered states such as superconductivity [2], disordered spin liquids [3] or, well in focus recently, topological insulators [4]. The intricate knowledge of electronic and magnetic phases of matter, and of the interactions and behavior of the constituents that make up materials is not of purely academic interest. With the rise of the digital age comes an increasing dependence on faster and more advanced computer processing and memory technology, which in turn relies heavily on new insights from condensed matter research.

One of the remarkable features of emergence is that the same simple particles can give rise to very different phenomena when put in different conditions. One of these special environments is in the focus of this thesis. The origins lie in 1950, when Gregory Wannier considered a peculiar system which

should prove to set a new direction - the so-called Ising model arranged in triangle and honeycomb structures [5]. Some years later, in 1959, there were several independent works on non-collinear vector spins subject to competing interactions studied by Yoshimori [6], Villain [7] and Kaplan [8], which further cemented the start of the extensive new research area of *frustrated spin systems*. These are particularly intriguing, as the inability of the system to satisfy competing interactions often results in the emergence of unconventional states of matter. Consider for example spins coupled by an antiferromagnetic nearest-neighbor exchange interaction, which would ideally like to anti-align. In Fig. 1.1 this situation is sketched on two different lattice geometries. If the lattice is bipartite, i.e. can be split into two disjoint sublattices, such that any neighbor resides in the other sublattice, as shown on the left in Fig. 1.1, then this is easily resolved and the well known antiferromagnetic order appears. If there is a triangle involved, however, as on the right hand side of Fig. 1.1, it is not possible to satisfy each pair of spins and anti-align them all. Evidently, there must be a compromise emerging that could lead to unexpected behavior.
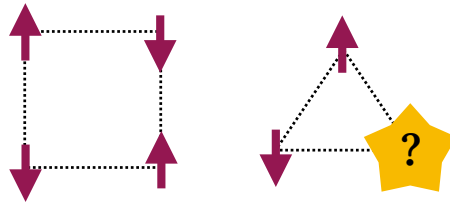
Figure 1.1.: Schematic picture of geometric frustration. The left picture shows an antiferromagnetic alignment of spins on the bipartite square lattice, which produces no frustration of the interactions. On the right hand side, on the contrary, a triangle is shown that does not allow for an unambiguous antiferromagnetic ground state.

Frustrated spin systems come in many different variants. The model considered in this thesis is the Kondo lattice model, which, quite generally and independent on the specific geometry, is a two orbital model describing the coupling and interplay between magnetic and fermionic degrees of freedom and can be applied to many different materials. If the localized magnetic moments are considered as classical spins, such as the case here, the Kondo lattice can for example describe the physics of transition metal oxides such as $LaMnO_3$, which are most famous for exhibiting the colossal magnetoresistance (CMR) effect. This context has stimulated much research in the last decades [9–12]. Recently, there has also been interest in the Kondo lattice on frustrated geometries, both theoretical [13–18] and experimental [19]. A more detailed introduction to the Kondo lattice model and its applications is given later.

One of the central goals here is to derive and understand the ground state phase diagram of the Kondo lattice with classical spins on a frustrated zigzag ladder. It turns out to contain a spin-dimerized phase

that is absent in the unfrustrated case and agrees well with results for the model variant with quantum spins 1/2 obtained by M. Peschke using the density-matrix renormalization group (DMRG) method [20,21]. This comparison of the classical-spin Kondo lattice with the quantum analogue is found highly instructive. Also very instructive are several perturbative approaches which describe the system well in both the weak and strong coupling regime, with the exception of the dimerized phase that appears to be a non-perturbative phenomenon.

1.2. Moving on: Dynamics and Dynamical Phase Transitions

There is a big advantage of the semiclassical Kondo lattice as compared to the quantum-spin variant. Namely, the real-time dynamics of a given microstate can be traced on time scales that are orders of magnitude larger - hence, a second main goal of this thesis is to explore the dynamical behavior of the system. This goal is in turn split into more general considerations of the nature of the dynamics and the search for a thermal phase transition of the dimerized phase, i.e. understanding a thermodynamical phase transition via real-time dynamics.

To describe the physics of the many, it is often neither possible nor necessary to keep track of every single particle. The great success of statistical mechanics as developed by James Clerk Maxwell, Ludwig Boltzmann and Josiah Willard Gibbs, is the ability to describe equilibrium properties of macroscopic systems using only elements of probability theory. If the premise is still that every particle on its own follows some (perhaps unknown) deterministic equations of motion, there must, however, be a connection between the two viewpoints. Lately, there has been more focus again on dynamical theories and experiments: With the advent of optical lattices, there is now an unprecedented measure of control of model systems out of equilibrium that has been hugely successful for many different systems [22]. After many theoretical considerations [23–25] and preliminary studies [26,27] an optical lattice that closely resembles a Kondo lattice was recently realized experimentally using ^{173}Yb to create a two-orbital fermionic quantum gas [28]. This undoubtedly opens the door for many more studies to come.

These advances in experiment have already triggered many theoretical studies on the topic of non-equilibrium. In addition to the dynamics of classical systems, new questions have started to arise. One is thermalization, i.e. dynamically approaching equilibrium, in isolated quantum systems [29,30]. A second one is *dynamical phase transitions*, a term that was coined to describe phase transitions, where instead of in the free energy, the non-analyticities are found as a function of time and where the role of temperature which drives the change of state in a classical thermal phase transition is replaced by some external system parameter [31–33]. Another focus has recently been on the behavior of systems in the vicinity of an integrable point in parameter space, which has introduced new concepts such as prethermalization [34,35].

Many open questions still remain. The mechanism of thermalization in isolated systems both close to

and far from integrability is not understood beyond a doubt [30]. New dynamical phenomena emerge constantly, for example the existence of (meta)-stable non-equilibrium states that have no equivalent in equilibrium theory and which pose new questions that are far from being answered [36]. Also still unclear is the fundamental connection between statistical physics and dynamical theory. If statistical mechanics describes the physics of the many in thermal equilibrium in terms of state variables, while dynamical theory, on the other hand, describes the time propagation of a many-body microstate, then thermodynamics must be reducible to real-time dynamics for systems that are large enough. Exactly how many degrees of freedom are needed for statistical behavior, however, remains elusive.

One idea is to discuss if the criteria for ergodicity apply to the present model. It is found, in fact, that chaotic motion is apparently not as inevitable as expected. Another one is to investigate the possible proximity to an integrable model and to derive a linear theory of spin-wave-like excitations. Studying whether the dimerized phase found in the equilibrium phase diagram is stable against thermal fluctuations is a concrete question to be answered using the real-time dynamics approach. This is tackled with the method of quenching a system parameter, a similarity shared with the previously mentioned dynamical phase transitions known from the quantum-mechanical context [31–33]. Even though here, the transition is *thermal* and thus classical, it could still be called *dynamical* in the sense that long range (dimer) order is gradually emerging from real time dynamics.

2. The Kondo Lattice

This chapter introduces the main model used in this thesis: the Kondo lattice model. First, the model is motivated and the notation introduced in Section 2.1. Then, the geometry of the zigzag ladder is explained. Depending on the model parameters, different spin configurations minimize the total energy. In short, there are two possibilities - either the equilibrium spin configuration can be described by a constant pitch angle between neighboring spins, or the configuration is *dimerized* and requires two angles to characterize the configuration. Fixing the spin configuration with at most two parameters evidently reduces the problem enormously, and a transformation into k-space can be used to simplify even further. This is shown in Section 2.2 for both the homogenous spiral and dimerized case.

This chapter concludes with the presentation of two perturbative approaches. The weak coupling limit, i.e. the well-known RKKY model, is derived in Section 2.3.1. In addition, the strong coupling limit, which can also be mapped onto an effective spin-only theory - in this case the $J_1 - J_2$-Heisenberg model, is derived in Section 2.3.2.

2.1. Introduction to the Kondo Lattice Model

Electrons in an elemental solid occupy orbitals or bands according to the position in the periodic table. Generally speaking, electrons in a partially filled d-band tend to be itinerant, whereas electrons occupying an f-orbital are localized. In transition metals, itinerant electrons contribute to the metallic or even superconducting properties of a compound, while localized electrons form local magnetic moments. Materials with well-formed local moments are, as P. Coleman puts it, *on the brink of magnetism* [37].

A model that describes the interplay between local magnetic moments and itinerant conduction electrons is called the *Kondo lattice model* with one conduction electron orbital and one localized spin per lattice site. Historically, this is the dense version of the *Kondo model*, an impurity model that captures the physics of the *Kondo effect*, where a localized magnetic impurity acts as a resonant scattering potential for the electron fluid which increases the resistivity. The Kondo and the Kondo lattice model can be derived via a so-called Schrieffer-Wolff transformation from the more general Anderson impurity or periodic Anderson model, respectively [38]. The physics of the so-called *heavy-fermion* materials described by the Kondo lattice model is usually dominated by a competition between the Kondo effect

and a low-energy effective spin-spin coupling caused by the so-called *RKKY* interaction. In some materials, however, the f-electrons are in fact so close to the nuclear core that multiple electrons may form a total spin of length $\gg \frac{1}{2}$ and can thus be approximated by a classical vector - a "classical spin". In this case, the Kondo effect - being a purely quantum phenomenon - does not play a role, but other interesting physics arises. This describes for example the entire class of Manganites which exhibit effects such as *colossal magnetoresistance*. More on them and on other heavy fermion or mixed valence materials can be found e.g. in [9,37,39]. This thesis concentrates on the model with a classical approximation of the localized moments.

The Hamiltonian of the Kondo lattice model is given by

$$H = \sum_{ij\sigma} t_{ij} c_{i\sigma}^\dagger c_{j\sigma} + J \sum_i \mathbf{S}_i \cdot \mathbf{s}_i, \tag{2.1}$$

where $c_{i\sigma}^\dagger (c_{i\sigma})$ creates (annihilates) an electron at site $i = 1, ..., L$ with spin projection $\sigma = \uparrow, \downarrow$ and

$$\mathbf{s}_i = \frac{1}{2} \sum_{\sigma\sigma'} c_{i\sigma}^\dagger \boldsymbol{\sigma}_{\sigma\sigma'} c_{i\sigma'} \tag{2.2}$$

is the local conduction-electron spin at site i, where $\boldsymbol{\sigma}$ denotes the vector of Pauli matrices. The local spin $\mathbf{s}_i$ couples antiferromagnetically to the localized spin $\mathbf{S}_i$ at the same site via exchange coupling constant $J > 0$. Here, as mentioned, the localized spins $\mathbf{S}_i$ are taken to be classical vectors of fixed length $|\mathbf{S}_i| = 1/2$. The first term of Eq. (2.1) describes the hopping of the electrons with hopping amplitudes t_{ij} between sites i and j.

For classical spins $\mathbf{S}_i$, the Hamiltonian Eq. (2.1) is effectively bilinear and can be expressed using an effective hopping matrix $\mathbf{t}_{\text{eff}}$:

$$H = \sum_{ii'\sigma\sigma'} t_{\text{eff},ii'\sigma\sigma'} c_{i\sigma}^\dagger c_{i'\sigma'} \tag{2.3}$$

with elements

$$t_{\text{eff},ii'\sigma\sigma'} = t_{ii'} \delta_{\sigma\sigma'} + \frac{J}{2} (\boldsymbol{\sigma} \mathbf{S}_i)_{\sigma\sigma'} \delta_{ii'}. \tag{2.4}$$

The total energy of the system is a functional of the classical spin configuration $\{\mathbf{S}\} = (\mathbf{S}_1, ..., \mathbf{S}_L)$:

$$E(\{\mathbf{S}\}) = \sum_{ii'\sigma\sigma'} \left(t_{ii'} \delta_{\sigma\sigma'} + \frac{J}{2} (\boldsymbol{\sigma} \mathbf{S}_i)_{\sigma\sigma'} \delta_{ii'} \right) \langle c_{i\sigma}^\dagger c_{i'\sigma'} \rangle_{\{\mathbf{S}\}} \tag{2.5}$$

It is convenient to introduce the $2L \times 2L$ one-particle reduced density matrix ρ with elements

$$\rho_{ii'\sigma\sigma'} \equiv \langle c^\dagger_{i'\sigma'} c_{i\sigma} \rangle, \qquad (2.6)$$

which for the ground state is obtained by diagonalizing the effective hopping matrix Eq. (2.4) $\mathbf{t}_{\text{eff}} = \mathbf{U}\epsilon\mathbf{U}^\dagger$ for the given spin configuration and taking $\boldsymbol{\rho} = \Theta(-\mathbf{t}_{\text{eff}}) = \mathbf{U}\Theta(-\epsilon)\mathbf{U}^\dagger$, where Θ is the Heaviside step function.

2.2. Equilibrium Spin Configurations on the Zigzag Ladder

Much attention has been given in recent years to the study of frustrated spin systems. A system is called *frustrated*, whenever there are competing interactions acting on the spins and the lattice geometry does not allow to satisfy all bonds simultaneously, i.e. the ground state does not correspond to the minimum of each pair of spins. Besides there being many experimental examples of magnetic materials exhibiting frustration (see for example [???]), frustrated systems are also highly interesting model systems that often display unconventional states of matter. Frustration induced by geometry is present whenever the lattice structure includes elementary triangles, such as the 2D triangular and Kagome lattice. There are already a few works on the Kondo lattice with classical spins on such geometries, see for example [17,40,41]. The simplest model possible to exhibit frustration, however, is the zigzag ladder. The zigzag ladder is, despite including elementary triangles, strictly speaking a one-dimensional model, since it can be mapped exactly on the one-dimensional chain with both nearest and next-to-nearest neighbor interactions. Both the zigzag ladder geometry as well as the equivalent one-dimensional chain are illustrated in Fig. 2.1.
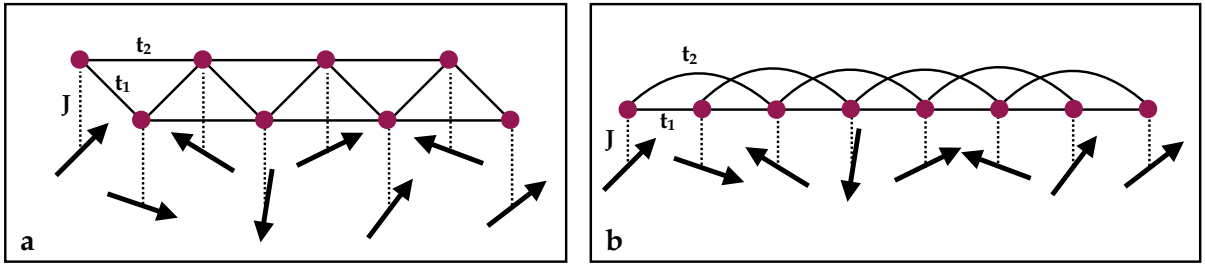
Figure 2.1.: (a) Kondo lattice with classical spins on a zigzag ladder with hopping $-t_1$ on the rungs and $-t_2$ on the legs of the ladder ($t_1, t_2 > 0$). This is equivalent to (b), a one-dimensional chain with nearest neighbor hopping $-t_1$ and next-to-nearest neighbor hopping $-t_2$. In both cases, classical spins are coupled locally to electrons via exchange coupling constant J.

The hopping amplitude is $-t_1$ between nearest neighbors and $-t_2$ between next-to-nearest neighbors, i.e. on rungs and legs of the zigzag ladder, respectively. Electrons are coupled locally to a classical spin via an antiferromagnetic exchange coupling constant $J > 0$. To better quantify the measure of

frustration in the system, a parameterization of hopping amplitudes $t_1 = t \cos \varphi$ and $t_2 = t \sin \varphi$ is introduced with t fixed at $t \equiv 1$. Evidently, the limits $\varphi = 0$ and $\varphi = \pi/2$ describe the unfrustrated limit of one, or, in the case of $\varphi = \pi/2$, two decoupled chains with nearest neighbor exchange only. Within this thesis, the lattice is always considered to be at half-filling, i.e. one electron per site i on average. Additionally, periodic boundary conditions are always assumed.

The length of the classical spins $|\mathbf{S}|$ is constant and kept at $|\mathbf{S}| = \frac{1}{2}$ throughout this work, but the orientation of the spins is of course a priori arbitrary. There are therefore $2L$ parameters of the spin configuration, i.e. the polar and azimuthal angles of each spin $\{\phi_i, \theta_i\}$, where both ϕ_i and θ_i are continuous variables with $\phi_i \in [0, 2\pi)$ and $\theta_i \in [0, \pi]$. This leaves infinitely many possible configurations and renders a simple minimization of the energy functional Eq. (2.5) nearly impossible. Knowing, however, the ground state of the Heisenberg model with classical spins on the zigzag ladder (see Appendix A), an Ansatz can be made that greatly simplifies the task. Considering that frustration of this type often leads to a spiral spin order [42], it is not far-fetched to consider a parameterization with a constant pitch angle θ between spins as a possible ground state configuration. Both ferro- and antiferromagnetic order is included in this parameterization with $\theta = 0$ and $\theta = \pi$. As an extension, here, the parameterization will additionally include the possibility of a modulation $\Delta\theta$. As pictured in Fig. 2.2, the angle between nearest neighbor spins then alternates between $\theta + \Delta\theta$ and $\theta - \Delta\theta$ with $\Delta\theta = 0$ returning the original constant angle configuration. The entire spin configuration is thus parametrized by two parameters $(\theta, \Delta\theta)$ now allowing for a simple minimization of the energy $E(\{\mathbf{S}\}) \equiv E(\theta, \Delta\theta)$ (Eq. (2.5)). For symmetry reasons it is sufficient to consider $\theta \in [0, \pi]$ and $\Delta\theta \in [0, \pi/2)$ with $\theta = n \cdot 2\pi/L$ ($n \in \mathbb{N}$) to satisfy periodic boundary conditions. Spin configurations with $\Delta\theta \neq 0$ are termed *dimerized*.
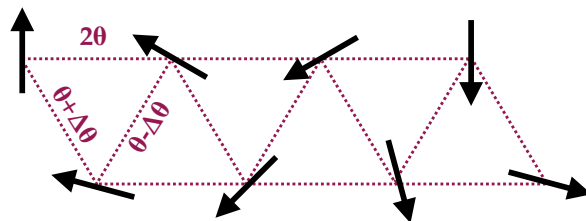
Figure 2.2.: Parameterization of spin configurations on the zigzag ladder, where the angle between nearest neighbors is alternating between $\theta \pm \Delta\theta$ and the angle between next-to-nearest neighbors is 2θ.

2.2.1. Spin Configurations With Constant Pitch Angle

Replacing the $2L$ parameters $\{\phi_i, \theta_i\}$ with only two, i.e. θ and $\Delta\theta$, evidently significantly reduces the complexity of the model. Translational invariance can be exploited to further simplify the calculation of the energy, as will be shown in this section. For the moment, only spin configurations with a constant

pitch angle θ between neighboring spins will be considered. As the model used in this thesis is one-dimensional, most calculations will reflect this, and the one-dimensional 'vectors' are not printed in bold.

While the $2L \times 2L$ dimensional effective hopping matrix in Eq. (2.4) can certainly be diagonalized numerically for finite lattice sizes, it is not possible to do so analytically for arbitrary spin configurations. The hopping term alone, however, is diagonalized by a simple Fourier transform

$$H_{\text{hopp}} = \sum_{ij\sigma} t_{ij} c_{i\sigma}^{\dagger} c_{j\sigma} = \sum_{k\sigma} \varepsilon(k) c_{k\sigma}^{\dagger} c_{k\sigma} \tag{2.7}$$

where

$$\varepsilon(k) = -2t_1 \cos(k) - 2t_2 \cos(2k) \tag{2.8}$$

is the dispersion relation and the Fourier transform is defined as

$$c_{i\sigma}^{\dagger} = \frac{1}{\sqrt{L}} \sum_{k}^{BZ} e^{-ikr_i} c_{k\sigma}^{\dagger} \tag{2.9}$$

where the sum $\sum_{k}^{BZ}$ runs over the first Brillouin zone and the spacing of the wave vectors k is given by $k = n \cdot \frac{2\pi}{aL}$ with integer n and lattice spacing $a \equiv 1$.

The second term of the Kondo lattice Hamiltonian in Eq. (2.1) describes the interaction between electrons and classical spins and can be written as

$$H_J = J \sum_{i} \mathbf{S}_i \cdot \mathbf{s}_i = \frac{J}{2} \sum_{i\sigma\sigma'} (\boldsymbol{\sigma} \mathbf{S}_i)_{\sigma\sigma'} c_{i\sigma}^{\dagger} c_{i\sigma'}. \tag{2.10}$$

As mentioned, for now, the classical spins $\mathbf{S}_i$ are considered to be in a homogenous spiral spin configuration with wave vector q and taken, without loss of generality, to lie in the $x - y$ plane, i.e.

$$\mathbf{S}_i = S \begin{pmatrix} \cos(q \cdot r_i) \\ \sin(q \cdot r_i) \\ 0 \end{pmatrix}, \tag{2.11}$$

where $S \equiv \frac{1}{2}$ is the length of each classical spin. Multiplied with the vector of Pauli matrices $\boldsymbol{\sigma} = (\sigma^x, \sigma^y, \sigma^z)^T$ this gives

$$\boldsymbol{\sigma} \cdot \mathbf{S}_i = \begin{pmatrix} 0 & \cos(q \cdot r_i) - i \sin(q \cdot r_i) \\ \cos(q \cdot r_i) + i \sin(q \cdot r_i) & 0 \end{pmatrix}$$
$$= \begin{pmatrix} 0 & e^{-iqr_i} \\ e^{iqr_i} & 0 \end{pmatrix}. \tag{2.12}$$

The interaction term (Eq. (2.10)), too, can now be Fourier transformed using the Fourier transform in Eq. (2.9), and becomes

$$\begin{aligned} H_J &= \frac{JS}{2} \sum_i \left(c_{i\uparrow}^\dagger c_{i\downarrow} e^{-iqr_i} + c_{i\downarrow}^\dagger c_{i\uparrow} e^{iqr_i} \right) \\ &= \frac{JS}{2} \frac{1}{L} \sum_i \sum_{kk'} \left(c_{k\uparrow}^\dagger c_{k'\downarrow} e^{-ikr_i} e^{ik'r_i} e^{-iqr_i} \right. \\ &\quad \left. + c_{k\downarrow}^\dagger c_{k'\uparrow} e^{-ikr_i} e^{ik'r_i} e^{iqr_i} \right) \end{aligned} \tag{2.13}$$

where the representation of the Kronecker delta with $k = n \cdot 2\pi/L$ and $k' = m \cdot 2\pi/L$ (n, m integer)

$$\delta_{kk'} = \frac{1}{L} \sum_{j=1}^{L} e^{ir_j(k-k')} \tag{2.14}$$

is used to yield

$$\begin{aligned} H_J &= \frac{JS}{2} \sum_{kk'} \left(c_{k\uparrow}^\dagger c_{k'\downarrow} \delta_{k',k\oplus q} + c_{k\downarrow}^\dagger c_{k'\uparrow} \delta_{k,k'\oplus q} \right) \\ &= \frac{JS}{2} \sum_k \left(c_{k\uparrow}^\dagger c_{k\oplus q\downarrow} + c_{k\oplus q\downarrow}^\dagger c_{k\uparrow} \right). \end{aligned} \tag{2.15}$$

Unlike the case of the hopping term above, the Fourier transform does not diagonalize the interaction Hamiltonian fully, but leaves a 2×2 structure where terms with wave vector k mix with $k \oplus q$, where the latter is understood as $k \oplus q = k + q + G$ with G being a uniquely defined vector of the reciprocal lattice such that $k + q + G \in \text{BZ}$.

Periodicity of the lattice ensures invariance of $\sum_{k\sigma} \varepsilon_k c_{k\sigma}^\dagger c_{k\sigma}$ after a shift with constant vector q. The entire Hamiltonian can thus be expressed in matrix form as

$$H = \sum_k \begin{pmatrix} c_{k\uparrow}^\dagger & c_{k\oplus q\downarrow}^\dagger \end{pmatrix} \begin{pmatrix} \varepsilon_k & \Delta \\ \Delta & \varepsilon_{k\oplus q} \end{pmatrix} \begin{pmatrix} c_{k\uparrow} \\ c_{k\oplus q\downarrow} \end{pmatrix} \tag{2.16}$$

with $\Delta \equiv JS/2 = J/4$. This can now be diagonalized with a so-called Bogoliubov transformation

$$
\begin{aligned}
\alpha_k^\dagger &= u_k c_{k\uparrow}^\dagger + v_k c_{k\oplus q\downarrow}^\dagger \\
\beta_k^\dagger &= -v_k c_{k\uparrow}^\dagger + u_k c_{k\oplus q\downarrow}^\dagger
\end{aligned}
\tag{2.17}
$$

with the condition $u_k^2 + v_k^2 = 1$ to ensure the operators α_k, β_k obey fermionic anticommutation relations. Then

$$
\begin{aligned}
u_k^2 &= \frac{1}{2}\left(1 - \frac{\varepsilon_{k\oplus q} - \varepsilon_k}{\sqrt{(\varepsilon_{k\oplus q} - \varepsilon_k)^2 + \Delta^2}}\right) \\
v_k^2 &= \frac{1}{2}\left(1 + \frac{\varepsilon_{k\oplus q} - \varepsilon_k}{\sqrt{(\varepsilon_{k\oplus q} - \varepsilon_k)^2 + \Delta^2}}\right) \\
u_k v_k &= \frac{\Delta}{2\sqrt{(\varepsilon_{k\oplus q} - \varepsilon_k)^2 + \Delta^2}}
\end{aligned}
\tag{2.18}
$$

follows from the vanishing of the off-diagonal terms of Eq. (2.16) rewritten in terms of α_k, β_k. The diagonal Hamiltonian is now

$$
H = \sum_k \left[E_-(k,q)\alpha_k^\dagger \alpha_k + E_+(k,q)\beta_k^\dagger \beta_k \right]
\tag{2.19}
$$

with

$$
E_\pm(k,q) = \frac{\epsilon_k + \epsilon_{k\oplus q}}{2} \pm \sqrt{\left(\frac{\epsilon_k - \epsilon_{k\oplus q}}{2}\right)^2 + \Delta^2}.
\tag{2.20}
$$

For $q = \pi$ (antiferromagnetic phase), the lower band $E_-(k,q)$ of the half-filled system is completely filled and there is a gap at the boundaries of the magnetic BZ of size $2\Delta = JS$.

Instead of diagonalizing the $2L \times 2L$-dimensional effective hopping matrix in Eq. (2.4), the task of calculating the ground state energy of a spin configuration with constant angle θ is now reduced to evaluating Eq. (2.20) for $q = \theta$ and summing all $E_\pm(k,\theta)$ with $k \leq k_F$, where k_F denotes the Fermi wave vector.

2.2.2. Dimerized Spin Configurations

The previous section was concerned with spin configurations that can be described with a constant pitch angle θ. The premise here, however, is precisely the possibility to deviate from this antiferromagnetic or spiral configuration by a constant value $\Delta\theta$ that may result in a dimerized spin configuration as shown in Fig. 2.2. Numerical calculations minimizing $E = E(\theta, \Delta\theta)$ in the (J, φ) phase diagram presented in Chapter 3 show that the only potentially inhomogeneous ground state ever present is a

spin-dimerized phase with ($\theta = \pi/2, \Delta\theta = \pi/2$). For simplicity, this section is thus restricted to this special case, even though all results could of course be generalized to arbitrary values of $\Delta\theta$.

The particular dimerized phase considered here can be visualized as a $\uparrow\uparrow\downarrow\downarrow$-pattern of the spins, which doubles the unit cell with respect to the regular antiferromagnet.
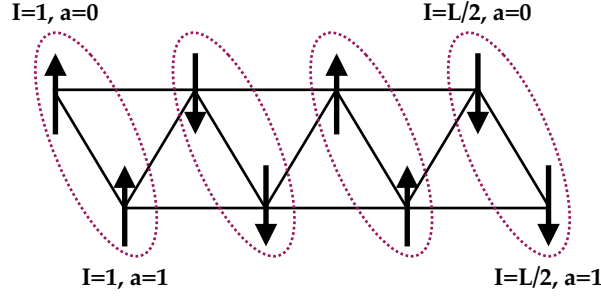
Figure 2.3.: Dimerized spin configuration with $\theta = \pi/2$, $\Delta\theta = \pi/2$. For labelling purposes, two adjacent sites are combined as a 'master-site' as pictured with the dotted outlines and described with inter-site-index $I \in (0, L/2)$ and intra-site-index $a \in (0, 1)$.

Combining adjacent sites with the same orientation into a two-site 'master-site' as pictured in Fig. 2.3 relabels the spin-electron-interaction part of the Hamiltonian as

$$H_J = J \sum_{I=1}^{L/2} \sum_{a=0,1} \mathbf{S}_{Ia}\mathbf{s}_{Ia}, \tag{2.21}$$

where I denotes the inter- 'master-site' index running from 1 to L/2 and a the site[1] index with values 0 or 1, i.e. the upper or lower leg of the zigzag ladder. The dimerized classical spin configuration can - without loss of generality assumed to lie in z-direction - be expressed as

$$\mathbf{S}_{Ia} = S(-1)^I \mathbf{e}_z, \tag{2.22}$$

which yields for the interaction Hamiltonian in Eq. (2.21):

$$
\begin{aligned}
H_J &= \frac{JS}{2} \sum_I \sum_a \sum_{\sigma\sigma'} (-1)^I (\boldsymbol{\sigma}\mathbf{e}_z)_{\sigma\sigma'} c_{Ia\sigma}^\dagger c_{Ia\sigma'} \\
&= \frac{JS}{2} \frac{1}{L/2} \sum_{I,a,\sigma\sigma'} \sum_{K,K'=-\pi/2}^{\pi/2} \sigma_{\sigma\sigma'}^z e^{-iI\pi} e^{-iKI} e^{iK'I} c_{Ka\sigma}^\dagger c_{K'a\sigma'}.
\end{aligned}
\tag{2.23}
$$

In the last line, a Fourier transform similar to Eq. (2.9) was used, except not - as done above in the

---

[1]Not to be confused with the lattice spacing also termed a.

case of homogenous spin configurations - with respect to lattice site $i \in (1, L)$, but with respect to the 'master-site' $I \in (1, L/2)$. Accordingly, the inter-'atomic'-distance is not $a = 1$ anymore as above, but $a = 2$. The first Brillouin zone therefore runs from $-\pi/2$ to $\pi/2$ and contains $L/2$ K-values with $K = n \cdot \frac{2\pi}{L}$ ($n \in \mathbb{N}$). Using again the definition of the Kronecker Delta as above in Eq. (2.14) gives:

$$
\begin{aligned}
H_J &= \frac{JS}{2} \sum_{a,\sigma\sigma'} \sum_{K,K'} \sigma^z_{\sigma\sigma'} \delta_{K',K\oplus\pi} c^\dagger_{Ka\sigma} c_{K'a\sigma'} \\
&= \frac{JS}{2} \sum_{a,\sigma\sigma'} \sum_K \sigma^z_{\sigma\sigma'} c^\dagger_{Ka\sigma} c_{K\oplus\pi,a\sigma'} \\
&= \frac{JS}{2} \sum_a \sum_K \left(c^\dagger_{Ka\uparrow} c_{K\oplus\pi,a\uparrow} - c^\dagger_{Ka\downarrow} c_{K\oplus\pi,a\downarrow} \right) + \text{h.c.} \\
&= \frac{JS}{2} \sum_{a,\sigma} \sum_K z_\sigma \left(c^\dagger_{Ka\sigma} c_{K\oplus\pi,a\sigma} + c^\dagger_{K\oplus\pi,a\sigma} c_{Ka\sigma} \right) ,
\end{aligned}
\tag{2.24}
$$

where $z_\sigma = \pm 1$ for $\sigma = \uparrow, \downarrow$. Similar to above, $K \oplus \pi$ should be understood as $K \oplus \pi = K + \pi + G$ with reciprocal vector G such that $K + \pi$ lies within the first BZ.

The hopping term in the Hamiltonian can also be rewritten using the relabelling as

$$
\begin{aligned}
H_{\text{hopp}} &= \sum_{ij\sigma} t_{ij} c^\dagger_{i\sigma} c_{j\sigma} = \sum_\sigma \sum_{I,I'=1}^{L/2} \sum_{a,b=0,1} t_{II'ab} c^\dagger_{Ia\sigma} c_{I'b\sigma} \\
&= \frac{1}{L/2} \sum_{\sigma II'ab} \sum_{K,K'=-\pi/2}^{\pi/2} t_{II'ab} e^{-iKI} e^{iK'I'} c^\dagger_{Ka\sigma} c_{K'b\sigma},
\end{aligned}
\tag{2.25}
$$

again using the 'master-site'-respective Fourier transform.

The sum over I' can immediately be evaluated explicitly, as the hopping amplitude $t_{II'ab}$ is non-zero only for $I' \in \{I, I+1, I-1\}$. It follows that

$$
\begin{aligned}
H_{\text{hopp}} &= \frac{1}{L/2} \sum_{\sigma Iab} \sum_{K,K'=-\pi/2}^{\pi/2} \Big(t_{IIab} e^{i(K-K')I} (1 - \delta_{ab}) \\
&\quad + t_{I(I+1)ab} e^{i(K-K')I} e^{iK'} + t_{I(I-1)ab} e^{i(K-K')I} e^{-iK'} \Big) c^\dagger_{Ka\sigma} c_{K'b\sigma} \\
&= \frac{1}{L/2} \sum_{\sigma Iab} \sum_{K,K'=-\pi/2}^{\pi/2} e^{i(K-K')I} \big(t_{IIab} (1 - \delta_{ab}) \\
&\quad + t_{I(I+1)ab} e^{iK'} + t_{I(I-1)ab} e^{-iK'} \big) c^\dagger_{Ka\sigma} c_{K'b\sigma},
\end{aligned}
\tag{2.26}
$$

where

$$t_{IIab} = t_2 \quad \text{and}$$

$$t_{I(I+1)ab} = t_{I(I-1)ab} = \begin{cases} t_1, & \text{if } a \neq b, a > b \\ t_2, & \text{if } a = b \end{cases} \tag{2.27}$$

The condition $a > b$ ensures that the hopping is truly along a zigzag geometry, i.e. the rungs only connect each site to *one* other site on the other leg of the lattice outside of their own 'master-site'. The resulting hopping Hamiltonian can be written as a 2x2 matrix

$$\begin{aligned} H_{\text{hopp}} &= \sum_\sigma \sum_K \begin{pmatrix} c_{K0\sigma}^\dagger & c_{K1\sigma}^\dagger \end{pmatrix} \begin{pmatrix} 2t_2\cos(K) & t_1(1+e^{iK}) \\ t_1(1+e^{-iK}) & 2t_2\cos(K) \end{pmatrix} \begin{pmatrix} c_{K0\sigma} \\ c_{K1\sigma} \end{pmatrix} \\ &\equiv \sum_\sigma \sum_K \begin{pmatrix} c_{K0\sigma}^\dagger & c_{K1\sigma}^\dagger \end{pmatrix} \begin{pmatrix} \varepsilon_2(K) & \varepsilon_1(K) \\ \varepsilon_1^*(K) & \varepsilon_2(K) \end{pmatrix} \begin{pmatrix} c_{K0\sigma} \\ c_{K1\sigma} \end{pmatrix}, \end{aligned} \tag{2.28}$$

where $\varepsilon_1(K) \equiv t_1(1 + e^{iK})$ and $\varepsilon_2(K) \equiv 2t_2\cos(K)$. Together with the result for H_J and again using the notation $\Delta \equiv JS/2$, this yields a 4×4-matrix for the entire Hamiltonian

$$H = \sum_\sigma \sum_K \begin{pmatrix} c_{K0\sigma}^\dagger & c_{K1\sigma}^\dagger & c_{K\oplus\pi0\sigma}^\dagger & c_{K\oplus\pi1\sigma}^\dagger \end{pmatrix} \mathbf{M}(K) \begin{pmatrix} c_{K0\sigma} \\ c_{K1\sigma} \\ c_{K\oplus\pi0\sigma} \\ c_{K\oplus\pi1\sigma} \end{pmatrix} \tag{2.29}$$

with

$$\mathbf{M}(K) = \begin{pmatrix} \varepsilon_2(K) & \varepsilon_1(K) & \Delta & 0 \\ \varepsilon_1^*(K) & \varepsilon_2(K) & 0 & \Delta \\ \Delta & 0 & -\varepsilon_2(K) & \varepsilon_1(K+\pi) \\ 0 & \Delta & \varepsilon_1^*(K+\pi) & -\varepsilon_2(K) \end{pmatrix}. \tag{2.30}$$

This can be diagonalized numerically to yield 4 bands (8 if counting $\sigma = \uparrow, \downarrow$, which are, however, pairwise degenerate).

Even though there is no analytical expression for the energy eigenvalues that can be evaluated immediately, still the calculation of the ground state energy has been simplified from diagonalizing a $2L \times 2L$-dimensional matrix to diagonalizing $L/2$ matrices of dimension 4×4. This is a considerable improvement and, as can be seen in, Section 3.3 allows therefore (in combination with CUDA-programming), to calculate lattices of size $\mathcal{O}(10^5)$ easily.

2.3. Perturbative Approaches

In this model, there are several parameter regimes accessible to perturbation theory. In particular, performing perturbation theory in both the weak and strong limit of the coupling constant J, i.e. $J \gg t$ and $J \ll t$, leads to an effective spin-only model of Heisenberg type. In the following section, both will be discussed. Additionally, perturbation theory around $t_1 = 0$ can be found in Appendix B.

2.3.1. Weak Coupling (RKKY) Limit

Phenomenologically, there is a type of indirect exchange interaction observed between nuclear magnetic moments in a metal that is due hyperfine interaction with conduction electrons. The theoretical description of this is attributed to Ruderman and Kittel ([43], 1954), Kasuya ([44], 1956) and Yosida ([45], 1957) and accordingly termed the *RKKY* model. Speaking in the context of the Kondo lattice model, a localized magnetic moment will polarize the conduction electrons in its vicinity, which in turn interact with other localized moments resulting in an effective indirect interaction between them. The nature of this interaction is thus not limited to nearest-neighboring spins and is in fact found to be oscillating as a function of distance. It can be derived using second order perturbation theory as shown in the following.

The starting point is the unperturbed Hamiltonian which is simply the hopping of non-interacting electrons in the conduction band

$$H_0 = \sum_{ij\sigma} t_{ij} c_{i\sigma}^\dagger c_{j\sigma} = \sum_{k\sigma} \epsilon_k c_{k\sigma}^\dagger c_{k\sigma}. \tag{2.31}$$

A small interaction with the localized spins via $J \ll t$ is then introduced via

$$H_1 = J \sum_i \mathbf{s}_i \mathbf{S}_i \,. \tag{2.32}$$

This perturbation is expected to cause an energy shift, which to first order is given by

$$\Delta E^1 = \langle 0|H_1|0\rangle = \frac{J}{2} \sum_{i\sigma\sigma'} (\boldsymbol{\sigma}\mathbf{S}_i)_{\sigma\sigma'} \langle 0|c_{i\sigma}^\dagger c_{j\sigma'}|0\rangle = \frac{J}{2} \sum_{i\sigma\sigma'} (\boldsymbol{\sigma}\mathbf{S}_i)_{\sigma\sigma'} \sum_{kk'} U_{ik}^\dagger U_{ik'} \langle 0|c_{k\sigma}^\dagger c_{k'\sigma'}|0\rangle \tag{2.33}$$

where

$$c_{i\sigma}^\dagger = \sum_k U_{ik} c_{k\sigma}^\dagger \tag{2.34}$$

is also the unitary transformation that diagonalizes the tight binding model H_0 in Eq. (2.31) (i.e. the

discrete Fourier transform) and $|0\rangle$ is the ground state of H_0. In the unpolarized system, the spin is conserved and $\sum_{\sigma\sigma'} \boldsymbol{\sigma}_{\sigma\sigma'} \delta_{\sigma\sigma'} = 0$. It follows that the first order term

$$\Delta E^{(1)} = 0 \tag{2.35}$$

does not contribute. The second order contribution to perturbation theory is in general given by

$$\Delta E^{(2)} = \sum_{n \neq 0} \frac{|\langle 0|H_1|n\rangle|^2}{E_0 - E_n}, \tag{2.36}$$

where $|n\rangle$ are the excited states of the unperturbed system with energies E_n and E_0 is the ground state energy. The only states constributing to the sum in Eq. (2.36) are those excited by single-particle operators corresponding to the particle–hole excitations of the originally filled Fermi sphere

$$|n\rangle = c_{q\sigma}^\dagger c_{q'\sigma'} |0\rangle \equiv |qq'\sigma\sigma'\rangle \tag{2.37}$$

with $q > k_F$ and $q' \leq k_F$ where k_F denotes the Fermi wavevector, i.e. the highest occupied state in the Fermi sea and $\sigma, \sigma' \in (\uparrow, \downarrow)$. The ground state energy of the unperturbed system is given simply by the some of all occupied one-particle energies

$$E_0 = \langle 0|H_0|0\rangle = \sum_{k \leq k_F} \epsilon_k. \tag{2.38}$$

The energies of the excited states $|n\rangle$ are

$$\begin{aligned} E_n = E_{qq'\sigma\sigma'} &= \langle qq'\sigma\sigma'|H_0|qq'\sigma\sigma'\rangle \\ &= \sum_{k \leq k_F, k \neq q'} \epsilon_k + \epsilon_q \end{aligned} \tag{2.39}$$

and thus the energy denominator in Eq. (2.36) is given by

$$E_0 - E_{qq'\sigma\sigma'} = \epsilon_{q'} - \epsilon_q. \tag{2.40}$$

The matrix elements in the numerator of Eq. (2.36) are given by

$$\langle 0|H_0|qq'\sigma\sigma'\rangle = \frac{J}{2} \sum_{i\sigma\sigma'} \sum_{kk'} U_{ik}^\dagger U_{ik'} \left(\boldsymbol{\sigma}\mathbf{S}_i\right)_{\sigma\sigma'} \langle 0|c_{k\sigma}^\dagger c_{k'\sigma'} c_{q\tau}^\dagger c_{q'\tau'}|0\rangle$$

$$= \frac{J}{2} \sum_{i\sigma\sigma'} \sum_{kk'} U_{ik}^\dagger U_{ik'} \left(\boldsymbol{\sigma}\mathbf{S}_i\right)_{\sigma\sigma'} \delta_{kq'}\delta_{\sigma\tau'}\delta_{k'q}\delta_{\sigma'\tau} \qquad (2.41)$$

$$= \frac{J}{2} \sum_{i} U_{iq'}^\dagger U_{iq} \left(\boldsymbol{\sigma}\mathbf{S}_i\right)_{\tau'\tau}.$$

All in all, the entire second order energy shift becomes

$$\Delta E^{(2)} = \sum_{\sigma\sigma',q>k_F,q'\leq k_F} \frac{|\langle 0|H_0|qq'\sigma\sigma'\rangle|^2}{\epsilon_q' - \epsilon_q}$$

$$= \left(\frac{J}{2}\right)^2 \sum_{\sigma\sigma',q>k_F,q'\leq k_F} \left(\sum_i U_{iq'}^\dagger U_{iq} \left(\boldsymbol{\sigma}\mathbf{S}_i\right)_{\sigma'\sigma}\right) \left(\sum_j U_{jq'}^\dagger U_{jq} \left(\boldsymbol{\sigma}\mathbf{S}_j\right)_{\sigma'\sigma}\right)^\dagger \qquad (2.42)$$

$$= \frac{J^2}{2} \sum_{ij} \mathbf{S}_i\mathbf{S}_j \sum_{q>k_F,q'\leq k_F} \frac{U_{iq'}^\dagger U_{iq} U_{jq}^\dagger U_{jq'}}{\epsilon_{q'} - \epsilon_q}$$

where in the last line $\sum_{\sigma\sigma'} \boldsymbol{\sigma}_{\sigma\sigma'}\boldsymbol{\sigma}_{\sigma'\sigma} = 2$ was used.

The perturbation term can thus be written as an effective spin-only Hamiltonian

$$H_{RKKY} = \sum_k J_{RKKY}(k)\mathbf{S}_k\mathbf{S}_{-k} \qquad (2.43)$$

at order J^2 with the effective RKKY coupling $J_{RKKY}(k) = -J^2\chi_0(\omega = 0, k)$ and the static susceptibility of the conduction electrons

$$\chi_0(\omega = 0, k) = \frac{1}{2L} \sum_q \frac{n_{k+q,\uparrow} - n_{q,\downarrow}}{\epsilon(q) - \epsilon(k+q)} \qquad (2.44)$$

where $n_{k\sigma} = \Theta(-\epsilon(k))$ is the occupation number.

2.3.2. Strong Coupling Limit

On the other end of the parameter range of the coupling strength J, perturbation theory can also be used for the limit $J \gg t$. Just as in the RKKY limit, here too, the model can be mapped onto an effective spin-only Hamiltonian of Heisenberg type. Figuratively speaking, the strong coupling limit corresponds to local "bonds" which fix the electron tightly to the respective classical spin and,

within the bond, anti-align their orientations perfectly. At half-filling, there is now one such bond at each lattice site, leaving no possibility for the electrons to move around the lattice. This situation is the starting point for perturbation theory. In order to apply non-degenerate perturbation theory, the classical spin configuration must be considered fixed.

The unperturbed Hamiltonian is then evidently the spin-electron interaction term

$$H_0 = J \sum_i \mathbf{s}_i \cdot \mathbf{S}_i, \tag{2.45}$$

while the perturbation is given by the hopping term

$$H_1 = \sum_{ij\sigma} t_{ij} c_{i\sigma}^\dagger c_{j\sigma}. \tag{2.46}$$

Again following time independent perturbation theory, the first order correction to the ground state energy is given by

$$E_0^{(1)} = \langle 0|H_1|0 \rangle, \tag{2.47}$$

which vanishes, since there is no on-site hopping t_{ii}.

The expression for the second order contribution is, as above,

$$E_0^{(2)} = \sum_{n \neq 0} \frac{|\langle 0|H_1|n \rangle|^2}{E_0 - E_n}. \tag{2.48}$$

where the $|n\rangle$ are eigenstates and $|0\rangle$ the ground state of H_0.

The energy of the ground state is given by the sum of bond-energies, with $|\mathbf{S}_i| = \frac{1}{2}$, as

$$E_0 = \sum_{i=1}^{L} J\langle s_i \rangle \mathbf{S}_i = -\frac{1}{4}JL \,. \tag{2.49}$$

Excited states $|n\rangle$ contributing to the sum in Eq. (2.48) are those that break two of the bonds between spins and electrons to allow one electron to hopp to another site, the excited states have thus an energy lowered by two bond-energies. The difference in the denominator of Eq. (2.48) is then

$$E_0 - E_n = -\frac{1}{4}JL - \left(-\frac{1}{4}J(L-2)\right) = -\frac{J}{2} \,. \tag{2.50}$$

For the numerator, matrix elements of the form

$$\langle 0|c_{i\sigma}^\dagger c_{j\sigma}|n \rangle \tag{2.51}$$

are needed. The ground state $|0\rangle$ can be split into local ground states and expressed as

$$|0\rangle_i = |\theta_i, \phi_i\rangle = \begin{pmatrix} e^{i\phi_i}\cos(\theta_i/2) \\ \sin(\theta_i/2) \end{pmatrix} \tag{2.52}$$

where (ϕ_i, θ_i) are spherical angles of the given classical spin configuration. Without loss of generality, the classical spins can be taken to lie in the $x - y$-plane, i.e. $|0\rangle_i = |\theta_i\rangle$. Note that in particular

$$|\uparrow\rangle = |\theta = 0\rangle = \begin{pmatrix} 1 \\ 0 \end{pmatrix} \quad \text{and} \quad |\downarrow\rangle = |\theta = \pi\rangle = \begin{pmatrix} 0 \\ 1 \end{pmatrix}. \tag{2.53}$$

One excited state $|n\rangle$ describes the hopping of one electron from site $i \to j$:

$$|n\rangle = |0_i\rangle c_{j\sigma}^\dagger c_{j\sigma'}^\dagger |0_j\rangle \tag{2.54}$$

The sum $\sum_n$ in Eq. (2.48) is thus to be understood as over every ordered pair (i, j). One matrix element for (i, j) including the sum over spin $\sigma = \uparrow, \downarrow$ is

$$\begin{aligned} \sum_\sigma \langle 0| c_{i\sigma}^\dagger c_{j\sigma} |n\rangle &= \sum_\sigma \langle\theta_i|\langle\theta_j| c_{i\sigma}^\dagger c_{j\sigma} |0\rangle_i c_{j\sigma}^\dagger c_{j\sigma'}^\dagger |0\rangle_j \\ &= \langle\theta_i|\uparrow\rangle_i \langle\theta_j|\downarrow\rangle_j - \langle\theta_i|\downarrow\rangle_i \langle\theta_j|\uparrow\rangle_j \\ &= \cos(\frac{\theta_i}{2})\sin(\frac{\theta_j}{2}) - \sin(\frac{\theta_i}{2})\cos(\frac{\theta_j}{2}). \end{aligned} \tag{2.55}$$

With $\sin x \cos y = \frac{1}{2}(\sin(x-y) + \sin(x+y))$ and $\sin(\frac{\theta_i - \theta_j}{2}) = -\sin(\frac{\theta_j - \theta_i}{2})$ follows

$$\begin{aligned} \sum_\sigma \langle 0| c_{i\sigma}^\dagger c_{j\sigma} |n\rangle &= \frac{1}{2}\left(\sin(\frac{\theta_j - \theta_i}{2}) + \sin(\frac{\theta_j + \theta_i}{2}) \right. \\ &\quad \left. - \sin(\frac{\theta_i - \theta_j}{2}) - \sin(\frac{\theta_i + \theta_j}{2})\right) \\ &= \sin(\frac{\theta_j - \theta_i}{2}) := \sin(\frac{\theta_{ij}}{2}), \end{aligned} \tag{2.56}$$

where θ_{ij} denotes the angle between spins at sites i and j. On the zigzag ladder, the angle between nearest neighbors is $\theta_{ij} = \theta \pm \Delta\theta$, while the angle between next-to-nearest neighbors is 2θ. The hopping amplitudes are $t_{ij} = t_1$ for nearest and $t_{ij} = t_2$ for next-to-nearest neighbors. Thus, the

energy shift due to one hopping process $i \to j$ is given by

$$\Delta E_{ij} = \frac{|\langle 0|H_1|ij\rangle|^2}{E_0 - E_{ij}} = -\frac{2}{J} t_{ij}^2 \sin^2(\frac{\theta_{ij}}{2})$$

$$= \begin{cases} -\frac{2}{J} t_1^2 \sin^2(\frac{\theta \pm \Delta\theta}{2}) & \text{for } i, j \text{ nearest neighbors} \\ -\frac{2}{J} t_2^2 \sin^2(\frac{2\theta}{2}) & \text{for } i, j \text{ next-to-nearest neighbors .} \end{cases} \tag{2.57}$$

All in all, including both $i \to j$ and $j \to i$, the ground state energy including second-order corrections is therefore

$$E = -\frac{1}{4}LJ - (\#\,\text{n.n.n.}) \cdot \frac{4}{J} t'^2 \sin^2\left(\frac{2\theta}{2}\right)$$

$$- (\#\,\text{n.n.}) \cdot \frac{4}{J} t^2 \left(\frac{1}{2}\sin^2\left(\frac{\theta + \Delta\theta}{2}\right) + \frac{1}{2}\sin^2\left(\frac{\theta - \Delta\theta}{2}\right)\right) + \mathcal{O}\left(\frac{t^3}{J^3}\right) \tag{2.58}$$

where $\#\,\text{n.n.}$ is the number of nearest and $\#\,\text{n.n.n.}$ the number of next-to-nearest neighbors. With $\sin^2(\frac{x}{2}) = \frac{1}{2}(1 - \cos(x))$ follows finally up to $\mathcal{O}\left(\frac{t^3}{J^3}\right)$:

$$E = L\left(-\frac{1}{4}J - \frac{2t_1^2}{J} - \frac{2t_2^2}{J} + \frac{t_1^2}{J}\cos(\theta)\cos(\Delta\theta) + \frac{2t_2^2}{J}\cos(2\theta)\right). \tag{2.59}$$

As shown in Appendix A, the energy for the Heisenberg $J_1 - J_2$ model on a zigzag ladder is

$$E(\theta, \Delta\theta) = L\,S^2\left(J_1 \cos\theta \cos\Delta\theta + J_2 \cos 2\theta\right). \tag{2.60}$$

Comparing to Eq. (2.59), the second-order perturbation theory for the Kondo lattice model can apparently be mapped onto an effective Heisenberg $J_1 - J_2$ model with

$$J_1 = \frac{8t_1^2}{J} \quad \text{and} \quad J_2 = \frac{8t_2^2}{J} \tag{2.61}$$

as well as a constant energy-offset of

$$\Delta E = L\left(-\frac{1}{4}J - \frac{2t_1^2}{J} - \frac{2t_2^2}{J}\right). \tag{2.62}$$

The equilibrium spin configuration for the Heisenberg $J_1 - J_2$-model is, as shown in Appendix A,

$$\begin{aligned} \theta = \pi, \ \Delta\theta = 0 & \qquad \text{if } J_1 > 4J_2 \\ \theta = \arccos\left(-\frac{J_1}{4J_2}\right), \ \Delta\theta = 0 & \quad \text{if } J_1 < 4J_2 \,, \end{aligned} \tag{2.63}$$

which can now be translated into Kondo lattice parameters as

$$
\begin{aligned}
\theta &= \pi, \ \Delta\theta = 0 && \text{if } t_1 > 2t_2 \\
\theta &= \arccos\left(-\frac{t_1^2}{4t_2^2}\right), \ \Delta\theta = 0 && \text{if } t_1 < 2t_2 \,.
\end{aligned}
\tag{2.64}
$$

3. Equilibrium Phase Diagram

The ground state phase diagram of the unfrustrated one dimensional Kondo lattice model with classical spins was studied for example by employing a Monte Carlo method in [10] and using a self-consistent mean-field-like approach in [46]. The phase diagram, as a function of coupling constant J and electron filling $\langle n \rangle$, resulting from the latter is shown in Fig. 3.1. The lattice with low electron filling $\langle n \rangle \ll 1$ is found to have a ferromagnetic ground state, while the half-filled system with $\langle n \rangle = 1$ is antiferromagnetic for any value of J. In between is a region of phase separation characteristic of a first order phase transition, where both phases coexist. Additionally, for small to medium coupling constant J and medium filling $\langle n \rangle$, there is an incommensurate spiral phase.
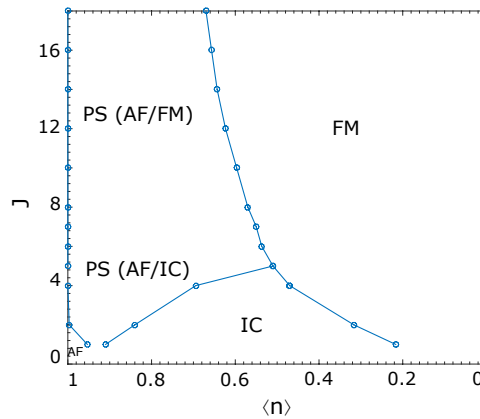
Figure 3.1.: Ground state phase diagram of the unfrustrated Kondo chain with classical spins as a function of coupling constant J and electron filling $\langle n \rangle$ with FM = ferromagnetic, AF = antiferromagnetic, IC = incommensurate (spiral), PS = phase separation. On the line $\langle n \rangle = 1$, the system is antiferromagnetic. From [46].

At half-filling, the system is therefore either antiferromagnetic at zero temperature, or disordered at finite temperature. On the zigzag ladder which was introduced in the previous chapter, however, the situation is different. The inclusion of frustration in the form of next-to-nearest neighbor hopping opens a new dimension of the phase diagram and results in a new phase, which is exclusive to the frustrated case.

This chapter shows numerical results for the ground state of the Kondo lattice with classical spins on the zigzag ladder. Here, the system will always be assumed at half-filling with $\langle n \rangle = 1$. The first part in Section 3.1 will introduce the method, review the parameterization and present the ground state phase diagram as a function of coupling constant J and frustration φ. The next part in Section 3.2 will carry on the discussion on perturbative approaches, which was started in Section 2.3 analytically, and present numerical results. After a discussion of finite size effects in Section 3.3, the semiclassical phase diagram presented here will in Section 3.4 eventually be compared to the quantum mechanical analogue obtained with DMRG by M. Peschke [20]. Large parts of this chapter have been taken from our joint publication [21].

3.1. The Ground State as a Function of J and φ

The Kondo lattice model as introduced in Chapter 2 has essentially two parameters - the Kondo coupling constant J that couples conduction electrons to local moment spins and the hopping amplitude ratio, i.e. measure of frustration, $\varphi = \arctan(t_2/t_1)$. The equilibrium phase diagram in this chapter is calculated as a function of these two parameters in essentially the entire parameter range $0 \leq \varphi \leq \pi/2$ and $0 \leq J < \infty$. For each set of (J, φ), the ground state of the Kondo lattice system with classical spins is found by a simple variational calculation. As seen in Section 2.1, the ground state energy of the system is a functional of the spin configuration $\{\mathbf{S}\} = (\mathbf{S}_1, ..., \mathbf{S}_L)$:

$$E(\{\mathbf{S}\}) = \sum_{ii'\sigma\sigma'} \left(t_{ii'}\delta_{\sigma\sigma'} + \frac{J}{2}(\boldsymbol{\sigma}\mathbf{S}_i)_{\sigma\sigma'}\delta_{ii'} \right) \langle c_{i\sigma}^\dagger c_{i'\sigma'} \rangle_{\{\mathbf{S}\}} . \tag{3.1}$$

Instead of considering all possible spin configurations in space, the parametrization as introduced in Section 2.2 and shown in Fig. 2.2 is used, where two angles θ and $\Delta\theta$ are sufficient to describe the orientation of the classical spins. With this, the dependency on the spin configuration in Eq. (3.1) therefore reduces to $E = E(\theta, \Delta\theta)$. The angle θ is varied between $0 \leq \theta \leq \pi$ on a finite grid with discrete values $\theta = n2\pi/L$ ($n \in \mathbb{Z}$) to ensure consistency with periodic boundary conditions. For convenience, the same grid is used for $\Delta\theta$, despite the fact that it actually is a continuous variable. For symmetry reasons, it is sufficient to consider $0 \leq \Delta\theta \leq \pi/2$. Also note that $(\theta \rightarrow \theta - \pi, \Delta\theta \rightarrow \Delta\theta - \pi)$ is a symmetry of the system.

The relevant φ- and J-ranges - in practice $J \leq 14$ turns out as sufficient - can now be scanned to find the minimum energy and corresponding optimal spin configuration $(\theta, \Delta\theta)$ for each parameter pair J, φ. Exemplary results are shown in Fig. 3.2 for two calculations with constant J (left two columns, in pink) and two calculations with constant φ (right two columns, in blue). The leftmost column shows, from top to bottom, the minimum energy per lattice site E/L and the corresponding optimal angles $\theta, \Delta\theta$ as a function of φ for $J = 3$ in a system with $L = 100$. At $\varphi = 0$, the system is simply the well known one dimensional unfrustrated chain with an antiferromagnetic ground state ($\theta = \pi, \Delta\theta = 0$)

as shown in Fig. 3.1. When increasing the frustration, there emerges a critical φ_c at which the ground state changes to a new *dimerized* state with $(\theta = \pi/2, \Delta\theta = \pi/2)$. The same calculations performed at $J = 10$ in the second column show in between the antiferromagnetic and dimerized phase, the existence of another ground state configuration, a spiral phase with continuously varying θ.
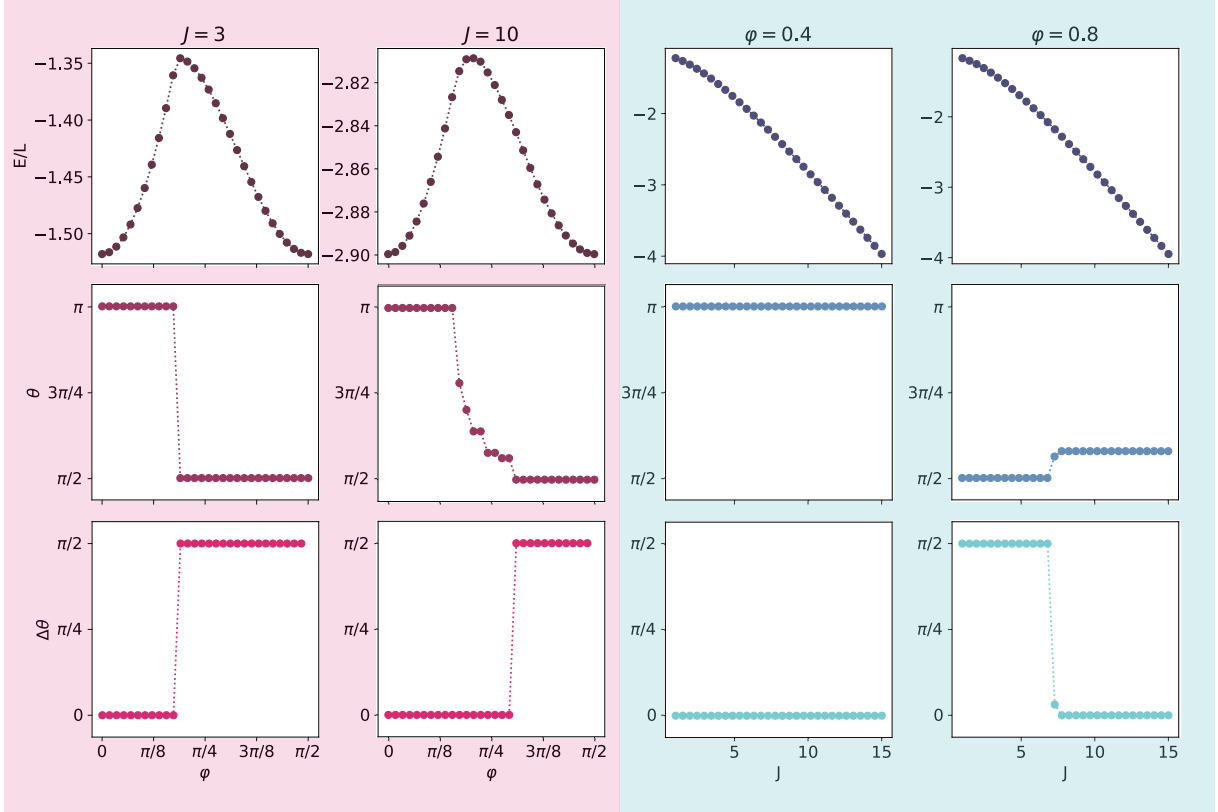
Figure 3.2.: Minimum energy per lattice site and optimal θ and $\Delta\theta$ as a function of φ for $J = 3, 10$ (first and second column, pink region) and as a function of J for $\varphi = 0.4, 0.8$ (third and fourth column, blue region) for $L = 100$.

Keeping $\varphi = 0.4$ constant and varying J as shown in the third column in Fig. 3.2, leads to a rather uneventful picture. The entire J-range here leads to an antiferromagnetic ground state. The same J-variation at $\varphi = 0.8$ as shown in the rightmost column, however, reveals a phase boundary between a dimerized state with $(\theta = \pi/2, \Delta\theta = \pi/2)$ and a spiral with $\theta \approx 104°$ at around $J_c \approx 6$. The latter is incidentally also the ground state of the classical $J_1 - J_2$-Heisenberg model with $J_1 = J_2$, which will be discussed in more detail later on. Note that the shape of $\theta(\varphi)$ in the middle row of the first two columns is consistent with a first order antiferromagnetic-dimerized transition and a continuous antiferromagnetic-spiral transition.

After similar calculations across the entire parameter space, the resulting equilibrium phase diagram

is shown in Fig. 3.3. The solid line indicates calculations for lattice sizes of about $L = 200$, for which finite size analysis shows convergence in the regime $0 < \varphi \lesssim \pi/4$. Beyond this, however, much larger lattice sizes of up to $L = \mathcal{O}(10^5)$ are needed and the results plotted as data points in Fig. 3.3. The dimerized phase for $\varphi \gtrsim \pi/4$ shown in the second column of Fig. 3.2 for $J = 10$ for example, is actually a finite size effect, and should in the thermodynamic limit $L \to \infty$ actually be a spiral phase with θ close to, but not exactly $\pi/2$ and $\Delta\theta = 0$. A detailed discussion of finite size effects can be found in Section 3.3. Both the regimes $J \ll t$ and $J \gg t$ are accessible with perturbation theory as shown analytically in Section 2.3, a comparison with numerical results is shown in Section 3.2.
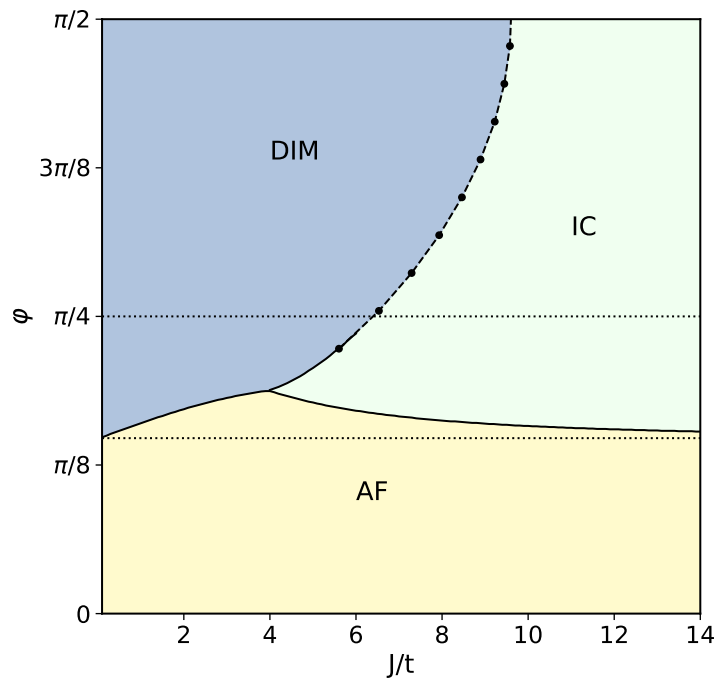
Figure 3.3.: $\varphi - J$ magnetic phase diagram with an antiferromagnetic phase (AF, $\theta = \pi$, $\Delta\theta = 0$), an incommensurate spiral phase (IC, $\pi/2 < \theta < \pi$, $\Delta\theta = 0$), and a dimerized phase (DIM, $\theta = \pi/2$, $\Delta\theta = \pi/2$). One of the horizontal dotted lines indicates $t_1 = t_2$ ($\varphi = \pi/4$), the other $t_1 = 2t_2$ ($\varphi \approx 0.148\pi$). Calculations have been performed for $L = 200$. This is sufficient for convergence, except for the regime $\varphi \gtrsim \pi/4$ where much larger systems with up to $L = 100,000$ sites are necessary. The dashed line interpolates between the data points.

As shown for selected parameter ranges in Fig. 3.2, the numerical calculations show the presence of three different phases. As expected, the well-known result for the unfrustrated chain with $\varphi = 0$ is reproduced, i.e. an antiferromagnetic phase with ($\theta = \pi$, $\Delta\theta = 0$). Note that as opposed to the 1D quantum system, the ground state of the classical system does exhibit true long range order at temperature $T = 0$. The classical spins act like a staggered magnetic field, resulting in a magnetic

unit cell twice the size of the original lattice unit cell. As shown in Section 2.2.1, the electronic band structure consists of two dispersive bands in the reduced Brillouin zone $-\pi/2 < k \leq \pi/2$ with a gap of $JS = J/2$ at the zone boundary. At half-filling, the system is evidently an insulator.

This characteristic is preserved after turning on the next-to-nearest neighbor hopping t_2 by increasing φ. In fact, all of the phases present in the phase diagram Fig. 3.3 show a finite gap between the highest occupied and the lowest unoccupied one-particle energies given by the eigenvalues of the effective hopping matrix (Eq. (2.4)). As the gap is of the order of J, this is of course numerically not possible to decide for weak J. The finite-size gap is t/L, so that for $J \to 0$ at fixed L the only statement that can be made with certainty is for $J \gtrsim t/L$.

Even away from the unfrustrated limit at $\varphi = 0$, the antiferromagnetic phase persists after increasing $\varphi > 0$ and extends up to a critical value φ_c that depends, albeit not very strongly, on the exchange coupling J. In the weak coupling limit, the phase boundary is found to be at $\varphi_c(J \to 0) \equiv \varphi_0 = \arctan(1/2) \approx 0.148\pi$, which is drawn as a dotted line in Fig. 3.3 and corresponds to $t_1 = 2t_2$. This is the exact position of the Lifschitz point where the number of Fermi points in the noninteracting band structure changes from two (for $\varphi < \varphi_0$) to four (for $\varphi > \varphi_0$) as seen in Fig. 3.4. Coincidentally, this is also the value of the transition in the strong coupling regime $J \to \infty$ where the phase boundary is also found at $\varphi_c(J \to \infty) \equiv \varphi_\infty \approx 0.148\pi$, which is not pictured in Fig. 3.3 as $J = 14$ is not quite converged to qualitative behavior of $J \to \infty$. This transition was also found using perturbation theory in Section 2.3.2, where in Eq. (2.64) the transition from an antiferromagnetic to spiral phase was found to lie precisely at $\varphi_\infty = \arctan(1/2)$.
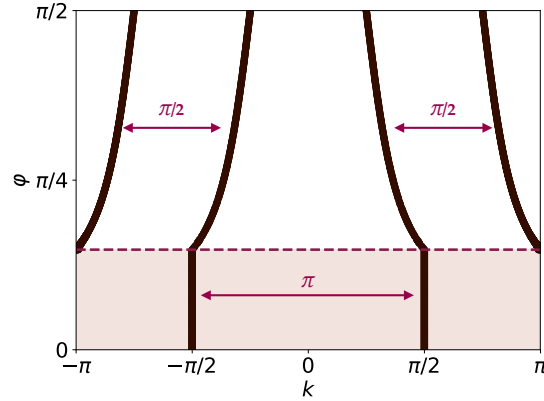
Figure 3.4.: Location of the Fermi points in k-space as a function of φ. The dashed red line illustrates the Lifshitz transition between a state with two and with four Fermi points at $\varphi = \varphi_0 = \arctan(\frac{1}{2}) \approx 0.148\pi$ ($t_1 = 2t_2$). Horizontal arrows: nesting vectors.

For weak $J \lesssim 4$, the phase transition at φ_c is a first order transition between the well-known antiferro-

magnetic phase and a new *spin-dimerized* phase with $(\theta = \pi/2, \Delta\theta = \pi/2)$. In this dimerized phase, the spin configuration exhibits a ↑↑↓↓-like pattern with antiferromagnetic correlations between next nearest neighbors, i.e. on the sides of the ladder, and alternating ferro- and antiferromagnetic correlations on the rungs of the ladder.

For larger J, however, the phase boundary φ_c separates the antiferromagnetic phase not from the dimerized, but from an incommensurate spin spiral phase (IC) with continuously varying pitch angle between $\pi/2 < \theta < \pi$, as can be seen in the middle row of the second column in Fig. 3.2, where $\theta(\varphi)$ is plotted for $J = 10$. Increasing φ starting at φ_c, the spin configuration changes from $\theta = \pi$, i.e. antiferromagnetic order along the rungs - or nearest neighbors, to an incommensurate spiral phase that ultimately ends in a 90° spiral for $\varphi \to \pi/2$. A first order phase transition separates the spiral phase from the dimerized phase along the J-axis that starts at $J_c \approx 9.7$ at $\varphi = \pi/2$ and terminates in a triple point at $J_{\text{tri}} \approx 4.2$.

Dimerization is a nonperturbative phenomenon. For $J \to 0$, standard RKKY theory does not recover spin dimerization, at least not at order J^2, see Section 3.2.2. Still, the phase boundary ends at $J = 0$ for a finite hopping ratio: $\varphi_c^{(\text{dim})}(J) \to \varphi_0 = \arctan(\frac{1}{2})$ for $J \to 0$. It is obvious that in the $J \to 0$ limit the spin dimerization is caused by the Lifschitz transition at φ_0, where the number of Fermi points in the noninteracting band structure changes. It is noteworthy that φ_0 coincides with $\varphi_\infty = \varphi_c^{(\text{dim})}(J = \infty)$. However, this must be seen as a coincidental match; for example, the wave vectors of the incommensurate phase for strong J do not correspond to nesting vectors connecting noninteracting Fermi points.

3.2. Perturbative Approaches

3.2.1. Strong Coupling Regime

In the ground state of the atomic limit $t_1 = t_2 = 0$, each lattice site i is occupied by exactly one electron. The local spin moment $\langle \mathbf{s}_i \rangle$ is fully polarized and oriented antiparallel to the classical spin $\mathbf{S}_i$. To compute the functional $E(\{\mathbf{S}\})$ (Eq. (3.1)) the configuration of classical spins $\{\mathbf{S}\} = (\mathbf{S}_1, ..., \mathbf{S}_L)$ must be considered as fixed, and thus the electronic ground state $|0\rangle$ is nondegenerate. The first nonzero contribution to the functional within nondegenerate perturbation theory in powers of t/J is found at second order:

$$E(\{\mathbf{S}\}) = -L\frac{J}{4} + \sum_{n \neq 0} \frac{|\langle 0|H_1|n\rangle|^2}{E_0 - E_n} + \mathcal{O}(t^3/J^2). \tag{3.2}$$

Here, the perturbation $H_1 = \sum_{ij\sigma} t_{ij} c_{i\sigma}^\dagger c_{j\sigma}$ is the hopping term in Eq. (3.2), $|0\rangle$ and $|n\rangle$ are the ground and the excited states of the Kondo term H_0, and $E_0 = -LJ/4$ and E_n are the corresponding unper-

turbed eigenenergies. The straightforward calculation is given in Section 2.3.2 and results in:

$$
\begin{aligned}
E(\theta, \Delta\theta) =&\text{const.} + \frac{L}{4}\left(J_1 \cos\theta \cos\Delta\theta + J_2 \cos(2\theta)\right) \\
&+ \mathcal{O}(t^4/J^3),
\end{aligned}
$$

which is just the energy of the classical-spin ($|\mathbf{S}_i| = 1/2$) Heisenberg model on the zigzag ladder with exchange couplings $J_1 = 8t_1^2/J$ and $J_2 = 8t_2^2/J$ and for the same parameterization of the spin configuration as assumed above for the classical-spin Kondo lattice (see Fig. 2.2). The constant, $\{\mathbf{S}\}$-independent energy offset is given by

$$
\Delta E = L\left(-\frac{1}{4}J - \frac{2t_1^2}{J} - \frac{2t_2^2}{J}\right). \tag{3.3}
$$

As the ground-state energy correction at order t^3/J^2 vanishes identically for all $(\theta, \Delta\theta)$ due to a cancellation of two different types of virtual ring-exchange processes, Eq. (3.3) holds up to fourth-order corrections. The according calculation is a bit more tedious but still straightforward and is not reported here.

As shown in Appendix A, minimization of the energy functional yields $\Delta\theta = 0$ for all (φ, J). Evidently, there is no spin dimerization in this theory. The optimal pitch angle θ for the spin configuration depends solely on φ and is $\theta = \pi$ for $t_1 > 2t_2$ and

$$
\theta = \arccos\left(-\frac{t_1^2}{4t_2^2}\right) = \arccos\left(-\frac{1}{4\tan^2(\varphi)}\right) \tag{3.4}
$$

for $t_1 < 2t_2$, which is in accordance with the numerical results of the full theory in the $J \to \infty$ limit.

Strong-coupling perturbation theory also explains why convergence of the results with increasing L is extremely poor in the range $\pi/4 \lesssim \varphi < \pi/2$ and for strong J. As detailed in Section 3.3, comparatively large systems must be considered to control the finite-size effects. Calculations in this parameter regime are performed for systems with up to $L = 100,000$ sites, see dots in Fig. 3.3.

In general, the total energy can be expanded in powers of $1/J$ as follows:

$$
E(J, \varphi) = E_0 + \frac{1}{J}E_2 + \frac{1}{J^3}E_4 + \mathcal{O}(\frac{1}{J^5}). \tag{3.5}
$$

Seeing as the strong coupling result Eq. (3.3) holds up to fourth order corrections, the difference between full theory and perturbation theory is expected to be $\propto t^4/J^3$, which, as can be seen in Fig. 3.5, is indeed the case.
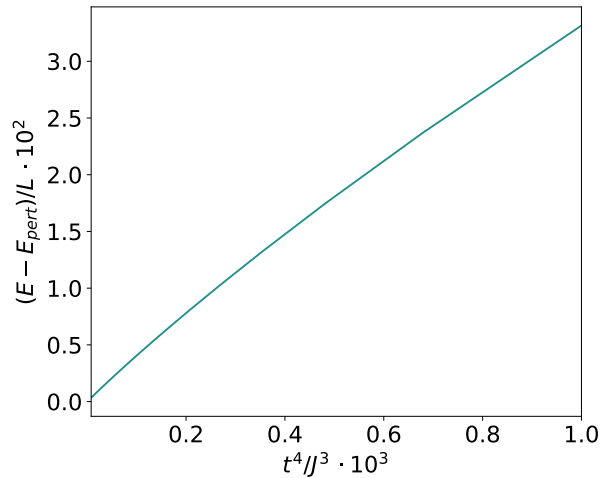
Figure 3.5.: Difference energy of full theory E and strong coupling perturbation theory E_{pert} per lattice site plotted against $1/J^3$ for $\varphi = \pi/4$ and $L = 50$.

Also apparent in Fig. 3.5 is the fact that perturbation theory agrees moderately well with the full theory even for J-values as low as $J = 10$, which is the smallest value plotted in Fig. 3.5, as even then the energy difference per lattice site is of $\mathcal{O}(10^{-2})$. At the highest plotted value of $J = 50$ perturbation theory is in nearly perfect agreement with the ground state energy of the full theory. Note that the energy plotted in Fig. 3.5 is the *ground state energy*, i.e. $E(\theta, \Delta\theta)$ minimized with respect to θ and $\Delta\theta$.

The qualitative agreement of the full energy landscape as a function of all θ and $\Delta\theta$ is shown in Fig. 3.6. The 2D parameter space is illustrated by plotting the energy per lattice site E/L as a function of θ for all values of $\Delta\theta$ according to the pictured color scale, where in particular the deepest red line corresponds to $\Delta\theta = 0$, the lightest yellow line to $\Delta\theta = \pi/2$ and the deepest blue line to $\Delta\theta = \pi$. Note that the above-mentioned symmetry ($\theta \to \theta - \pi$, $\Delta\theta \to \Delta\theta - \pi$) of the system is immediately apparent, as the minimum of the red line with $\Delta\theta = 0$ is mirrored around $\theta = \pi/2$ onto the minimum of the blue line where $\Delta\theta = \pi$. The left column shows the energy landscape of the full theory next to the perturbation theory result in the right column. The rows show different values of J. At $J = 5$ in the top row, i.e. Fig. 3.6 a., the energy minimum seems to be nearly at the same location $(\theta, \Delta\theta)$ for both full and perturbation theory, but the value of the ground state energy differs noticeably. Additionally, the entire shape of the $(\theta, \Delta\theta)$-dependence is different and the energy spectrum much narrower in the full Kondo model compared to the perturbation theory result. In the middle row, however, where $J = 10$, the overall qualitative agreement is already apparent and both location $(\theta, \Delta\theta)$ and value of minimum energy of the perturbation theory is close to the full theory. Finally, in the bottom row, where $J = 50$, the agreement is nearly perfect. The agreement between the full and perturbation theory is thus not limited to value and location of the energy minimum $E(\theta, \Delta\theta)$ but is identical for the entire dependence of the energy on θ and $\Delta\theta$, as it should be, knowing that for $J \to \infty$ the Kondo lattice

model with classical spins can be mapped exactly onto the Heisenberg $J_1 - J_2$-model. To see this, the calculation in Appendix A can be done for arbitrary spin configurations.

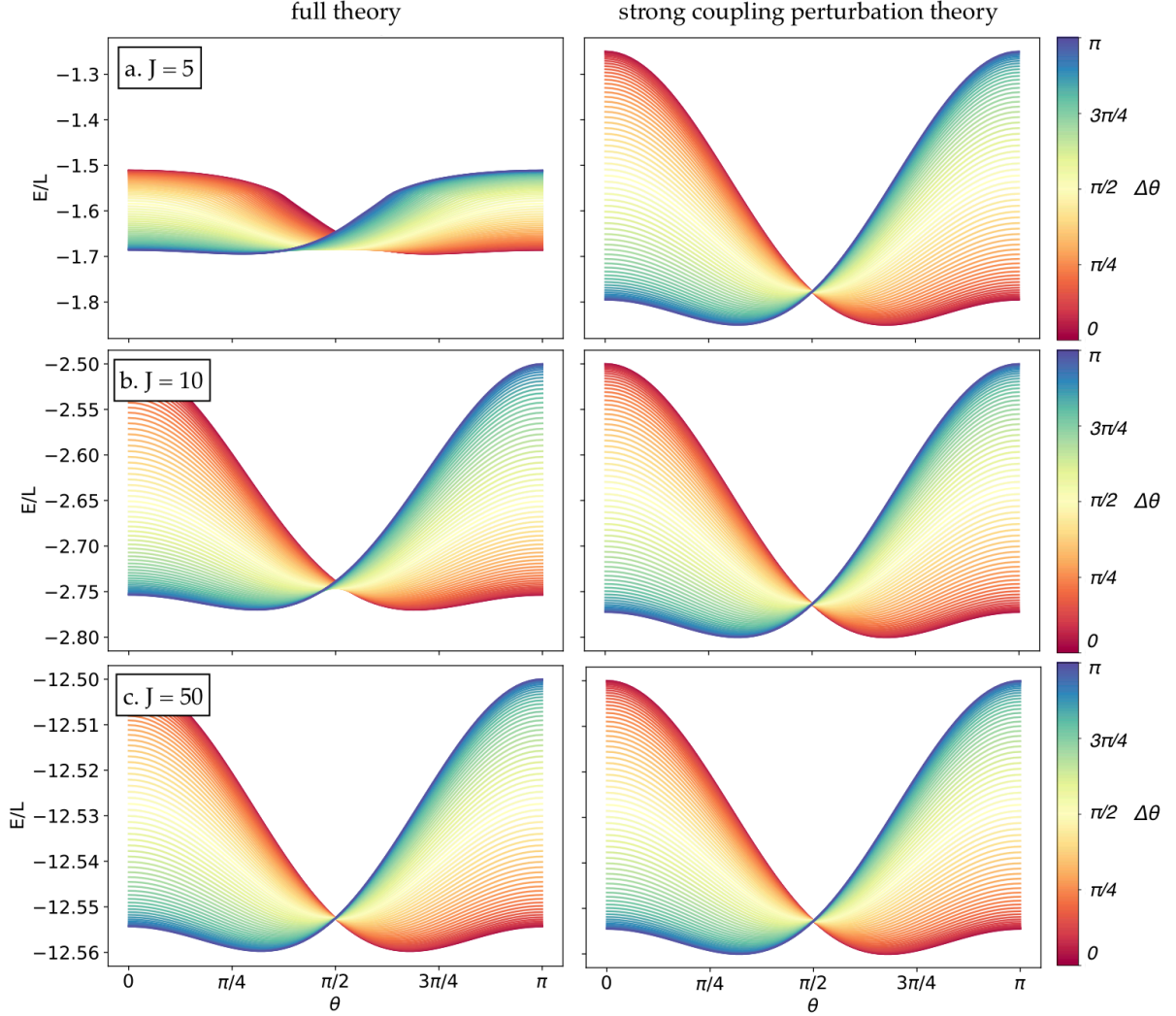**Figure 3.6.**: Energy per lattice site E/L as a function of θ (x-axis) and $\Delta\theta$ (colored lines) for a system with $L = 128$ at $\varphi = 0.6$ and a. $J = 5$ (top row), b. $J = 10$ (middle row) and c. $J = 50$ (bottom row) in the full Kondo lattice theory with classical spins (left column) and for the effective spin-only theory obtained by strong coupling perturbation theory (right column).

3.2.2. Weak Coupling Regime - RKKY

The effective spin Hamiltonian obtained by standard RKKY theory [43–45] is given by

$$H_{\text{RKKY}} = \sum_k J_{\text{RKKY}}(k)\mathbf{S}_k\mathbf{S}_{-k} \tag{3.6}$$

at order J^2 in the limit $J \to 0$. For a detailed calculation in real space, see Section 2.3.1. The effective RKKY coupling $J_{\text{RKKY}}(k) = -J^2\chi_0(\omega = 0, k)$ is given by the static magnetic susceptibility of the noninteracting conduction electrons

$$\chi_0(\omega = 0, k) = \frac{1}{2L}\sum_q \frac{n_{k+q,\uparrow} - n_{q,\downarrow}}{\varepsilon(q) - \varepsilon(k+q)} \, , \tag{3.7}$$

where $n_{k\sigma} = \Theta(-\varepsilon(k))$ is the occupation number and $\varepsilon(k)$ the dispersion of the zigzag lattice, i.e.

$$\varepsilon(k) = -2t_1\cos(k) - 2t_2\cos(2k) \, . \tag{3.8}$$

If $t_2 < t_1/2$ ($\varphi < \varphi_0 = \arctan(\frac{1}{2}) \approx 0.148\pi$), there are two Fermi points at $k_{\text{F}} = \pm\pi/2$, independent of φ. The susceptibility diverges logarithmically with $L \to \infty$ at $k = \pi$, as is easily seen by expanding the denominator in q around $q = k_{\text{F}}$. Hence, spin correlations are predominantly antiferromagnetic, consistent with the antiferromagnetic phase found numerically. If $t_2 > t_1/2$, there are four Fermi points, see Fig. 3.4, resulting in a logarithmic divergence of the susceptibility $\chi_0(0, k)$ at the φ-independent nesting „vector" $k = \pi/2$. This is consistent with a $\pi/2$ spin spiral as well as with a spin-dimerized phase. Consequently, weak-coupling perturbation theory appears to explain the presence of the phase transition at $t_1 = 2t_2$ in the $J \to 0$ limit. One has to be aware, however, that the effective RKKY model (Eq. (3.6)) is actually ill-defined in one dimension [47] due to the divergence of the coupling constant.

Considered here are arbitrary but *finite L*. In this regime, weak-coupling perturbation theory is well behaved, and the RKKY coupling constants can be computed numerically using Eq. (3.6) or in the real-space representation as given in Section 2.3.1. Because of the wave-like nature of the perturbation, the value of the exchange coupling constant J_{RKKY} oscillates as a function of the spin-spin distance, which is reproduced numerically and shown in Fig. 3.7 for a system with $L = 130$ sites at $\varphi = 0.3$ and $J = 0.01$.

For numerical calculations of RKKY theory as obtained by nondegenerate second order perturbation theory as detailed in Section 2.3.1, depending on the value of φ, the system size L must be chosen with care. This is a result of the Lifshitz transition mentioned above. In order to obtain a nondegenerate electronic ground state, at half-filling the system size needs to be chosen as $L = 4n + 2$ with integer n if $t_2 < t_1/2$ ($\varphi < \varphi_0$), and $L = 4n$ for $t_2 > t_1/2$ ($\varphi > \varphi_0$). In the latter case, occupied two-fold spin-degenerate one-particle states labeled by wave vectors k come in pairs $\pm k$, except for $k = 0$ and $k = \pi$.

The ground-state classical-spin configuration is obtained by minimization of the energy function

$$E_{\text{RKKY}}(\theta, \Delta\theta) = E_0 + \sum_{ij} J_{\text{RKKY},ij} \mathbf{S}_i \mathbf{S}_j . \tag{3.9}$$

Here, the constant offset E_0 is given by the total ground state energy of the half-filled conduction band at $J = 0$, i.e., $E_0 = \sum_{ij\sigma} t_{ij} \langle c_{i\sigma}^\dagger c_{j\sigma} \rangle$. Eq. (3.9) is easily evaluated numerically, and a nontrivial θ and $\Delta\theta$ dependence of $E_{\text{RKKY}}(\theta, \Delta\theta)$ is found as shown in Fig. 3.8.
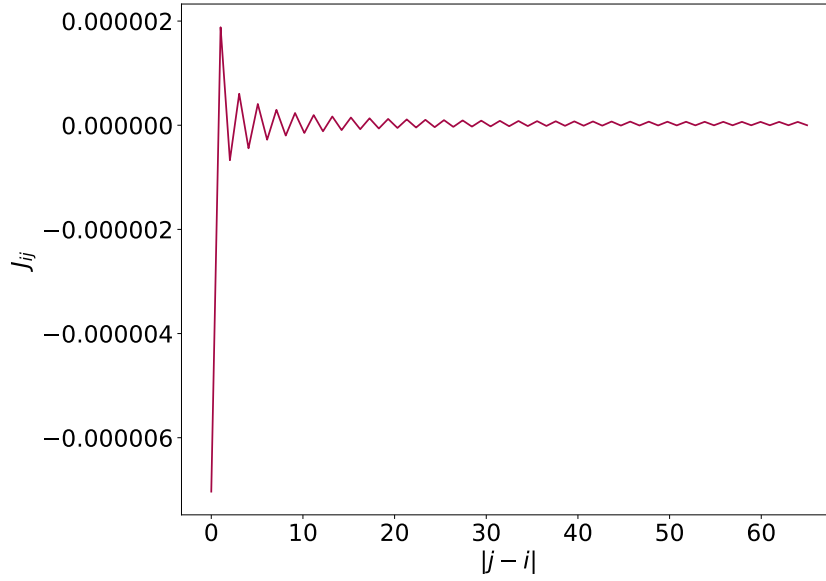
Figure 3.7.: RKKY coupling J_{ij} as a function of the distance $|j - i|$ here given for fixed $i = 0$ and $L = 130$ at $\varphi = 0.3$ and $J = 0.01$. Due to periodic boundary conditions the plot only covers $j = 0$ to $j = L/2$.

Fig. 3.8 shows a comparison between RKKY-perturbation theory and full theory for the entire $\theta, \Delta\theta$-dependent energy landscape similar to Fig. 3.6, where this was done for strong coupling perturbation theory. Again, the energy per lattice site E/L is plotted as a function of θ with different values of $\Delta\theta$ denoted as differently colored lines according to the colorbar on the right. In particular, $\Delta\theta = 0$ is shown as the dark red line, $\Delta\theta = \pi/2$ as light yellow, and $\Delta\theta = \pi$ as dark blue. Just as in Fig. 3.6, the symmetry $(\theta \to \theta - \pi, \Delta\theta \to \Delta\theta - \pi)$ of the system is conveyed as the minimum of the red line with $\Delta\theta = 0$ is mirrored around $\theta = \pi/2$ onto the minimum of the blue line where $\Delta\theta = \pi$. The left column shows the results of the full theory, compared to the right, where numerical results for the RKKY theory were obtained using Eq. (3.9). The rows correspond to different values of the coupling constant J.

Starting at the bottom row Fig. 3.8 c. where $J = 1.0$, the difference between the full theory on the left

and RKKY theory on the right is very noticeable. The only similarity that could be deduced is that the minimum of $E(\theta, \Delta\theta)$ in both cases lies at around $\theta = \pi/2$, but both the actual value of the minimum energy and the shape of the entire landscape look profoundly different. Additionally, the minimum for the full theory on the left is given by the yellow line with $\Delta\theta = \pi/2$, while the RKKY theory on the right shows a degeneracy with respect to $\Delta\theta$.

Figure 3.8.: Energy per lattice site E/L as a function of θ (x-axis) and $\Delta\theta$ (colored lines) for a system with $L = 128$ at $\varphi = 0.6$ and a. $J = 0.01$ (top row), b. $J = 0.1$ (middle row) and c. $J = 1.0$ (bottom row) in the full Kondo lattice theory with classical spins (left column) and for the effective spin-only theory obtained by RKKY theory (right column).

The RKKY result in the right panel of the middle row with $J = 0.1$ looks qualitatively quite similar to the corresponding full theory on the left. Again, the location of the energy minimum is at ($\theta =$

$\pi/2, \Delta\theta = 0$) compared to ($\theta = \pi/2, \Delta\theta = \pi/2$) in the full theory, but the value of the ground state energy differs by only $\mathcal{O}(10^{-4})$. Even better, and in fact nearly perfect, is the agreement shown in the top row Fig. 3.8 a. for $J = 0.01$. The only difference is again the absence of a spin-dimerized ground state in the framework of the RKKY theory.

Evidently, RKKY theory is not able to capture the spin-dimerized phase at all. This can be seen more clearly by zooming into the top row of Fig. 3.8, which is done in Fig. 3.9. Here, the top row again shows the energy landscape $E(\theta, \Delta\theta)$ again for $J = 0.01$ and $\varphi = 0.6$ as in Fig. 3.8 a., with a zoom into the region of the energy minimum pictured in the bottom row. Clearly, the full theory shows a true minimum for $\Delta\theta = \pi/2$ (yellow line), whereas in the RKKY theory on the right, all lines with $\Delta\theta \in (0, \pi/2)$ lie exactly on top of each other. Hence, higher-order-in-J perturbation theory would have to be invoked to lift this degeneracy and to reproduce the spin-dimerized phase.
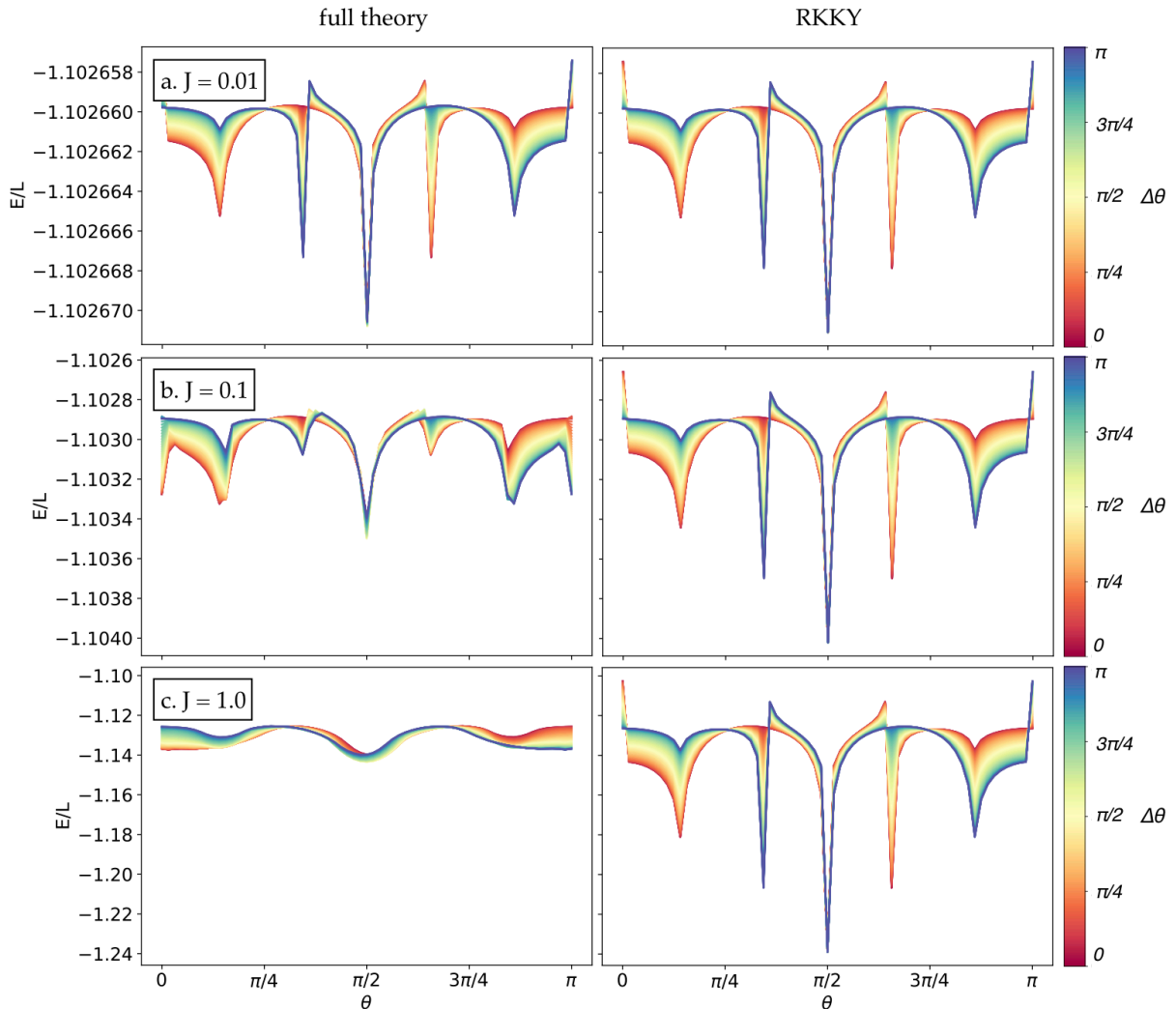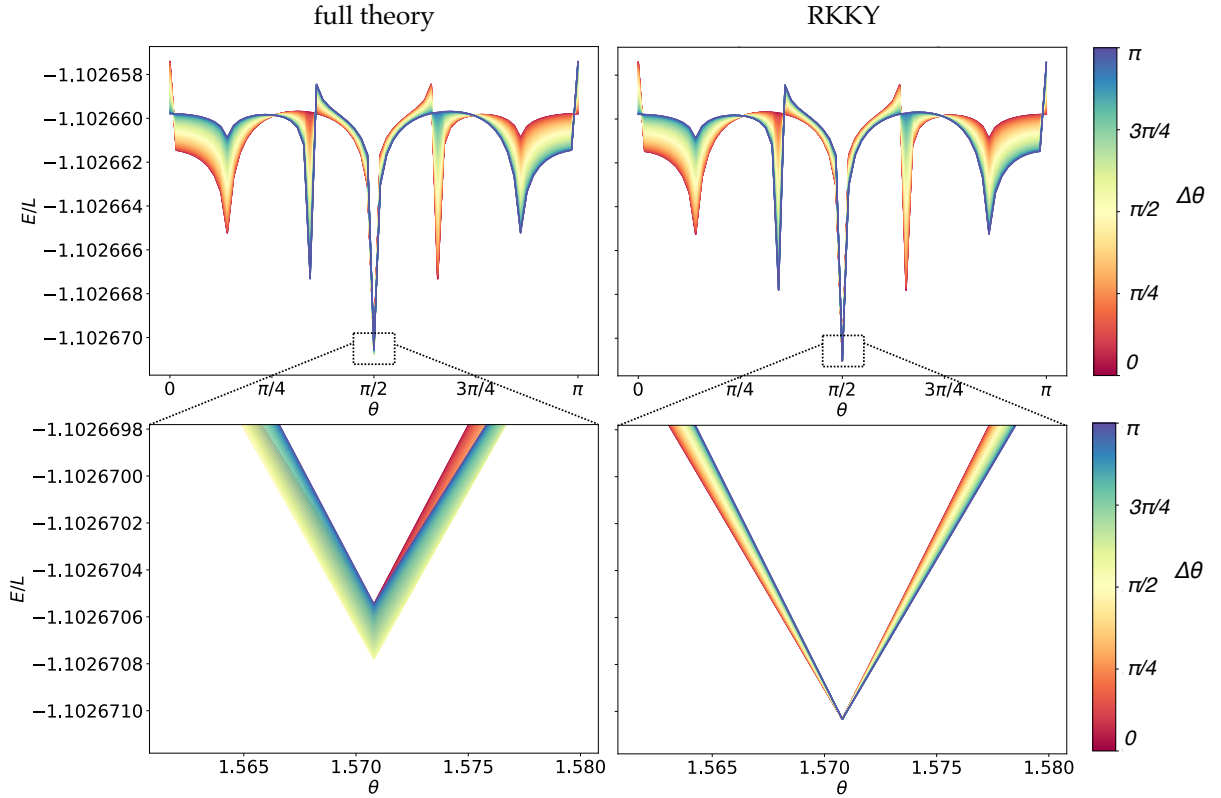

Figure 3.9.: Energy per lattice site E/L as a function of θ (x-axis) and $\Delta\theta$ (colored lines) for a system with $L = 128$ at $\varphi = 0.6$ and $J = 0.01$ in the full Kondo lattice theory with classical spins (left) and for the effective spin-only theory obtained by RKKY theory (right). The bottom row shows a zoom into the minimum of the energy and reveals the corresponding $\Delta\theta$ to be degenerate in RKKY theory and $\Delta\theta = \pi/2$ in the full theory.

The full semiclassical theory predicts a discontinuous transition at $\varphi_c(J)$ between an antiferromagnetic $(\theta = \pi, \Delta\theta = 0)$ and a dimerized state $(\theta = \pi/2, \Delta\theta = \pi/2)$, which are both characterized as local energy minima.

To characterize the course of the transition at weak J, $\varphi_c(J)$ can be expanded for any finite L:

$$\varphi_c(J) = \varphi_0 + \text{const} \times J^2 + \mathcal{O}(J^4) \,. \tag{3.10}$$

As the RKKY Hamiltonian involves a single energy scale only and thus predicts $\varphi_c(J) = \varphi_0 = \text{const}$ (relating to the transition with respect to θ only), the J^2 term is already *beyond* second-order perturbation theory. Note that φ_0 itself is independent of L as this is related to the Lifschitz transition which is L-independent in turn.

To learn more about the transition $\varphi_c(J)$ in general, both energy minima for the two competing phases $(i = 1, 2)$ can be expanded in powers of J:

$$E_i(J, \varphi) = E_{i,0}(\varphi) + J^2 E_{i,1}(\varphi) + J^4 E_{i,2}(\varphi) + \mathcal{O}(J^6) \,. \tag{3.11}$$

For $J = 0$, the total energy does not depend on the spin configuration such that trivially $E_{1,0}(\varphi) = E_{2,0}(\varphi)$. Therefore, the J^2-term of $\varphi_c(J)$ is obtained from the condition $E_{1,1}(\varphi_c) + J^2 E_{1,2}(\varphi_c) = E_{2,1}(\varphi_c) + J^2 E_{2,2}(\varphi_c)$, i.e., one has to go to $\mathcal{O}(J^4)$.

Figure 3.10.: Difference between the total energy of the full semiclassical theory and of the RKKY perturbation theory per site as a function of J^4 in the weak-J regime at $\varphi = 0.4 < \varphi_0$ and for different system sizes as indicated. Inset: Corresponding slope, i.e., the coefficient $\alpha_4 \equiv \lim_{J \to 0}(E(J) - E_{\text{RKKY}})/(LJ^4)$ as a function of L^2.
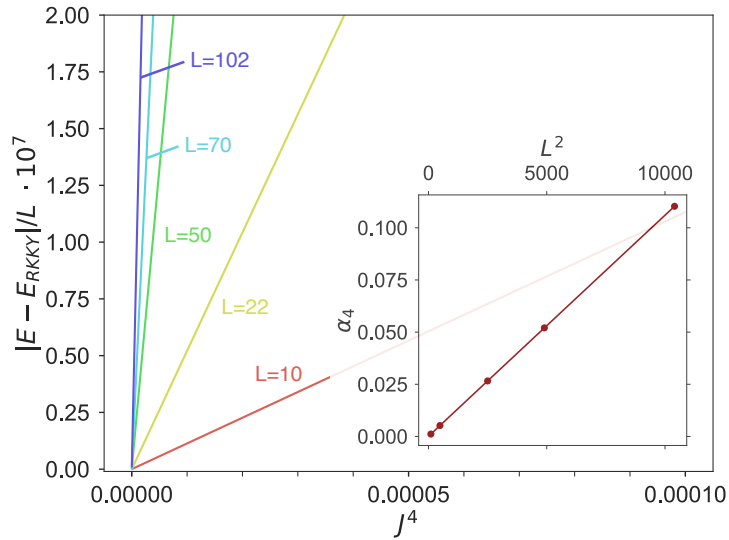
Fig. 3.10 (main figure) demonstrates that RKKY theory is perfectly valid in the weak-J limit for any *finite* system size L. Namely, the difference between the total energy, as obtained from the full semiclassical theory, and the RKKY energy, Eq. (3.9), is zero up to corrections of the order of J^4. For a small system with $L = 10$ sites, for instance, there is almost perfect agreement between $E_{\text{RKKY}}(\theta, \Delta\theta)$ and the exact ground-state energy $E(\theta, \Delta\theta)$ up to $J = 0.5$. In the same J range but for larger lattices with $L = 100$, however, there are qualitative deviations between the RKKY and the exact data for $E(\theta, \Delta\theta)$. In fact, the magnitude of the $\mathcal{O}(J^4)$ correction strongly increases with increasing system size, as can be seen in the main part of Fig. 3.10. This can be quantified by the coefficient $\alpha_4 \equiv E_{1,2}(\varphi)/L = \lim_{J \to 0}(E(J) - E_{\text{RKKY}})/(LJ^4)$, i.e., by the slope of the linear trend with J^4. The inset demonstrates that α_4 diverges as L^2 when $L \to \infty$. This illustrates the breakdown of perturbation theory in the thermodynamical limit. At the order J^2, on the other hand, $\alpha_2 \equiv E_{1,1}(\varphi) = \lim_{J \to 0}(E_{\text{RKKY}} - E_0)/(LJ^2)$, converges to a finite value as $L \to \infty$, as is well known for the free electron gas [48,49]. The logarithmic divergence of $\chi_0(0, k)$ at $k = \pi/2$ is integrable, which implies that the total RKKY energy per site, Eq. (3.6), converges to a finite value in the thermodynamic limit. For the free electron gas in one dimension, one can evaluate Eq. (3.7) analytically and show that [48,49] $\chi_0(\omega = 0, k) \sim \frac{\ln(2k_F - k)}{\ln(2k_F + k)}$. This diverges at $k = 2k_F$. However, in the real-space representation one has $\chi_{ij} \sim \text{Si}(R_i - R_j)$, and the sinc function is integrable from 0 to ∞ such that the total energy of a Hamiltonian of the form $H = L^{-1} \sum_{ij} \chi_{ij} S_i S_j$ stays finite for $L \to \infty$.

Consequently, the J^2-term of $\varphi_c(J)$, see Eq. (3.10), is ill-defined when $L \to \infty$ since it is fixed by a condition involving both α_2 and α_4.

3.2.3. Perturbation Theory Around $t_1 = 0$

At $t_1 = 0$, i.e. $\varphi = \pi/2$, the ground state is given by two decoupled antiferromagnetically ordered chains, where both the dimerized and the incommensurate spiral configurations are degenerate. This is lifted at finite t_1 and produces first-order transitions traced by the line $J_c^{(\text{dim})}(t_1)$, or $J_c^{(\text{dim})}(\varphi)$. Numerically, it can be seen that for $t_1 \to 0$, the line $J_c^{(\text{dim})}(t_1)$ terminates at $J_0 \approx 9.7t$ as shown in the phase diagram, Fig. 3.3. Hoping to gain analytical insight into the phase transition, nondegenerate perturbation theory in t_1 can be used to compute the total energy for a given configuration of the classical spins. The calculation is shown in Appendix B but unfortunately results in a ground state where both the dimerized and $\pi/2$-spiral state are still degenerate. As odd powers of t_1 do not contribute, the degeneracy is lifted, at the earliest, at order t_1^4.

This knowledge can, however still be used to determine properties of the behavior of the line $J_c^{(\text{dim})}(t_1)$. Dimerized states ($i = 1$) with $\Delta\theta = \pi/2$ and spiral states ($i = 2$) with $\Delta\theta = 0$ are given by local minima, whose energy can be expanded in powers of t_1,

$$E_i(J, t_1) = E_{i,0}(J) + t_1^2 E_{i,1}(J) + t_1^4 E_{i,2}(J) + \dots, \tag{3.12}$$

and the degeneracy $E_{1,0}(J) = E_{2,0}(J)$ in the decoupled-chain limit can be exploited. The energy is trivially independent of $\Delta\theta$ and it follows $E_{1,1}(J) = E_{2,1}(J)$. The condition fixing $J_c^{(\text{dim})}(t_1)$ then reads as $E_{1,2}(J_c^{(\text{dim})}) + t_1^2 E_{1,3}(J_c^{(\text{dim})}) = E_{2,2}(J_c^{(\text{dim})}) + t_1^2 E_{2,3}(J_c^{(\text{dim})})$. Consequently, for an analytical computation of J_0 one would have to go $\mathcal{O}(t_1^6)$ at least. In any case, the line can be expanded as follows

$$J_c^{(\text{dim})}(t_1) = J_0 + \text{const.} \times t_1^2 + \mathcal{O}(t_1^4),\tag{3.13}$$

or put differently, $J_c^{(\text{dim})}(\varphi) - J_0 \propto (\varphi - \pi/2)^2$. This is fully consistent with the dotted line in Fig. 3.3 interpolating between the data points.

3.3. Finite Size Analysis

As mentioned in Section 3.1 in the discussion of the ground state phase diagram, the finite size scaling is extremely poor for $J \gtrsim 6$ and $\varphi \gtrsim \pi/4$. The phase boundary φ_c between the spiral and dimerized phase is highly dependent on L for $J \gtrsim 7$ as can be seen in Fig. 3.11, where φ_c is plotted as a function of system size L for different values of J. In Fig. 3.11, φ_c is only converged at $L = 200$ for $J = 6$ and $J = 7$. For all higher J-values, lattices with around $L = 200$ sites falsely show a φ_c value significantly lower than $\pi/2$, i.e. a dimerized phase that extends further than the actual transition shown in Fig. 3.3 for $L = 10^5$.

In order to extrapolate, an expression is needed for the dependence of φ_c on L. Strong coupling perturbation theory as detailed in Section 2.3.2 gives as the optimal spin configuration for $t_1 < 2t_2$

$$\theta = \arccos\left(-\frac{1}{4\tan^2(\varphi)}\right), \quad \Delta\theta = 0,\tag{3.14}$$

where $t_2/t_1 = \tan\varphi$. In an infinite system, θ would be a continuous variable that smoothly approaches $\pi/2$ from above as $\varphi \to \pi/2$ from below. For the actual numerical calculations, performed at finite L and using periodic boundary conditions, θ runs on a discrete θ-grid with spacings of $2\pi/L$. Assuming that the energy as a function of θ can in the immediate proximity of the minimum at $\theta_{\min}$ be approximated as a parabola, the 'wrong' $\theta_{\min}(L \text{ finite})$ can be explained by the finite θ-grid spacing. As $\varphi \to \pi/2$ from below, the optimal θ jumps from $\theta = \pi/2 + 2\pi/L$ to $\theta = \pi/2$ at a certain value $\varphi = \varphi_L < \pi/2$. For large L, φ_L can be determined from the estimate

$$\frac{\pi}{2} + \frac{\pi}{L} = \arccos\left(-\frac{1}{4\tan^2(\varphi_L)}\right).\tag{3.15}$$

Solving for φ_L yields

$$\varphi_L = \arctan\left(\frac{1}{\sqrt{4\sin(\pi/L)}}\right).\tag{3.16}$$

This is plotted in Fig. 3.11 as a dotted line and found to agree well with the result for large J, in particular with $J \geq 20$. Unfortunately, the convergence of φ_L to φ_∞ is very slow. System sizes of about $L \approx 50,000$ would be necessary to determine φ close to $\pi/2$ with an accuracy of better than 1%.
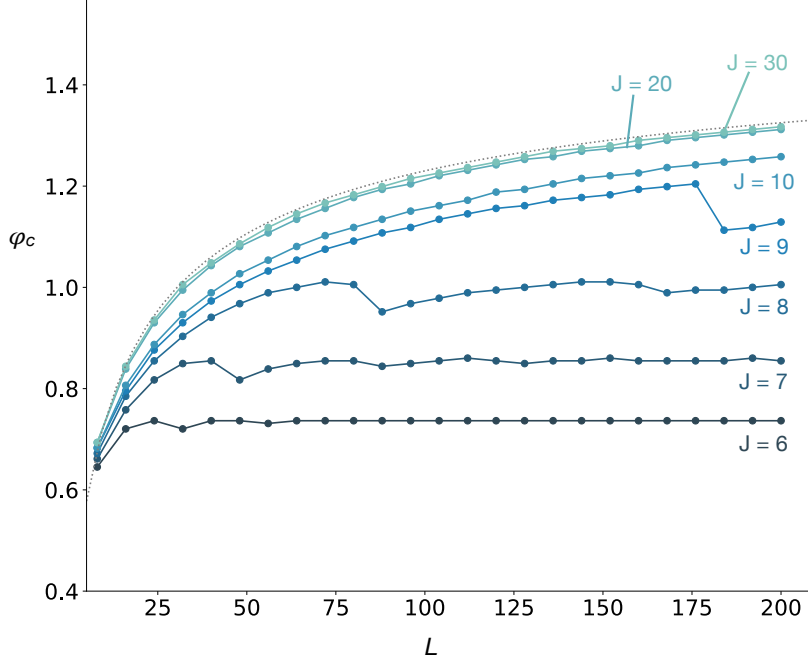
Figure 3.11.: Value of φ_c, i.e. the position of the phase boundary between homogenous and dimerized phase as a function of system size L for different values of J (see colored labels). Dotted line: analytical estimate for $\varphi_c(L) \equiv \varphi_L$, see Eq. (3.16).

As the $\theta - \Delta\theta$ parameter space for each parameter set of (φ, J) is $(L/2) \times (L/4)$ dimensional, simply minimizing $E(\theta, \Delta\theta)$ is clearly not feasible for lattices of size $\mathcal{O}(10^5)$ that are required for convergence of the phase boundary. Each parameter set is independent, an obvious strategy is therefore to parallelize the computation. In particular, as the number of parameter sets is rather large, this seems as an ideal use case for GPU computing. In order to calculate the energy $E(\theta, \Delta\theta)$ according to Eq. (3.1), however, the diagonalization of a $2L \times 2L$ matrix is necessary. For system sizes of $L \approx 10^5$ this is not feasible. Fortunately, as the crude minimization calculations using the entire $\theta - \Delta\theta$ parameter space show, there is only one phase present with $\Delta\theta \neq 0$. To obtain the phase boundary between the dimerized and the homogenous spiral phase, it is thus only necessary to compare two phases and determine the crossover. As detailed in Section 2.2, tackling the problem in k-space only leaves a 4×4-matrix for the dimerized phase and a 2×2 matrix for the homogenous spiral phase to diagonalize per set of parameters. As this is independent of lattice size, this is easily feasible for a standard GPU. Using the CUDA toolkit, it was possible to calculate the phase boundary in Fig. 3.3 for lattices of up to 10^5

lattice sites within a few computing hours. The CUDA calculations in Fig. 3.3 are indicated with black markers and connected with a dotted line.

3.4. Comparison to DMRG Results

This section aims to compare the results of the Kondo lattice with classical spins as presented in this thesis to the full quantum system calculated with the density-matrix renormalization group (DMRG) method, and the related variational uniform matrix product state approach (VUMPS) by Matthias Peschke. Further information can be found in [20,21].

The fundamentals of the Density Matrix Renormalization Group (DMRG) method were published by Steven White in 1992 [50,51] and it has since evolved to become one of the most widely used methods for low dimensional strongly correlated electron systems. An extensive review can be found in [52]. It has remarkable accuracy, for gapped one-dimensional systems, e.g. the spin-1 Heisenberg model, the exact ground state can be computed up to machine precision [53]. The main draw back of DMRG is, that it is not easily generalized for systems of higher dimensions $d > 1$, and while time-dependent extensions do exist, they also suffer from an exponentially growing computational cost with increasing time [54]. Nonetheless, it is one of the most powerful methods available to theoretical solid state physics. In contrast to the semi-classical approximation in the focus of this thesis, the DMRG method is able to describe the full quantum mechanical problem.

An important difference between semiclassical and quantum system is that the ground state of the classical system is expected to exhibit long-range order and is degenerate with respect to global SO(3) rotations of the classical spins, while this is not the case for the quantum mechanical case where quantum fluctuations are present and where the ground state is an isotropic spin singlet. The type of magnetic order found semi-classically, however, is expected to relate to the corresponding type of magnetic short-range order correlations or quasi-long-range (algebraic) magnetic order of the quantum spin case, since the classical-hybrid system comprises the relevant indirect magnetic coupling mechanisms. The antiferromagnetic phase with $\theta = \pi, \Delta\theta = 0$ for the unfrustrated chain ($\varphi = 0$) found for all values of $0 < J < \infty$ corresponds to the quantum mechanical quantum-singlet state with short range antiferromagnetic correlations. The mechanisms responsible - the RKKY indirect magnetic interaction at weak J and the superexchange mechanism at strong J - are present in both theories. Both the semiclassical and quantum-mechanical method also predict the spin dimerized phase.

The phase transition between the AF and the IC phase found semiclassically perfectly matches the shift of the maximum of the spin-structure factor from $Q = \pi$ for $\varphi < \varphi_c(J)$ to $Q < \pi$ for $\varphi > \varphi_c(J)$ in the quantum-spin case as seen in Fig. 3.12. In this regard, spin correlations in the strong-J regime are almost classical. For $J \to \infty$, the φ-dependence of the pitch angle θ of the incommensurate magnetic order can be determined analytically by mapping onto a classical Heisenberg model on the zigzag ladder

as detailed in Section 2.3.2, which is plotted in Fig. 3.12 as a black line, and is in excellent agreement. For $J = 10$ both the classical and DMRG result lie more or less exactly on the analytical perturbation theory line, whereas for $J = 5$ this is only the case for the DMRG results. This is due to the fact that in contrast to the quantum theory, the classical result for θ at $J = 5$ predicts a discontinuous transition from AF to dimerized phase instead of the smooth curve from Af to spiral (IC). Evidently, the magnitude of the transition J_c between dimerized and spiral phase is different in both theories. This is not surprising. Clearly, due to the mean-field character inherent to the classical-spin theory, an identical order of magnitude for the critical parameters cannot be expected. The necessary critical interaction strength for the classical spins $J_{c,class}^{(dim)}$ is expected to be much stronger than $J_c^{(dim)}$, the DMRG value, since mean-field-like and classical approaches tend to overestimate ordering, i.e., dimerization due to absence of quantum fluctuations that act against ordering. Indeed, on the $t_1 = t_2$ line, for example, $6.4t J_{c,class}^{(dim)} \gg J_c^{(dim)} \approx 0.62t$ is found instead, see [20].
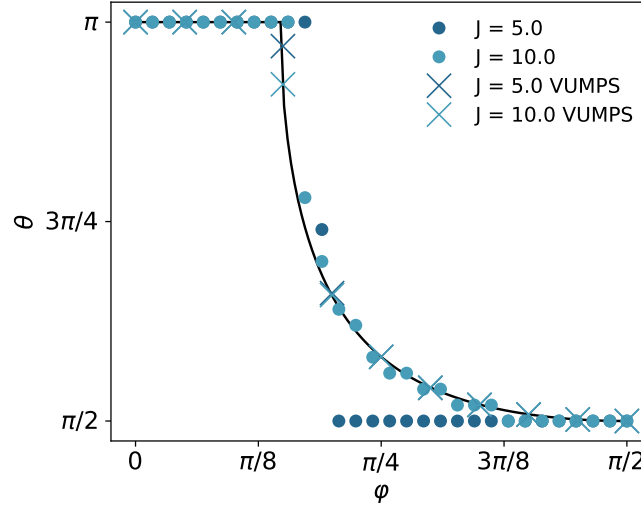
Figure 3.12.: Pitch angle θ of classical spin configuration (circles) as a function of φ compared to the maximum of the spin-structure factor Q of the quantum system calculated with variational uniform matrix product state approach (VUMPS) ($\times$). Black line: analytical result from strong coupling perturbation theory.

The ground-state φ-vs.-J phase diagram as obtained by DMRG calculations is shown in Fig. 3.13. For strong J, there are two different homogeneous phases, one with short-range antiferromagnetic spin correlations characterized by the wave-vector $Q = \pi$ (AF-SRO), and another one with short-range incommensurate (spiral) spin correlations (IC-SRO) characterized by a wave-vector in the range $\frac{\pi}{2} \leq Q < \pi$, at which the spin-structure factor is at its maximum. Both phases are separated by the green line in Fig. 3.13. The green arrow indicates the boundary in the $J \to \infty$ limit.

For weaker interaction strength, $J \lesssim 0.9t$, the spin-structure factor is more complicated such that the "phase boundary" is no longer well defined. In particular, with decreasing J, a second peak grows near $\frac{\pi}{2}$. This is a precursor of a gapless ground state with quasi-long-range $90°$ spiral magnetic order (SP-QLRO, $Q = \frac{\pi}{2}$) which is found at still weaker J (see red line). The transition to this magnetic state, however, is preempted by a spin-dimerized phase (DIM) with spontaneously broken translation symmetry (blue line). This is characterized by alternating ferro- and antiferromagnetic nearest-neighbor correlations on the rungs of the ladder. In the weak-coupling limit the phase transition between the dimerized and the short-range antiferromagnetic states takes place at $\varphi_c(J \to 0) = \arctan(\frac{1}{2}) \approx 0.148\pi$ and exactly coincides with the transition point in the strong-coupling limit $\varphi_c(J \to \infty)$ as is indicated by the dotted line. The system is insulating in the whole phase diagram. Charge excitations are gapped and the momentum-distribution function does not show a singularity.
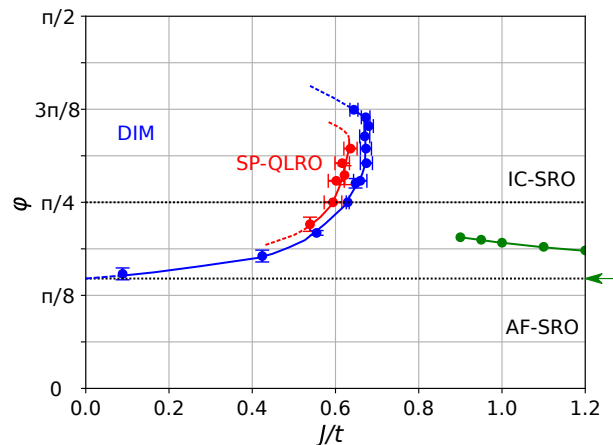
Figure 3.13.: Ground-state phase diagram in the J-φ plane for the half-filled quantum-spin Kondo model on the zigzag ladder, as obtained by DMRG calculations for systems of up $L = 52$ sites (and extrapolated to $L = \infty$) as well as by VUMPS calculations working directly in the thermodynamical limit (with bond dimensions extrapolated to $m = \infty$ where necessary). AF-SRO: antiferromagnetic short-range order with wave vector $Q = \pi$. IC-SRO: incommensurate spiral short-range order with $\pi/2 \le Q < \pi$. DIM: spin-dimerized phase. SP-QLRO: spiral quasi-long-range order, $Q = \pi/2$. Points with error bars locate the various transitions. Black dashes lines: $t_2 = t_1$ (upper) and $t_2 = t_1/2$ (lower). Blue and red dashed lines: see text.

The unfrustrated model at $t_2 = 0$ exhibits short-range antiferromagnetic order with an exponential decay of the spin-correlation function for all $J > 0$ and a finite energy gap to excited states. For finite $t_2 > 0$ and with increasing t_2, antiferromagnetic correlations are more and more frustrated. At $t_2 = t_1$, however, the ground state supports quasi-longe-range antiferromagnetic order at interactions weaker than the critical interaction $J_c^{\mathrm{mag}} \approx 0.84t_1$ (i.e., $J_c^{\mathrm{mag}} \approx 0.594t$, see Fig. 3.13) as done in [20]. In view of the strong geometrical frustrations, this is quite surprising. The magnetic state appears on top

of the spin dimerization, and the magnetic order is given by a $90°$ spin spiral rather than a collinear antiferromagnetic state. The quasi-long-range order is characterized by algebraically decaying spin correlations, by a vanishing spin gap, and by a spin-structure factor diverging at the wave vector $Q = \frac{\pi}{2}$ in the thermodynamic limit. Note that according to the Mermin-Wagner theorem [55] the presence of quantum fluctuations merely excludes true long-range order for the ground state of one-dimensional systems.

In summary, the phase diagram for the quantum-spin case is largely similar to the semi-classical case, but there are important additional effects of quantum fluctuations. Firstly, quantum fluctuations destroy the long-range AF and IC magnetic order but still allow a clear distinction between AF and IC short-range ordered states. Secondly, spin dimerization is strongly suppressed by quantum fluctuations, such that the spin-dimerized phase extends towards by an order of magnitude weaker interaction strengths J only. Moreover, in the quantum model, the line $\varphi_c^{(\dim)}(J)$ cannot terminate at a finite critical J on the $t_1 = 0$ axis, contrary to the classical-spin case, since the ground state is unique and fully gapped, unlike the classical-spin case where the global SO(3) spin-rotation symmetry leads to an infinite ground-state degeneracy. Apart from φ_0, which marks the termination point of $\varphi_c^{(\dim)}(J)$ for $J \to 0$, not only in the classical but also in the quantum-spin case, there is no second critical point of the noninteracting bandstructure in the range $0 < \varphi < \frac{\pi}{2}$, so that it seems likely that $\varphi_c^{(\dim)}(J) \to \frac{\pi}{2}$ for $J \to 0$ represents the second termination point on the $J = 0$ axis. Finally, there is no well-defined triple point in the quantum-spin case. With decreasing J, the boundary $\varphi_c^{(\dim)}(J)$ becomes less and less well defined, and a second peak grows in the spin-structure factor at $Q \gtrsim \frac{\pi}{2}$, which is a precursor of the spiral ($Q = \frac{\pi}{2}$) phase at still weaker J.

An important difference between the Kondo model on the zigzag ladder for classical and for quantum spins is also the different methods of dealing with the magnetic frustration. For strong J and sufficiently strong t_2, i.e., in the moderately frustrated regime, incommensurate (long- or short-range) order represents the preferred compromise in both cases. While the ground state of the classical-spin model supports long-range magnetic order in the entire J-φ plane with different collinear or noncollinear magnetic structures, quantum fluctuations entirely destroy magnetic long-range order in the quantum-spin case. It is surprising, however, that quasi-long-range magnetic order with algebraic decay of the spin correlations is realized in a parameter regime (weak J and strong t_2) of the quantum-spin model where frustration is expected to be dominant. Frustration in a way appears to *favor* magnetic order as far as possible to be consistent with the Mermin-Wagner theorem. To understand this effect, it is instructive to see that the quasi-long-range spiral ($Q = \frac{\pi}{2}$) order, SP-QLRO, only shows up *within* the spin-dimerized phase and that the phase boundary of the SP-QLRO phase closely follows the boundary for the onset of dimerization. Spin dimerization is thus the main reaction of the system to magnetic frustration in this parameter regime while magnetic order is favored as a secondary effect. Hence, SP-QLRO appears as an epiphenomenon that necessarily requires the alleviation of frustration due to a dimerized spin structure which mimics an unfrustrated bipartite lattice.

4. Real-Time Dynamics

In the previous chapter, the equilibrium phase diagram for a Kondo lattice model on the zigzag chain was calculated with the localized moments $\mathbf{S}_i$ considered as classical angular momentum vectors. This allowed a straight-forward calculation of the ground state energy in the entire relevant parameter space and showed the existence of a spin-dimerized phase previously found with quantum mechanical DMRG calculations [20]. The latter, covering a wealth of non-trivial quantum effects, is of course a much more computationally intensive method that in addition is challenged by conceptual limitations in particular for highly entangled problems[1]. Nonetheless it is for all intents and purposes an *exact* method that covers all relevant aspects of low temperature quantum physics. The semi-classical method was able to capture the most central results, i.e. the existence of a dimerized phase, but lacked the purely quantum effects that are also present. But besides a more economical use of computing resources the use of the classical approximation is also justified in materials where local moments do behave approximately classical, due to for example a large spin quantum number S.

The real moment to shine for the classical approximation, however, is not the calculation of the ground state, but the ensuing real-time dynamics. A complete set of non-linear first order differential equations can be found to describe the real-time dynamics of the entire quantum-classical-hybrid system. There is in principle no limit to system sizes or propagation times, except naturally the availability of computational resources. This is a clear advantage over methods that suffer from conceptional difficulties, such as the infamous Monte-Carlo sign problem (e.g. [57]) or truncation errors in DMRG (e.g. [54]).

This chapter is devoted to the study of several non-equilibrium phenomena of the semi-classical Kondo lattice on the zigzag ladder that was previously introduced. The method of choice to lift the system out of equilibrium will be the concept of so-called *parameter quenches*, meaning a sudden global change in some parameter value. The subsequent analysis will be organized as follows: First the equations of motions and numerical methods are introduced in Section 4.1, then the dynamics will be studied following several different parameter quenches that can be separated into two regimes according to the amount of energy introduced by the quench. Section 4.2 covers low-energy quenches with the discovery of an ergodicity threshold and a discussion including aspects from classical mechanics and the derivation of linearized equations of motion. This section also includes a short interlude with an analysis of the integrability of the $J_1 - J_2$-Heisenberg model and its applicability to the Kondo lattice.

---

[1]For details on the DMRG method, refer for example to [56]

Finally, the last part of this chapter, Section 4.3, examines the thermal phase transition connected to spontaneous (discrete) symmetry breaking and emergence of long-range dimer order as well as general remarks on the thermalization properties of results obtained in this thesis.

4.1. Method and Formalism

4.1.1. Equations of Motion

In classical mechanics, an observable $A(q, p, t)$ is a real-valued function on $6n$-dimensional phase space. The *Poisson bracket* between arbitrary observables A and B in canonical basis (q_i^α, p_i^α), $\alpha \in (x, y, z), i \in (1, n)$ is defined as

$$\{A, B\} = \sum_{i\alpha} \left(\frac{\partial A}{\partial q_i^\alpha} \frac{\partial B}{\partial p_i^\alpha} - \frac{\partial A}{\partial p_i^\alpha} \frac{\partial B}{\partial q_i^\alpha} \right) , \tag{4.1}$$

and can be used to express the time evolution of $A(t)$ as

$$\frac{\mathrm{d}}{\mathrm{d}t} A(t) = \{A(t), H_{class}\} , \tag{4.2}$$

where H_{class} is the classical Hamiltonian function [58]. Here, the relevant classical observables are the classical spins $\mathbf{S}_i$. Their dynamics is the same as angular momentum vectors and for the purpose of deriving the according equations of motion, they can be expressed in terms of canonical coordinates and momenta as $\mathbf{S}_i = \mathbf{q}_i \times \mathbf{p}_i$. This can now be used to simplify Eq. (4.1) for spin-dependent functions to

$$\{A(\mathbf{S}), B(\mathbf{S})\} = \mathbf{S} \cdot \frac{\partial A}{\partial \mathbf{S}} \times \frac{\partial B}{\partial \mathbf{S}} . \tag{4.3}$$

The classical Hamiltonian is here obtained by taking the expectation value of the quantum mechanical Hamilton operator $H_{class} \equiv \langle H \rangle$. Using this and Eqs. (4.2) and (4.3), the equations of motion for the classical spins can now be derived as

$$\begin{aligned} \frac{\mathrm{d}}{\mathrm{d}t} \mathbf{S}_i(t) &= \{\mathbf{S}_i(t), \langle H \rangle\} = \frac{\partial \langle H \rangle}{\partial \mathbf{S}_i} \times \mathbf{S}_i \\ &= J \langle \mathbf{s}_i \rangle_t \times \mathbf{S}_i(t) , \end{aligned} \tag{4.4}$$

where the subscript $\langle \cdot \rangle_t$ denotes the fact that of course $\langle \mathbf{s}_i \rangle$ is itself time-dependent.

The conduction electron system, on the other hand, cannot be considered as classical. The corresponding quantum mechanical version of Eq. (4.2) for the time evolution of an observable $A(t)$ with the

Hamilton operator[2] H is the Heisenberg equation of motion

$$i\frac{\mathrm{d}}{\mathrm{d}t}A(t) = [A(t), H] \, , \tag{4.5}$$

where $[\cdot, \cdot]$ denotes the quantum mechanical analogue to the Poisson bracket, i.e. the commutator. The equations of motion for the electron spins $\mathbf{s}_i = \frac{1}{2}\sum_{\sigma\sigma'} c_{i\sigma}^\dagger \boldsymbol{\sigma}_{\sigma\sigma'} c_{i\sigma'}$ can therefore be derived as

$$\begin{aligned}
\frac{\mathrm{d}}{\mathrm{d}t}\langle\mathbf{s}_i\rangle_t &= -i\langle[\mathbf{s}_i, H]\rangle_t \\
&= J\,\mathbf{S}_i(t) \times \langle\mathbf{s}_i\rangle_t - \frac{i}{2}\sum_j t_{ij}\left(\langle c_{i\sigma}^\dagger \boldsymbol{\sigma}_{\sigma\sigma'} c_{j\sigma'}\rangle_t + \text{h.c.}\right) \, .
\end{aligned} \tag{4.6}$$

Note that as $\langle c_{i\sigma}^\dagger \boldsymbol{\sigma}_{\sigma\sigma'} c_{j\sigma'}\rangle_t$ is also time-dependent, Eq. (4.4) and Eq. (4.6) together do not form a closed set of equations. To capture the dynamics of all electronic degrees of freedom, it is convenient to use the one-particle density matrix ρ with elements

$$\rho_{ii'\sigma\sigma'} = \langle c_{i'\sigma'}^\dagger c_{i\sigma}\rangle \, . \tag{4.7}$$

It is calculated as

$$\boldsymbol{\rho} = \Theta(-\mathbf{t}_{\text{eff}}) = \mathbf{V}\Theta(-\boldsymbol{\epsilon})\mathbf{V}^\dagger \, , \tag{4.8}$$

where $\mathbf{t}_{\text{eff}}$ is the effective hopping matrix with elements

$$t_{\text{eff},ii'\sigma\sigma'} = t_{ii'}\delta_{\sigma\sigma'} + \frac{J}{2}(\boldsymbol{\sigma}\mathbf{S}_i)_{\sigma\sigma'}\delta_{ii'} \, , \tag{4.9}$$

ϵ is a diagonal matrix containing its eigenvalues with corresponding eigenvectors $\mathbf{V}$ obtained by the diagonalization $\mathbf{t}_{\text{eff}} = \mathbf{V}\epsilon\mathbf{V}^\dagger$, and Θ is the Heaviside step function.

The equation of motion for the one-particle density matrix can be derived from the time-dependent Schrödinger equation and is called *von Neumann* or *Liouville-von Neumann equation*:

$$i\frac{\mathrm{d}\boldsymbol{\rho}(t)}{\mathrm{d}t} = [\mathbf{t}_{\text{eff}}(t), \boldsymbol{\rho}(t)] \, . \tag{4.10}$$

The formal solution is given by

$$\boldsymbol{\rho}(t) = \mathbf{U}\boldsymbol{\rho}_0\mathbf{U}^\dagger \, , \tag{4.11}$$

---

[2]For simplicity, none of the operators here will be denoted with $\hat{\cdot}$, this should be clear from context alone.

where the unitary time-evolution propagator $\mathbf{U}$ is defined as

$$\mathbf{U}(t) = \mathcal{T} \exp\left(-i \int_0^t \mathbf{t}'_{\text{eff}}(\tau) d\tau\right) \tag{4.12}$$

with time-order operator $\mathcal{T}$ and possibly - in case of parameter quenches - modified effective hopping matrix t'_{eff}. The initial condition is

$$\boldsymbol{\rho}_0 = \Theta(-\mathbf{t}_{\text{eff},0}) \, . \tag{4.13}$$

Together, Eqs. (4.4) and (4.10) describe the dynamics of the entire coupled quantum-classical system. It can be easily seen that they respect the conservation of

- *total particle number*, where of course classical spins are fixed to one spin per lattice site, thus the total number of electrons is also separately conserved, i.e.

$$\frac{\mathrm{d}}{\mathrm{d}t}\langle N_{\text{tot}}^{cc}\rangle = \frac{\mathrm{d}}{\mathrm{d}t}\text{Tr}[\boldsymbol{\rho}(t)] = 0 \, , \tag{4.14}$$

- *total energy*

$$\frac{\mathrm{d}}{\mathrm{d}t}E_{\text{tot}} = \frac{\mathrm{d}}{\mathrm{d}t}\text{Tr}[\boldsymbol{\rho}(t) \cdot \mathbf{t}_{\text{eff}}] = 0 \, , \tag{4.15}$$

- and *total spin*, i.e. sum of classical and electron spins $\mathbf{S}_{\text{tot}} = \sum_i (\mathbf{S}_i + \langle \mathbf{s}_i\rangle)$

$$\frac{\mathrm{d}}{\mathrm{d}t}\mathbf{S}_{\text{tot}} = \frac{\mathrm{d}}{\mathrm{d}t}\sum_i\left(\mathbf{S}_i + \frac{1}{2}\sum_{\sigma\sigma'}\boldsymbol{\sigma}_{\sigma\sigma'}\rho_{ii\sigma'\sigma}\right) = 0 \, . \tag{4.16}$$

As a side note, it can be easily seen by explicitly calculating the time derivative of Eq. (4.11) with $\boldsymbol{\rho}_0 \equiv$ const. and recognizing that the time evolution operator $\mathbf{U}$ itself satisfies a time dependent Schrödinger equation, that the diagonal elements of $\boldsymbol{\rho}$ (in molecular physics sometimes called *populations* or natural occupations) are also time-independent.

4.1.2. Initial Conditions and Numerical Remarks

The coupled non-linear first order differential equations Eqs. (4.4) and (4.10) constitute an initial value problem of the form

$$\dot{y}(t) = f(y(t)), \quad \text{with} \quad t \geq t_0, \quad \text{and} \quad y(t_0) \equiv y_0 \, , \tag{4.17}$$

where $y : \mathbb{R} \to \mathbb{R}^n$ is vector-valued.

Here, the solution of the ode system is implemented using an explicit Runge-Kutta method of order 5(4) that is part of the scipy library [59,60]. The term order 5(4) means the error is controlled assuming

accuracy of the fourth-order method, but steps are taken using the fifth-order accurate formula. More on Runge-Kutta methods in general can be found in [61]. The numerical results respect the conserved quantities in Eqs. (4.14) to (4.16). In Fig. 4.1 an example is plotted for a typical time evolution up to $\mathcal{O}(10^4)$ time steps. The unit of time is chosen as one inverse hopping matrix element t^{-1}, where t comes from the nearest and next-to-nearest neighbor hopping $t_1 = t\cos\varphi$ and $t_2 = t\sin\varphi$. An important side note is, that whenever time steps t - here and from now on t will denote time and not hopping matrix element - are explicitly mentioned in this thesis, they are always understood to be "true" time steps in the before mentioned units, not *Runge-Kutta-time steps*.
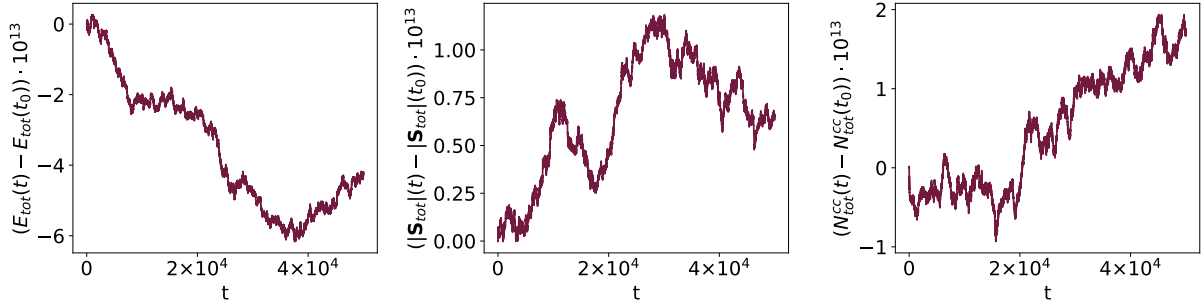

Figure 4.1.: Variation in total energy (left), total spin (middle) and total particle number (right) plotted for $5 \cdot 10^4$ time steps in units of inverse hoppings for a typical time evolution for a system with $L = 8$, $J = 3$ and $\varphi = 0.0$. Note the scale on the vertical axis.

Fig. 4.1 shows the difference between total energy at time t and its initial value at time t_0 (left panel) and its analogue for total spin length (middle panel) and total (electron) particle number (right panel). It can be seen that all are conserved up to machine precision.

An initial state that is also the ground state will not trigger any dynamics. For interesting non-equilibrium observations, the system will thus have to be excited in one way or another. There are of course numerous methods to achieve this, but here the focus will be on parameter quenches. In contrast to a ramp or adiabatic change, the premise of a parameter *quench* is a sudden change in parameter at the very beginning of the time evolution. The equilibrium phase diagram from Chapter 3 allows for several possible interesting quench set-ups, but the focus here will be mainly on two different kinds as illustrated in Fig. 4.2.

Section 4.2 will cover both φ- and J-quenches within the antiferromagnetic phase as marked with ① in orange in Fig. 4.2. The topic of the final section of this thesis, Section 4.3, will be quenches either crossing the AF-DIM or IC-DIM phase boundary as drawn with ② in purple in Fig. 4.2. For all results presented here, initial spin configurations $\{\mathbf{S}\}$ that are collinear, i.e. antiferromagnetic (AF) or dimerized (DIM), are chosen to lie in x-direction. Spiral (IC) configurations are initially taken to lie in the $x-y$-plane. Because dimerized spin configurations only "fit" into lattices with $L = 4 \cdot n$, $n \in \mathbb{N}$

due to periodic boundary conditions, the lattice sizes within this thesis are all chosen accordingly.
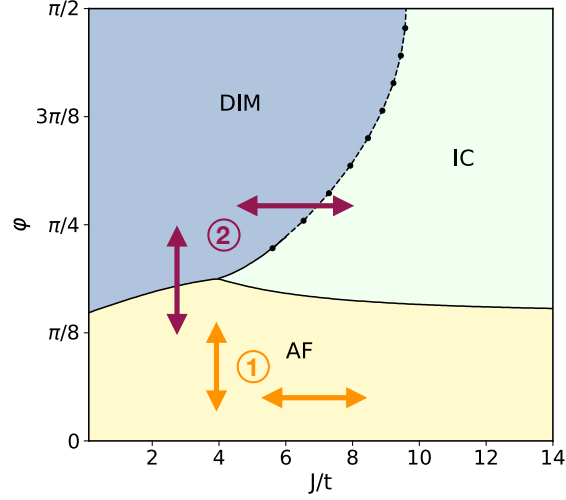

Figure 4.2.: Phase diagram of the semiclassical Kondo lattice on the zigzag chain with schematic illustration of quenches investigated within this thesis. 1) (orange): φ-or J-quenches within the antiferromagnetic phase. 2) (purple): φ- or J-quenches across the AF-DIM or IC-DIM phase boundary.

Before the discussion of results in the succeeding sections, a short comment on initiating dynamics is warranted. The first thing to note is that by construction, the electron spins are initially always collinear to the classical spins, i.e. $\langle \mathbf{s}_i \rangle \, || \, \mathbf{S}_i \; \forall \, i \in (1, \ldots, L)$, since they are explicitly calculated to be in equilibrium to the respective spin configuration, see Eq. (4.8). Remembering the equations of motion

$$\frac{\mathrm{d}}{\mathrm{d}t} \mathbf{S}_i(t) = J \langle \mathbf{s}_i \rangle_t \times \mathbf{S}_i(t) \tag{4.18}$$

and

$$\frac{\mathrm{d}}{\mathrm{d}t} \langle \mathbf{s}_i \rangle_t = J \, \mathbf{S}_i(t) \times \langle \mathbf{s}_i \rangle_t - \frac{i}{2} \sum_{j\sigma\sigma'} t_{ij} \left(\langle c_{i\sigma}^\dagger \boldsymbol{\sigma}_{\sigma\sigma'} c_{j\sigma'} \rangle_t - \mathrm{h.c.} \right) , \tag{4.19}$$

it is clear that the terms $\propto \langle \mathbf{s}_i \rangle \times \mathbf{S}_i$ are thus initially zero. This implies that Eq. (4.18) vanishes entirely whereas all that remains of Eq. (4.19) is the second term on the right hand side. As $\langle \mathbf{s}_i \rangle \, || \, \mathbf{S}_i$, this part of Eq. (4.19) will initially also be collinear to the classical spins. The only possible motion is therefore constrained to longitudinal motion of $\langle \mathbf{s}_i \rangle$ the direction of the initial collinear spin configuration!

This would of course hardly merit the discussion for an entire chapter of this thesis. The (numerical) reality, however, is that the spins - both classical and electronic - *can* escape this constraint. Whether this happens or not is a non-trivial property of the system that is deeply connected to the topics covered in Section 4.2. In short, dynamics can either be *chaotic* or *regular*, where the former is expected to be far more common. A more detailed discussion can be found in the following section. For now, the

only relevant statement is that *deterministic chaos*, i.e. chaotic motion following from deterministic equations of motion, can be defined by the presence of exponential sensitivity on small perturbations [62]. Double precision on regular computing machines is of order $\mathcal{O}(10^{-12})$, in case of chaotic motion this should therefore be enough to eventually start dynamics.

Fig. 4.3 confirms this. Plotted are the absolute values of the x-components of the classical spins $\mathbf{S}_i$ following a φ-quench from $\varphi_{ini} = 0.3$ to $\varphi_f = 0.8$ at $J = 3$ for a system of size $L = 128$ for the first 80 time steps. There appears to be a rather long period without any dynamics, until at around $t = 50$ the motion starts to become chaotic. Zooming into the seemingly flat lines as shown in the inset even reveals the trajectories to deviate much earlier, hinting at the exponential sensitivity on the accumulating numerical error. As there is no laboratory in the world that could provide experimental conditions free of such perturbations that can start the dynamics, this is not to be regarded as unphysical. There is not much to be learned from it either, apart from the already mentioned power to decide about the chaotic (or in contrast: regular) nature of the motion. This initial period will therefore often be omitted from plots, particularly in Section 4.3 where all featured dynamics are chaotic.
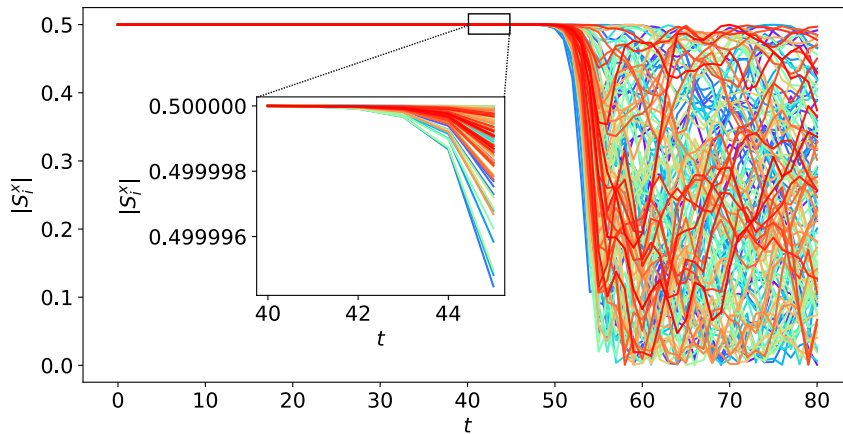
Figure 4.3.: Initial trajectories of $|S_i^x|$ after a quench $\varphi = 0.3 \to 0.8$ for $J = 3$ and $L = 128$. The inset shows a zoom that illustrates the exponential sensitivity on small perturbations (here: numerical inaccuracy).

4.2. Ergodicity Threshold

Incidentally, not all dynamical systems show chaotic behavior as that displayed in Fig. 4.3. There are of course further subtleties, but roughly speaking, the absence of chaos is an indication of a so-called *integrable* system. The following definitions and discussion will be focused on *classical* mechanics, because even though considered here is a quantum-classical hybrid system, for the purposes of this thesis the main interest lies in the dynamics of the classical spins. It should also be noted, that by

defining appropriate Poisson-Brackets, the dynamics of the entire hybrid system can be mapped exactly onto a purely classical system with $\mathcal{O}(L^2)$ degrees of freedom [63].

Within the Hamiltonian framework, each degree of freedom is connected to two independent quantities: position and momentum. A state of a system with n degrees of freedom therefore lives in $2n$-dimensional phase space. If the total energy is a constant of motion, the system is said to be conservative and all its trajectories lie on a $(2n - 1)$-dimensional hypersurface in phase space. If - after potentially long but finite times - a trajectory passes arbitrarily close to every point on this hypersurface, it is called *ergodic*. This is an important concept in statistical mechanics, where only for ergodic systems the connection between dynamical and ensemble-based description can be made in form of the *ergodic hypothesis*

$$\langle A \rangle_T = \lim_{T \to \infty} \frac{1}{T} \int_0^T A(x(t)) \, \mathrm{d}t \;\; \overset{!}{=} \int_\Omega A(x) \, \rho(x) \, \mathrm{d}x = \langle A \rangle_\rho \tag{4.20}$$

that relates the long-time average to ensemble average of an observable A which depends on some set of degrees of freedom $x(t)$ that are distributed in phase space Ω according to the equilibrium probability distribution ρ [64]. In a mathematical sense, the ergodic hypothesis can be expressed in the language of measure theory [65]. Note that ergodicity is necessary but not sufficient for chaotic dynamics as will be explained shortly.

There are multiple definitions of integrable systems, an overview can be found for example in [66]. Most common is perhaps integrability "in the Liouville sense", where a system is called integrable, if it possesses as many constants of motion I_i as degrees of freedom n that are independent and in involution, i.e. $\{I_i, I_j\} = 0$ for any $i, j = 1, \ldots, n$, where $\{\cdot, \cdot\}$ is the Poisson bracket defined in Eq. (4.1). Such a system is called integrable, because it can be solved by "reduction to quadratures", i.e. n independent integrations [67].

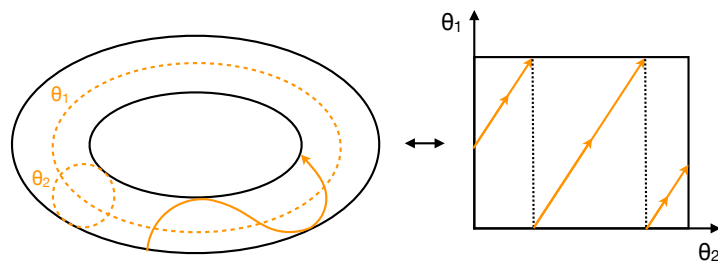**Figure 4.4.:** Schematic illustration of the mapping of a trajectory on a 2-torus onto a square. After [68].

The constants of motion constrain the dynamics of an integrable system even further, such that all trajectories lie on n-dimensional invariant tori that for completely integrable systems cover the entire phase space. Any trajectory will stay on the same torus, determined by initial conditions, indefinitely

and can be described in terms of angle variables θ_i, as pictured in Fig. 4.4 for $n = 2$. Let $\theta_1 = \omega_1 t + \theta_{10}$ and $\theta_2 = \omega_2 t + \theta_{20}$. If the ratio of the frequencies ω_1 / ω_2 is commensurate, i.e. a rational number, then the orbit on the torus is closed and the motion *periodic*. If it is incommensurate, on the other hand, the motion is *quasi-periodic* and never exactly repeats itself. This is clear from Fig. 4.4, where the 2-torus is unfolded into a square with periodic boundary conditions. In this case, the trajectory becomes a series of parallel lines. It is immediately clear, that should the frequencies be incommensurate, they cover the torus densely for $t \to \infty$ [68]. In this sense, the motion on the torus is ergodic, i.e. Eq. (4.20) holds [69]. True statistical properties can therefore only be achieved by ergodicity *and* chaos. The latter property is often called *mixing*, with the most important indication being independence on initial conditions [68].

Even though much research has been devoted to them over the last decades, integrable systems are exceptionally rare and in fact are said to "form a set of measure zero" [68]. As of yet, there is no general mechanism known that can determine the integrability of a system. Still, there is no indication that the system considered here is integrable, and any dynamics following a parameter quench is therefore expected to be mixing. This is in fact not the case. The following section focusses on φ- and J-quenches within the antiferromagnetic phase as illustrated in the overview of the phase diagram in Fig. 4.2 in orange and denoted with ①. Contrary to expectations, a finite energy barrier is found below which the system is not mixing on any observable time scales.

4.2.1. Numerical Observations

Any parameter quench introduces energy into the system. This is intuitively clear, but can also be expressed more concretely. In Section 4.1.1, the one-particle density matrix $\boldsymbol{\rho}$ was introduced, that describes the state of the electron system coupled to the classical spins. With this notation, the energy of the system for fixed spin configuration $\{\mathbf{S}\}$ can be expressed as a function of exchange coupling J and frustration φ as

$$E(J, \varphi) = \mathrm{Tr} \left[\boldsymbol{\rho}(J, \varphi) \cdot \mathbf{t}_{\mathrm{eff}}(J, \varphi) \right] , \qquad (4.21)$$

with effective hopping matrix $\mathbf{t}_{\mathrm{eff}}$ as defined in Eq. (4.9). Let $\boldsymbol{\rho}_0 \equiv \boldsymbol{\rho}(J_{\mathrm{ini}}, \varphi_{\mathrm{ini}})$ be the density matrix describing the initial state with parameters $J_{\mathrm{ini}}, \varphi_{\mathrm{ini}}$. This initial state is then propagated with a time evolution propagator $\mathbf{U}(\mathbf{t}'_{\mathrm{eff}})$ as introduced in Eq. (4.12) with a quenched effective hopping matrix $\mathbf{t}'_{\mathrm{eff}}(J_{\mathrm{f}}, \varphi_{\mathrm{f}})$ that depends on new parameters $J_{\mathrm{f}}, \varphi_{\mathrm{f}}$. The total energy after the quench is therefore given by

$$E_{\mathrm{f}} = \mathrm{Tr} \left[\boldsymbol{\rho}_0 \cdot \mathbf{t}'_{\mathrm{eff}} \right] . \qquad (4.22)$$

The interesting quantity, however, is only the difference to the ground state energy. This can be viewed as an "effective temperature", although such terminology is dangerous as the relationship between

energy and temperature is unknown for this system. Let

$$E_{0,f} = \text{Tr} \left[\boldsymbol{\rho}_f \cdot \mathbf{t}'_{\text{eff}} \right] \tag{4.23}$$

denote the ground state energy at the point in parameter space given by the after-quench parameters J_f, φ_f, with $\boldsymbol{\rho}_f \equiv \boldsymbol{\rho}(J_f, \varphi_f)$. Then, the additional - or excitation - energy introduced by the parameter quench is given by

$$\Delta E = E_f - E_{0,f}. \tag{4.24}$$

The focus in this section is on parameter quenches within the antiferromagnetic phase. Fig. 4.5 shows the energy introduced by a quench $\Delta\varepsilon = \Delta E / L$ for a final state within the antiferromagnetic phase (here: $J_f = 3$, $\varphi_f = 0.4$) as a function of initial parameters $J_{\text{ini}}, \varphi_{\text{ini}}$ for a φ-quench (left panel), where $J = \text{const.}$, and a J-quench (right panel), where $\varphi = \text{const.}$.
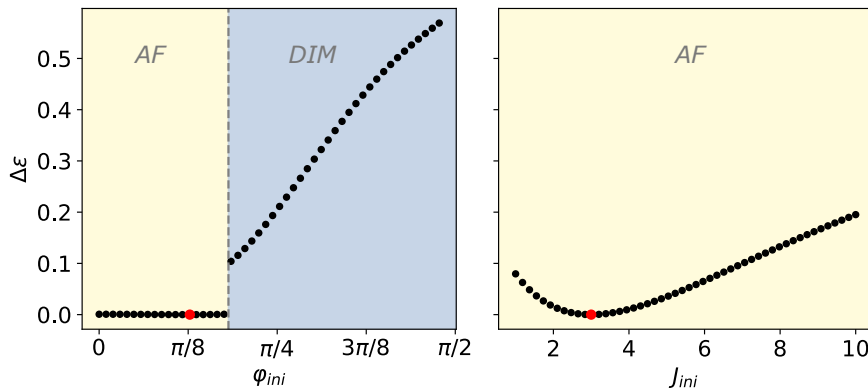

Figure 4.5.: Energy introduced by a φ-quench (left) and J-quench (right) $\Delta\varepsilon = \Delta E / L$ as a function of initial parameters $\varphi_{\text{ini}}, J_{\text{ini}}$. Final state in both cases is $J_f = 3$, $\varphi_f = 0.4$ as indicated by red dots. In the left panel, the dashed line shows the position of the equilibrium phase transition AF-DIM.

The right panel, where $\Delta\varepsilon$ is plotted for the J-quench, shows a a parabolic minimum around J_f, as might have been predicted - the expectation is certainly, that any quench with a finite $\Delta J = |J_f - J_{\text{ini}}|$ should lead to a finite $\Delta\varepsilon > 0$. The φ-quench plotted on the left, however, reveals a peculiarity of the antiferromagnetic phase. Apparently, $\Delta\varepsilon \approx 0$ for all $\Delta\varphi = |\varphi_f - \varphi_{\text{ini}}| > 0$ that lie within the φ-range with antiferromagnetic ground state. φ-quenches within the antiferromagnetic phase are thus "quasi-adiabatic" and do not cost energy, i.e. excite the system. This is not due to a symmetry of the model and cannot be proved analytically, $\Delta\varepsilon$ is also not *exactly* zero but of order $\mathcal{O}(10^{-4})$, well above numerical accuracy. Nevertheless, unexpectedly, it is found that $E_{0,f} \approx E_f$ as long as $J = \text{const.}$ and both $\varphi_f, \varphi_{\text{ini}}$ lie within the antiferromagnetic region of the phase diagram.

At the position of the equilibrium phase transition between antiferromagnetic and dimerized phase,

indicated by a dashed line and color-change in Fig. 4.5, there is a discontinuity in $\Delta\varepsilon(\varphi_{\mathrm{ini}})$ as well as a qualitative behavior change. φ-quenches are no longer quasi-adiabatic but cost an energy proportional to the size of the quench $\Delta\varphi$. As $E_{0,\mathrm{f}} = \mathrm{const.}$ in this plot, because $\Delta\varepsilon$ is plotted as a function of φ_{ini} on which $E_{0,\mathrm{f}}$ does not depend, the discontinuity must be present in E_{f} and the result of calculating the expectation value of a Hamiltonian in a state that depends on other parameters.

As suggested by the independence of the quench energy $\Delta\varepsilon$ on φ within the AF phase in the left panel of Fig. 4.5, a φ-quench does indeed not induce any noticeable dynamics. For a more compact visualization of the dynamics, instead of plotting every spin- and electron component separately, the focus is on the staggered magnetization per site

$$\mathbf{m}_{\mathrm{s}} \equiv \mathbf{M}_{\mathrm{s}}/L \quad \text{where} \quad \mathbf{M}_{\mathrm{s}} = \sum_{i=1}^{L}(-1)^{i}\,\mathbf{S}_{i}\,, \tag{4.25}$$

which can be defined in the electron system as

$$\langle\mathbf{m}_{\mathrm{s}}^{\mathrm{cc}}\rangle \equiv \langle\mathbf{M}_{\mathrm{s}}^{\mathrm{cc}}\rangle/L \quad \text{where} \quad \langle\mathbf{M}_{\mathrm{s}}^{\mathrm{cc}}\rangle = \sum_{i=1}^{L}(-1)^{i}\,\langle\mathbf{s}_{i}\rangle\,. \tag{4.26}$$

The staggered magnetization for both classical spins and electrons are plotted in Fig. 4.6 for a φ-quench from $\varphi_{\mathrm{ini}} = 0.1$ to $\varphi_{\mathrm{f}} = 0.4$ at $J = 3$. The only non-zero component is $\langle m_{\mathrm{s}}^{\mathrm{x,cc}}\rangle$, which fluctuates as a function of time as can be seen more closely in the inset of the right panel. This is in fact the only motion technically in accordance with the equations of motion as discussed in Section 4.1.2. Evidently, the energy $\Delta\varepsilon$ introduced by the φ-quench is not sufficient to trigger any dynamics beyond this oscillation of electron spin length. The classical spins remain forever in their initial configuration. Similar results are found for other φ-quenches within the AF phase and for system sizes up to $L = 128$.

When instead of quenching φ, the coupling constant J is quenched within the AF phase, the situation is similar at first. Fig. 4.7 shows the staggered magnetization for both classical spins and electrons as a function of time after four different J-quenches (rows) within the antiferromagnetic phase again for a small system with $L = 8$ sites at $\varphi = 0$. The first two rows show quenches from $J_{\mathrm{ini}} = 4.0$ and $J_{\mathrm{ini}} = 5.5$ to $J_{\mathrm{f}} = 3$, respectively. Neither of these result in any dynamics other than that seen in Fig. 4.6. The only noticeable difference for the larger quench $J = 5.5 \rightarrow 3$ is the increasing amplitude of the electron oscillations. Looking back at Fig. 4.5, where the energy introduced by the quench $\Delta\varepsilon$ is plotted against φ_{ini} and J_{ini}, it is clear that in contrast to φ-quenches, J-quenches within the antiferromagnetic phase do cost energy - however small - and are thus expected to result in chaotic behavior. This is apparently only the case for $J_{\mathrm{ini}} \gtrsim 5.6$ for a system with $L = 8$ as can be seen in the bottom two rows in Fig. 4.7, where $J_{\mathrm{ini}} = 5.6$ and $J_{\mathrm{ini}} = 5.7$, respectively.
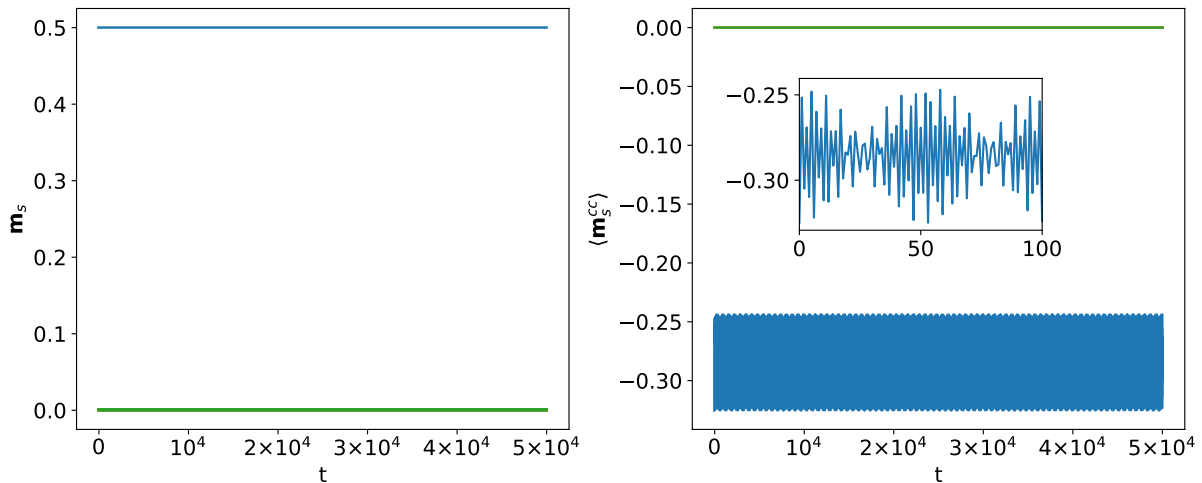
Figure 4.6.: Components of staggered magnetization per site $\mathbf{m}_s$ for classical spins (left) and electrons (right) after a quench from $\varphi = 0.1 \to 0.4$ for $J = 3$ and $L = 8$. Colors are the same for both panels. blue: x-component, orange: y-component (not visible, below the z-component), green: z-component. The inset shows a close-up of the oscillations in $\langle m_s^{x,cc} \rangle$ for the first 100 time steps.

There seems to be an energy threshold between $\Delta\varepsilon \approx 4.8 \cdot 10^{-2}$ and $\Delta\varepsilon \approx 5.1 \cdot 10^{-2}$ that needs to be overcome for chaotic dynamics to start. Even if both $J_{\text{ini}} = 5.6$ and $J_{\text{ini}} = 5.7$ in the bottom rows are clearly chaotic and likely ergodic, on comparatively long time scales of $t = 5 \cdot 10^4$ shown here, the mixing is still limited and the spins are evidently slow to rotate into other directions in space.

The assumption is generally, that any non-integrable system such as this one will be ergodic away from the ground state. The above observations of nearly stationary dynamics are thus in need of explanation. It could be argued that the quench energies shown are not very large, but the expectation is usually that even small energies should lead to ergodic behavior. Furthermore, energies of up to $\mathcal{O}(10^{-2})$ as shown are certainly not large, but also not negligible. In particular a J-quench from $J_{\text{ini}} = 5.5$ to $J_{\text{f}} = 3$ as pictured in the second row of Fig. 4.7 does not seem insignificant.

Another consideration could well be the finite system size. A system with $L = 8$ is admittedly not very large. Fig. 4.8, however, shows several J-quenches for a system with $L = 96$ lattice sites. Here, the energy threshold seems to be indeed much lower than in the system with $L = 8$, but it is still noticeable. The first row in Fig. 4.8 shows a J-quench from $J = 3.2 \to 3.0$ that results in stationary spins. This is of course a rather small quench with an energy of $\Delta\varepsilon \approx 4.8 \cdot 10^{-4}$, but while increasing the energy in the rows below does start dynamics, they can at most be described as *weakly chaotic*. Even after the largest quench from $J = 4.1 \to 3.0$ with $\Delta\varepsilon \approx 1.3 \cdot 10^{-2}$ the spins barely leave their initial alignment and merely start to oscillate erratically.

Before analyzing this in more detail, it seems necessary to introduce a more concrete measure of how

far the spin configuration is deviated from its initial configuration as a function of time. While the staggered magnetization gives a good qualitative and intuitive picture, it is difficult to quantify when the dynamics start and how chaotic they are. For this, a well-defined distance in phase space is needed. As the focus here is on the classical spins, the following discussion will be limited to a distance between spin configurations. The electrons, being coupled to the spins, are expected to align according to the classical spins in any case.

Figure 4.7.: Differently sized J-quenches within the antiferromagnetic phase with J_{ini} and $\Delta\varepsilon$ as indicated with $J_{\mathrm{f}} = 3$ at $\varphi = 0$ and $L = 8$. Plotted are the components of the staggered magnetization per lattice site for the classical spins $\mathbf{m}_s$ (left column) and for the electrons $\langle \mathbf{m}_s^{cc} \rangle$ (right column) for increasing energy $\Delta\varepsilon$ (top to bottom), where x=blue, y=orange and z=green.
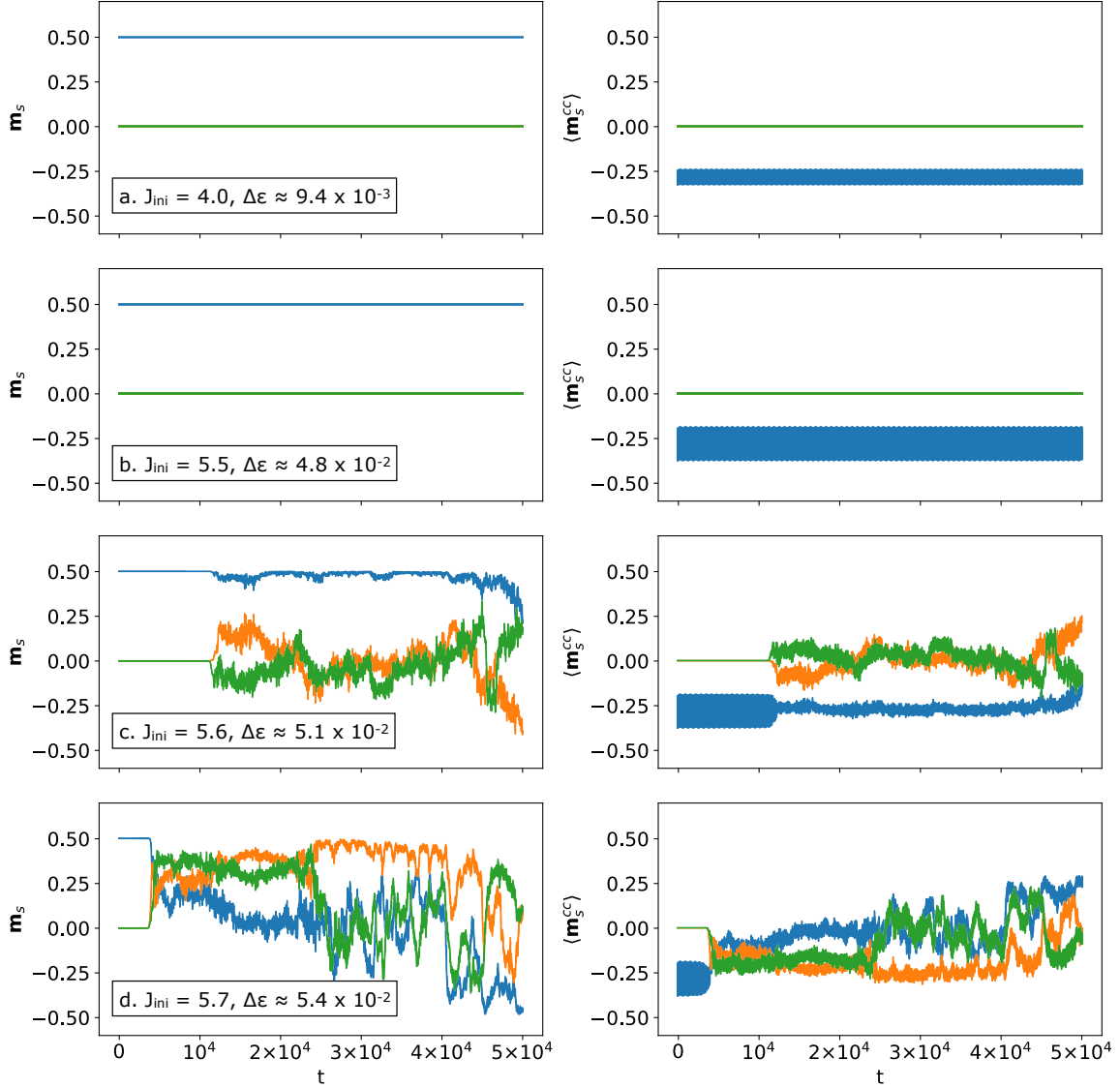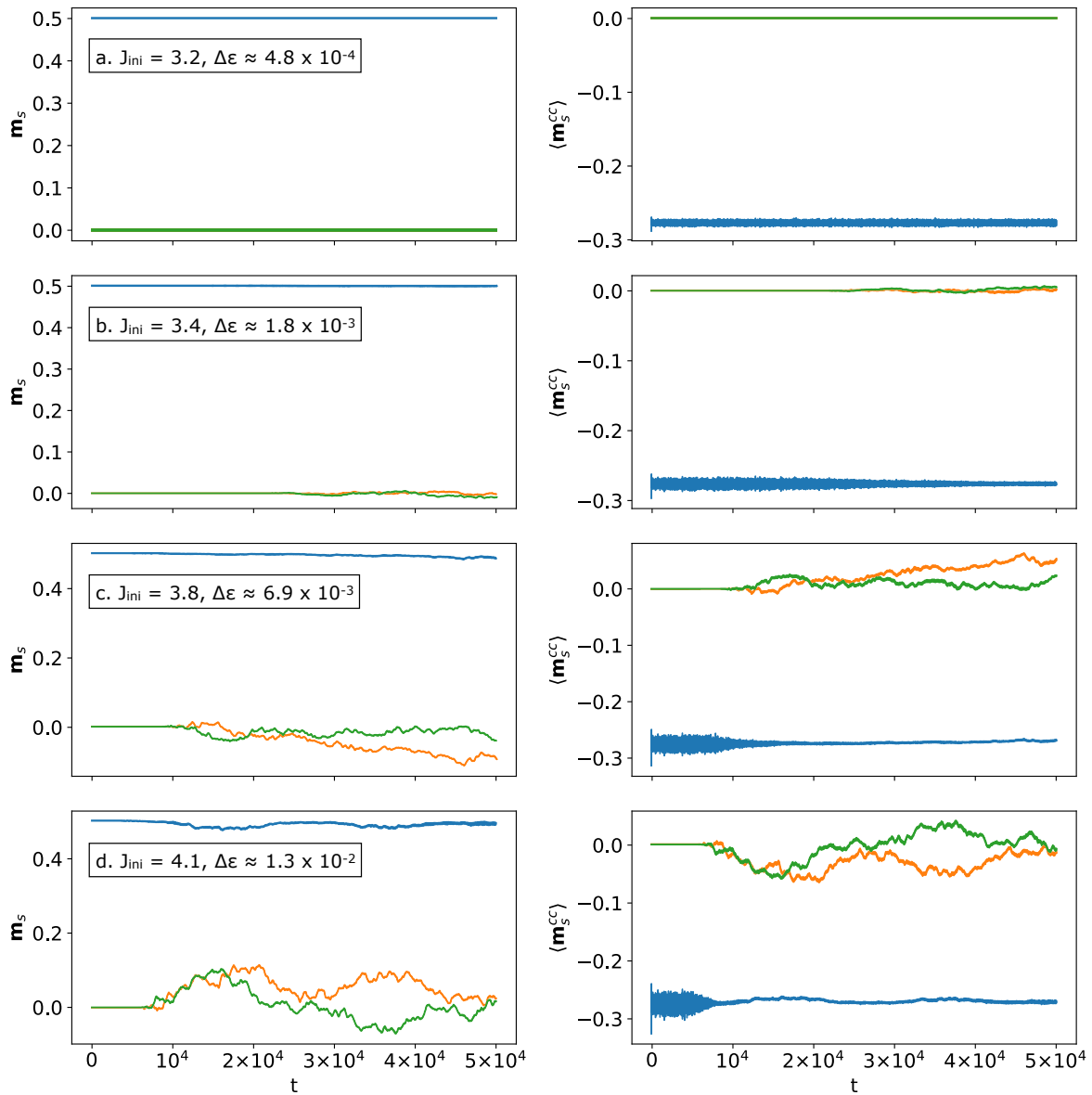
Figure 4.8.: Differently sized J-quenches within the antiferromagnetic phase with J_{ini} and $\Delta\varepsilon$ as indicated with $J_{\text{f}} = 3$ at $\varphi = 0$ and $L = 96$. Plotted are the components of the staggered magnetization per lattice site for the classical spins $\mathbf{m}_{\text{s}}$ (left column) and for the electrons $\langle \mathbf{m}_{\text{s}}^{\text{cc}} \rangle$ (right column) for increasing energy (top to bottom), where x=blue, y=orange and z=green.

Consider a spin configuration

$$\mathcal{C}_S \equiv \{\mathbf{S}_i\} \quad \text{with} \quad \mathbf{S}_i \in \mathbb{R}^3 \quad \text{and} \quad |\mathbf{S}_i| \equiv S = 1/2 \quad \text{for} \quad i = 1, \ldots, L \tag{4.27}$$

where each spin individually follows a trajectory $\mathbf{S}_i(t)$ in phase space. As the length of the classical

spins is fixed, each spin can only take values that lie on a sphere with radius S. The shortest distance between two points on a sphere is a geodesic on the surface of the sphere, also called great-circle distance. The parametrization can be chosen conveniently, such that the distance between two spins $\mathbf{S}_1$ and $\mathbf{S}_2$ in $\mathbb{R}^3$ is proportional to the angle between them as illustrated in Fig. 4.9. The shortest distance between two spin configurations $\mathcal{C}_S^A, \mathcal{C}_S^B$ is then given by

$$d(A, B) = \sqrt{\sum_{i=1}^{L} S^2 \phi_i^2} \quad \text{with} \quad \phi_i = \arccos\left(\frac{\mathbf{S}_i^A \cdot \mathbf{S}_i^B}{S^2}\right) \leq \pi \tag{4.28}$$

where $\mathbf{S}_i^A \in \mathcal{C}_S^A$ and $\mathbf{S}_i^B \in \mathcal{C}_S^B$. Eq. (4.28) implies, that the furthest distance is $d = S\pi\sqrt{L}$, where each spin is flipped in an opposite direction. This notation was inspired by [70].
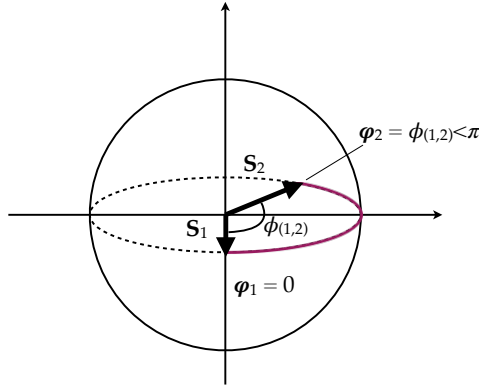
Figure 4.9.: Shortest distance between two classical spins $\mathbf{S}_1$ and $\mathbf{S}_2$, i.e. great-circle distance on a sphere.

Armed with a measure of how 'far away' the system is from the equilibrium configuration, it can now be analyzed precisely when the dynamic starts as a function of the energy introduced by the quench. Let

$$d_S(t) \equiv d(\mathcal{C}_0, \mathcal{C}_t), \tag{4.29}$$

where $\mathcal{C}_0$ denotes the initial spin configuration and $\mathcal{C}_t$ the spin configuration at time t. This distance from the initial state allows to determine the starting point of the dynamics with a single parameter, i.e. $d_S(t) > 0$. This is useful to determine the critical energy below which the spins are absolutely stationary. In order to capture also how closely the spins stay aligned, another measure is the length of the staggered magnetization per site

$$m_{\mathrm{s}} \equiv \sqrt{m_{\mathrm{s},x}^2 + m_{\mathrm{s},y}^2 + m_{\mathrm{s},z}^2} \,, \tag{4.30}$$

that is for a truly ergodic system expected to decrease and eventually become zero, as the system has no preferred direction in space and no long range magnetic order is allowed for a one dimensional system such as the one present here. The absence of long range order in one and two dimensional systems was proved rigorously by N. David Mermin und Herbert Wagner in 1966 [55] and is accordingly called the *Mermin-Wagner-theorem*, more on this will be mentioned later. If ergodicity is defined as time average = ensemble average (Eq. (4.20)), then a system with long time average $\langle m_{\mathrm{s}} \rangle \neq 0$ cannot be considered ergodic.

In Fig. 4.10, $d_S(t)$ as well as $m_{\mathrm{s}}(t)$ are plotted as a function of time for differently sized J-quenches with energies between $\Delta \varepsilon \approx 1.2 \times 10^{-4}$ (light green) and $\Delta \varepsilon \approx 1.7 \times 10^{-2}$ (dark blue) for a system with $L = 96$ sites. For lower energies (green lines), the distance d_S is either zero or, at marginally larger energies, increases very slightly. Over the entire time span of $t = 5 \times 10^4$ it grows very slowly if at all. Increasing the energy further, the spin configuration evidently leaves the initial condition, but, at least on the pictured time scales, seems to relax to a finite value still moderately close to zero. The largest energy (darkest blue) is the only one that can be said for certain to exhibit a clear upward trend. After a short initiation time it starts to increase continuously. Note that the maximum distance for $L = 96$ is according to the above definition $d_{S,\mathrm{max}} \approx 15.4$, which indicates that even $d_S \approx 3$ as in the case of the largest quench is not very far from the initial configuration, especially after a comparatively long time span of $t = 5 \times 10^4$ time steps.
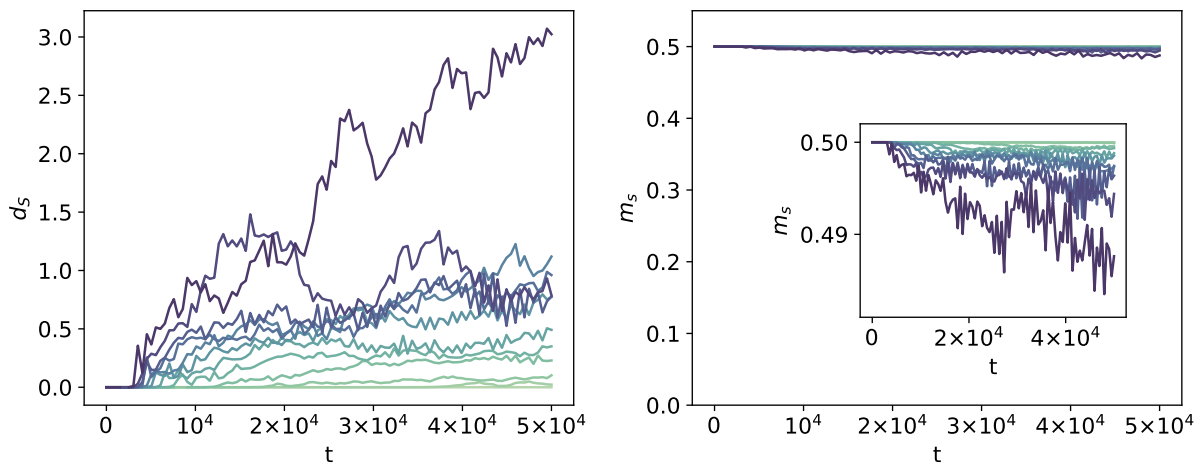
Figure 4.10.: Left: distance from initial spin configuration d_S as defined in Eqs. (4.28) and (4.29) as a function of time for quenches of different energies between $\Delta \varepsilon \approx 1.2 \times 10^{-4}$ (light green) and $\Delta \varepsilon \approx 1.7 \times 10^{-2}$ (dark blue) for a system with $L = 96$ sites at $\varphi = 0$ and $J_{\mathrm{f}} = 3$. Right: length of staggered magnetization per site m_s. Inset: Zoom into $m_s(t)$.

The length of the staggered magnetization plotted in the right panel of Fig. 4.10 can be considered as approximately conserved for all quenches. Even the largest quench only results in a decrease of approximately 3 % after $t = 5 \times 10^4$ time steps, and is the only one that displays a clear downward trend. All other energies follow the qualitative behavior of the distance plotted in the left panel of Fig. 4.10, i.e. even if they do depart from the initial value of $m_s = 0.5$, they seem to settle into a value only slightly below. The long range order present at zero temperature therefore remains even after a parameter quench introduces energy into the system. Without explicitly calculating the long time average $\langle m_s \rangle$, it is clear that it will not go to zero within the time scales accessible with this method.
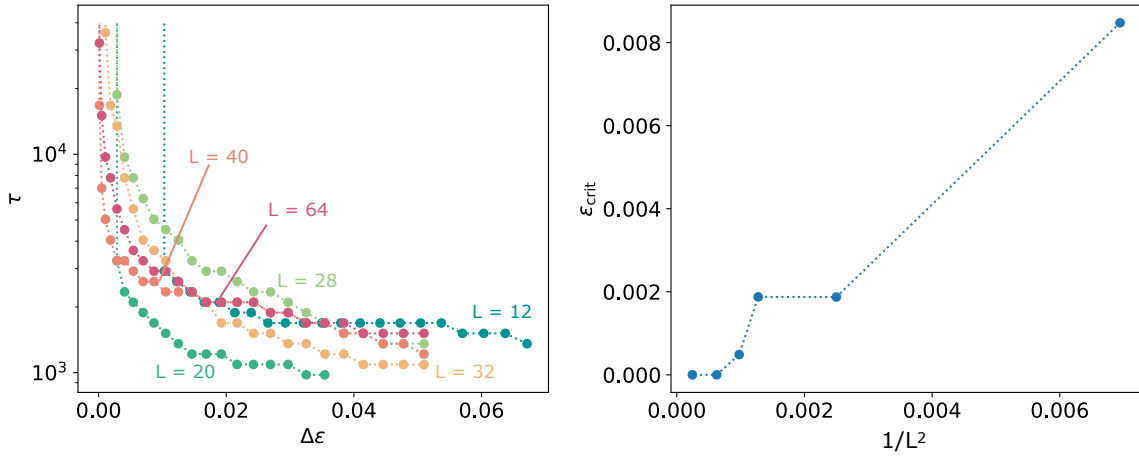

Figure 4.11.: Left Panel: Lifetime τ of initial spin configuration (or, equivalently, m_s) as defined in Eq. (4.31) plotted against energy per lattice site $\Delta\varepsilon$ for $J_f = 3$, $\varphi = 0$ and different lattice sizes as indicated, each vertical dotted line indicates $\tau = \infty$. Right panel: critical energy per lattice size $\varepsilon_{\text{crit}}$ as a function of $1/L^2$.

Another definition is needed to allow for a systematic analysis of the dependence on system size L. Evidently, there is a finite energy that needs to be overcome to take the system away from the initial state at all, and even if it does depart, it stays rather close to the initial configuration even after long times. To further quantify this, it is useful to define a "lifetime" τ of the initial spin configuration as

$$\tau \equiv \min t \quad \text{with} \quad d_S(t) > 0, \tag{4.31}$$

which is the time until the dynamic starts at all. In the following results this is numerically implemented as $d_S(t) > 10^{-5}$, although several values were tested and the results do not depend on the exact choice, as long as it is numerically small, i.e. of order $\mathcal{O}(10^{-4})$ or below. Naturally, τ must depend on the energy introduced by the quench $\Delta\varepsilon$. This relationship is plotted for several lattice sizes for $J_f = 3$, $\varphi = 0$ in the left panel of Fig. 4.11. τ increases strongly with $\Delta\varepsilon$ and eventually diverges for all lattice

sizes. The last data point is in all cases $\tau = \infty$, indicated by the vertical dotted lines. This point can be seen as the location of the critical energy $\varepsilon_{\text{crit}} = E_{\text{crit}}/L$, below which m_{s} is conserved exactly and the system does not show any dynamics.

Note that despite plotting against $\Delta\varepsilon = \Delta E/L$, there is still a distinct L-dependence of $\tau(\Delta\varepsilon)$, in particular of $\varepsilon_{\text{crit}}$. The latter is plotted in the right panel of Fig. 4.11. Evidently $\varepsilon_{\text{crit}} \to 0$ in the thermodynamic limit $L \to \infty$ approximately $\propto 1/L^2$.

4.2.2. The FPU Problem and Proximity to Integrability

This energy threshold is reminiscent of a phenomenon known in the framework of classical dynamics. In 1954, Enrico Fermi, John R. Pasta, Stanislaw Ulam und Mary Tsingou carried out one of the earliest numerical computer simulations now known as the Fermi-Pasta-Ulam-Tsingou or often just Fermi-Pasta-Ulam (FPU) problem [71]. The original objective was to confirm the ergodicity hypothesis by showing that any nonlinearity added to a linear model will immediately result in chaotic and thereby ergodic behaviour. They found, however, a different result, regardless of whether the chosen perturbation type was quadratic (termed α-model), cubic (termed β-model), or "broken linear". In each of their calculations, for $N = 32$ and $N = 64$ modes, the behavior was not chaotic at all, but found to be quasi-periodic. This result triggered many new avenues of research and lead for example to the discovery of solitons [72] and the integrability of a complete class of nonlinear equations, including the Korteweg-de Vries equations [73,74].

The idea that a system "close to" an integrable model retains its regular, non-chaotic dynamics was first proposed by Andrey Kolmogorov in 1954 [75] and later proven rigorously (under certain conditions) by Jürgen Moser in 1962 [76] and Vladimir Arnold in 1963 [77] and is since known as the *KAM-theorem*. The premise of it is that small perturbations to an integrable model leave some of the invariant tori introduced at the beginning of this section and sketched in Fig. 4.4, intact, such that depending on the initial conditions, the motion could still be trapped on one of them. Even though some of the conditions for its applicability - for example a nonlinear integrable model, smaller systems, smaller perturbations - are not satisfied in case of the FPU problem, it is still often cited as a qualitative explanation of the periodic dynamics of the nonlinear FPU model.

Inspired by the idea of the KAM-theorem, Felix Izrailev and Boris Chirikov found an energy threshold for the β-model above which the dynamics start to exhibit the expected ergodic behavior, that is calculated using a theory of overlapping non-linear resonances, which they called *stochasticity threshold* [78]. As it turns out, the initial conditions Fermi et. al. used in their original simulation were located far below this energy threshold. In particular the size of the perturbation was found to be much too small, despite previous perturbation theory studies finding the original FPU problem to be "beyond weak coupling limit" [79,80].

Neither the FPU threshold nor the KAM theorem can be applied exactly to the problem at hand, but inspired by this, the reason for the critical energy in the dynamics found here will be further investigated. Particularly promising seems the search for a "nearby" integrable model. The Kondo lattice model is very likely not integrable neither in the full quantum-mechanical version nor with classical spins, but a related spin model, the *Heisenberg model* was solved exactly by Hans Bethe in 1931 in the quantum mechanical variant, at least in the nearest-neighbor only case [81]. The classical spin-Heisenberg model has under certain conditions also been found to be integrable in the limit of small lattice sizes (see e.g. [82]). Since the FPU paradox is a classical mechanics problem and the relevant degrees of freedom here are the classical spins, it is not entirely far fetched to hope for an effective spin-only model that perhaps even posses an integrable limit. The following section will be concerned with the integrability of classical Heisenberg models in the geometry present here, i.e. the zigzag chain. Although this is ultimately not found to be a reasonable explanation for the numerically found energy threshold - this will be given later in Section 4.2.4 - it is still instructive to consider.

4.2.3. Integrability of the Classical J_1-J_2- Heisenberg Model

One of the most fundamental models of magnetism is the Heisenberg model that describes interactions between localized spins $\mathbf{S}_i$, $\mathbf{S}_j$ coupled to each other with coupling constants J_{ij}. The Hamiltonian is given by

$$H = \sum_{ij} J_{ij} \mathbf{S}_i \mathbf{S}_j \, , \tag{4.32}$$

where usually, the coefficients J_{ij} are taken to be nonzero only for nearest neighbours i, j, but here on the zigzag geometry, in addition to $J_{ij} = J_1$ for i, j=nearest neighbours (n.n.), $J_{ij} = J_2$ for next-to-nearest neighbours(n.n.n.), i.e.

$$H = J_1 \sum_{ij}^{\text{n.n.}} \mathbf{S}_i \mathbf{S}_j + J_2 \sum_{ij}^{\text{n.n.n.}} \mathbf{S}_i \mathbf{S}_j \, . \tag{4.33}$$

This is sometimes also called the *(Heisenberg) J_1-J_2—model*. An equilibrium consideration on this model can be found in Appendix A.

Nearest-neighbour-classical spin systems are thought to be non-integrable in general, except for the trivial highly anisotropic Ising case [83]. Technically, the $J_1 - J_2$-model is not a nearest-neighbor model, and in any case, exceptions may certainly exist. There is no known universal statement on the integrability of the classical $J_1 - J_2$-model, and it seems unlikely that it should be integrable in general. Still, there may be an integrable limit.

R. Steinigeweg et. al. propose a method to derive the integrability of small spin clusters of "Heisenberg type", i.e. that can be described with a Hamiltonian of the general form seen in Eq. (4.32) [82]. There, it is proven that such a spin system is integrable if it is either the *uniform* or *disjoint union* of other, themselves integrable, spin systems. In this context, a *uniform union* is defined as the union of two spin

systems A and B, where every spin in system A is coupled to every spin from system B with nonzero coupling constant J. A *disjoint union*, likewise, is then defined similarly, only with zero coupling constant $J = 0$. Using this method and a table of known integrable spin clusters in [82], the Heisenberg $J_1 - J_2$ model is found to be integrable only in the cases $L = 4$ and $L = 6$ with $J_1 = J_2 = 1$. The generalization to arbitrary values of $J_1 = J_2 \neq 1$ is assumed to be possible and numerically confirmed.
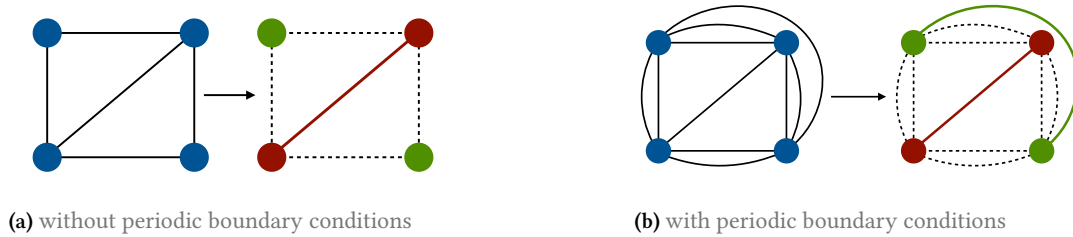

(a) without periodic boundary conditions   **(b)** with periodic boundary conditions

Figure 4.12.: Heisenberg J_1-J_2-spin cluster with $L = 4$ (a) without and (b) with periodic boundary conditions, where both right pictures shows the separation into two integrable subsystems shown as red and green.

The smallest possible system that could still be considered a "zigzag ladder" contains four lattice sites as pictured in Fig. 4.12. Both a spin dimer (two coupled or decoupled spins) and a single spin are known to be integrable. As the four spin model as pictured in Fig. 4.12 can be separated into the disjoint union of two such dimers, it is therefore also integrable both with and without periodic boundary conditions. The respective separation into subsystems is pictured in Fig. 4.12a and Fig. 4.12b.

Four spins is of course barely a ladder, the question is now whether the integrability holds also for larger sytems. The next larger system is a zigzag ladder with six sites as pictured in Fig. 4.13. Here, periodic boundary conditions are necessary to allow for separation into integrable subsystems. Fig. 4.13 shows that with periodic boundary conditions, the six spin system can be separated into a uniform union of two integrable subsystems, the four spin model marked in red and a disconnected dimer marked in green. The spins are labeled from $i = 0$ to $i = 5$ to facilitate the following analysis of constants of motion.

A system is integrable if it has as many linearly independent constants of motion c_i (that are also in involution, i.e. $\{c_i, c_j\} = 0$) as degrees of freedom $i = 1, ..., L$, the six-spin model pictured in Fig. 4.13 with $L = 6$ should therefore contain six conserved quantities. All spin systems of Heisenberg type (Eq. (4.32)) have at least two constants of motion, the total energy E_{tot} and one component of the total spin, often taken to be S_{tot}^z. If a system can be separated into two integrable subsystems A and B, i.e. $H = H_A + H_B$, there is an additionally known constant of motion, namely $\mathbf{S}_{\text{tot}}^2 - \mathbf{S}_A^2 - \mathbf{S}_B^2$. Furthermore, the total system also respects the conserved quantities of the respective subsystems [82].
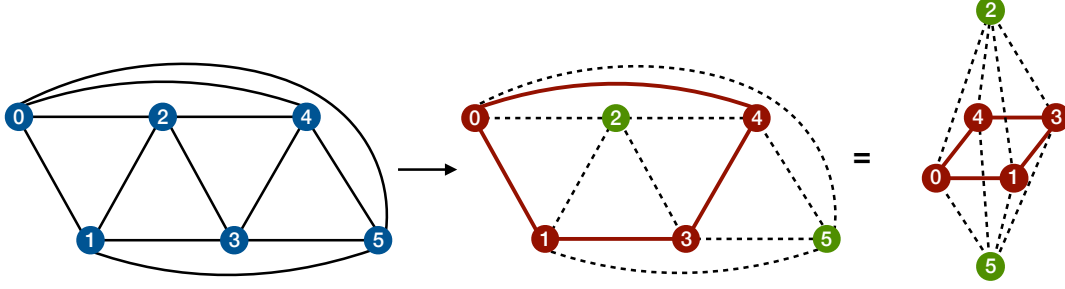
Figure 4.13.: Decomposition into two integrable subsystems shown in red and green of the J_1-J_2 system with $L = 6$, $J_1 = J_2$ and periodic boundary conditions.

Note that the choice for the conserved quantities is not unique. Gathering all the above mentioned hints, the six constants of motion for a classical Heisenberg spin system on the zigzag ladder with six spins can be expressed as

$$
\begin{aligned}
&1)\, E_0 = E_{\text{tot}},\\
&2)\, S^z_{\text{tot}},\\
&3)\, E_1 = \mathbf{S}_0\mathbf{S}_3,\\
&4)\, E_2 = \mathbf{S}_1\mathbf{S}_4,\\
&5)\, E_3 = \mathbf{S}_2\mathbf{S}_5,\\
&6)\, E_4 = \mathbf{S}^2_{\text{tot}} - \mathbf{S}^2_A - \mathbf{S}^2_B = \mathbf{S}_0\mathbf{S}_2 + \mathbf{S}_0\mathbf{S}_5 + \mathbf{S}_1\mathbf{S}_2 + \mathbf{S}_1\mathbf{S}_5 + \mathbf{S}_2\mathbf{S}_3 + \mathbf{S}_2\mathbf{S}_4 + \mathbf{S}_3\mathbf{S}_5 + \mathbf{S}_4\mathbf{S}_5\,.
\end{aligned}
\tag{4.34}
$$

As the *uniform* or *disjoint union* introduced above is only defined for the case $J_1 = J_2 = J \in \{0,1\}$, the separation shown in Fig. 4.13 would cease to be "uniform" in case of unequal couplings $J_1 \neq J_2$. As integrable systems are rather rare in general, a system that is not (yet) proven to be integrable is usually expected not to be. Whether the integrability of the six spin Heisenberg zigzag ladder and thus the conservation of the constants of motions Eq. (4.34) holds away from $J_1 = J_2$ is tested numerically in Fig. 4.14. Instead of J_1 and J_2, the variable to measure frustration will be taken as φ to allow a better comparison to the Kondo lattice model thereafter. As shown in Section 2.3.2, in equilibrium the Kondo lattice can be mapped exactly onto an effective Heisenberg model with

$$
J_1 = \frac{8t_1^2}{J} \quad \text{and} \quad J_2 = \frac{8t_2^2}{J}\,,
\tag{4.35}
$$

where $t_1 = t\cos\varphi$, $t_2 = t\sin\varphi$ and J is given in units of inverse hopping t as in the rest of this thesis. This parameterization will be used for $\varphi = \arctan(t_2/t_1) = \arctan(\sqrt{J_2/J_1})$. Note that of course $\varphi = \pi/4$ implies both $J_1 = J_2$ and $t_1 = t_2$. Fig. 4.14 now shows dynamics in the Heisenberg and

Kondo lattice model for different values of φ.

The initial conditions used are the same in all columns, namely the spiral ground state at $\varphi = \pi/4$ slightly perturbed to initiate dynamics. Note that this refers to the alignment of the classical spins, the initial condition for the electrons is as in all dynamical calculations within this thesis simply the corresponding ground state as explained in Section 4.1. The perturbation is exactly the same in all columns to guarantee exactly similar initial conditions. All calculations are done for $J = 10$. To clarify, J denotes the Kondo coupling, whereas J_1 and J_2 are the Heisenberg coupling constants, which depend on J as given in Eq. (4.35). The first row shows the dynamics of the average angle between nearest neighbor spins $\langle \theta_i \rangle$. In the integrable case $\varphi = \pi/4$ shown in orange in the middle column, the oscillation of $\langle \theta_i \rangle$ does look rather regular, it appears to be a superposition of periodic motions with different frequencies. Going away from the integrable case in the columns immediately to the left and right, this quality persists. Only looking at the dynamics in the first row, it would not be surprising to find that the system with $\varphi \neq \pi/4$ is still integrable. This is disproven, however, by looking at the rows below, where the constants of motion in Eq. (4.34) are also plotted as a function of time (except for E_{tot} and S_{tot}^z that are trivially conserved in all cases). Evidently, they are only constant in the previously found to be integrable case of $\varphi = \pi/4$.

This behaviour is reminiscent of the above mentioned KAM-theorem [75–77]. In short, the theorem states that even away from integrability, a system can retain invariant tori in phase space on which the motion remains regular. Under certain conditions, the measure of the chaotic regions is in fact nearly zero. Evidently, non-chaotic motion alone is no proof of integrability, and is indeed to be expected in the vicinity of a known to be integrable model. This idea explains the regular dynamics close to but away from the integrable case $J_1 = J_2$ in Fig. 4.14.

The rightmost column in Fig. 4.14 shows the same quantities in the Kondo lattice model plotted in red at $\varphi = \pi/4$, again using the same initial conditions as in the $J_1 - J_2$-model cases. The dynamics in the first row do not look regular at all, and none of the constants of motion of the Heisenberg spin case are still conserved. Unlike the Heisenberg model, the Kondo lattice does not appear to be integrable at $L = 6$, even though in equilibrium at $J = 10$ the ground state of the Kondo lattice is almost exactly that of an effective Heisenberg model with $J_1 = 8t_1^2/J$ and $J_2 = 8t_2^2/J$. The perturbative description seems to be limited to the equilibrium case and cannot be extended beyond.

This result is of course not altogether surprising, the mere fact that in equilibrium the Kondo lattice model can be mapped onto an effective Heisenberg model in the strong coupling limit does not necessarily imply that the dynamics are similar at all. In fact, it is not even trivial to simply compare the two models in non-equilibrium.
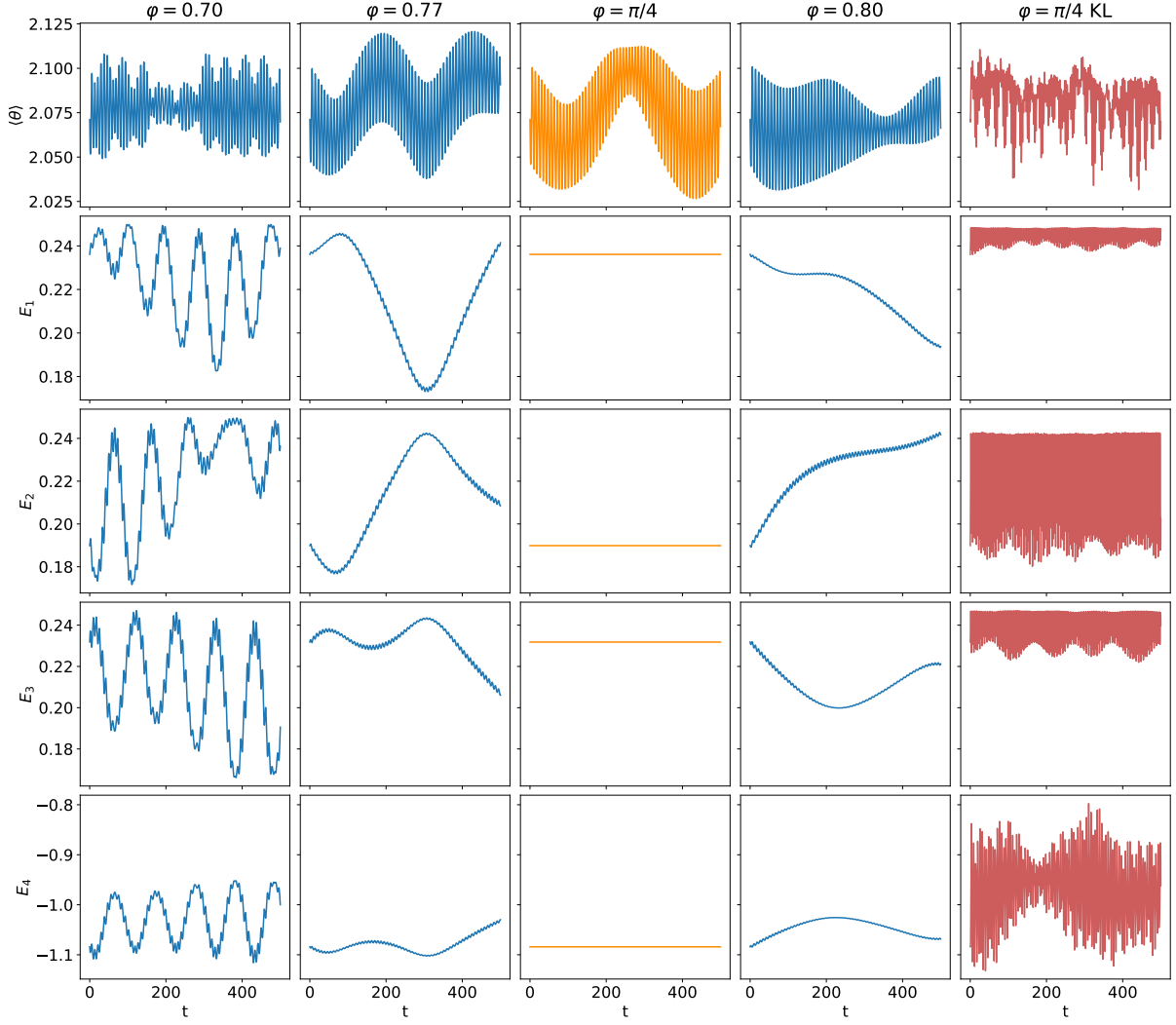
Figure 4.14.: First row: average nearest-neighbor angle $\langle \theta_i \rangle$ as a function of time for different values of φ, where the integrable case is plotted in orange ($\varphi = \pi/4$). Other rows: constants of motion of the integrable case, see Eq. (4.34). Rightmost column: comparison to Kondo lattice model. All calculations are done for $J = 10$ with $J_1 = 8t_1^2/J$, $J_2 = 8t_2^2/J$ and $\varphi = \arctan(t_2/t_1)$.

As introduced in Section 4.1.1, the equations of motion for classical spins and electrons in the Kondo lattice model are

$$
\begin{aligned}
\frac{\mathrm{d}}{\mathrm{d}t}\mathbf{S}_i(t) &= J\langle \mathbf{s}_i \rangle_t \times \mathbf{S}_i(t) \quad \text{and} \\
\frac{\mathrm{d}}{\mathrm{d}t}\langle \mathbf{s}_i \rangle_t &= J\mathbf{S}_i(t) \times \langle \mathbf{s}_i \rangle_t - \frac{i}{2}\sum_j t_{ij}\left(\langle c_{i\sigma}^{\dagger}\boldsymbol{\sigma}_{\sigma\sigma'}c_{j\sigma'}\rangle_t + h.c.\right),
\end{aligned}
\tag{4.36}
$$

compared to only the classical spins in the Heisenberg J_1-J_2-model with

$$\frac{\mathrm{d}}{\mathrm{d}t}\mathbf{S}_i = \sum_{j}^{\text{n.n.}} J_1\,\mathbf{S}_j \times \mathbf{S}_i + \sum_{j}^{\text{n.n.n.}} J_2\,\mathbf{S}_j \times \mathbf{S}_i\,, \tag{4.37}$$

where $\sum^{\text{n.n.}}$ and $\sum^{\text{n.n.n.}}$ denote the sums over nearest and next-to-nearest neighbours, respectively, and again $J_1 = 8t_1^2/J$ and $J_2 = 8t_2^2/J$.
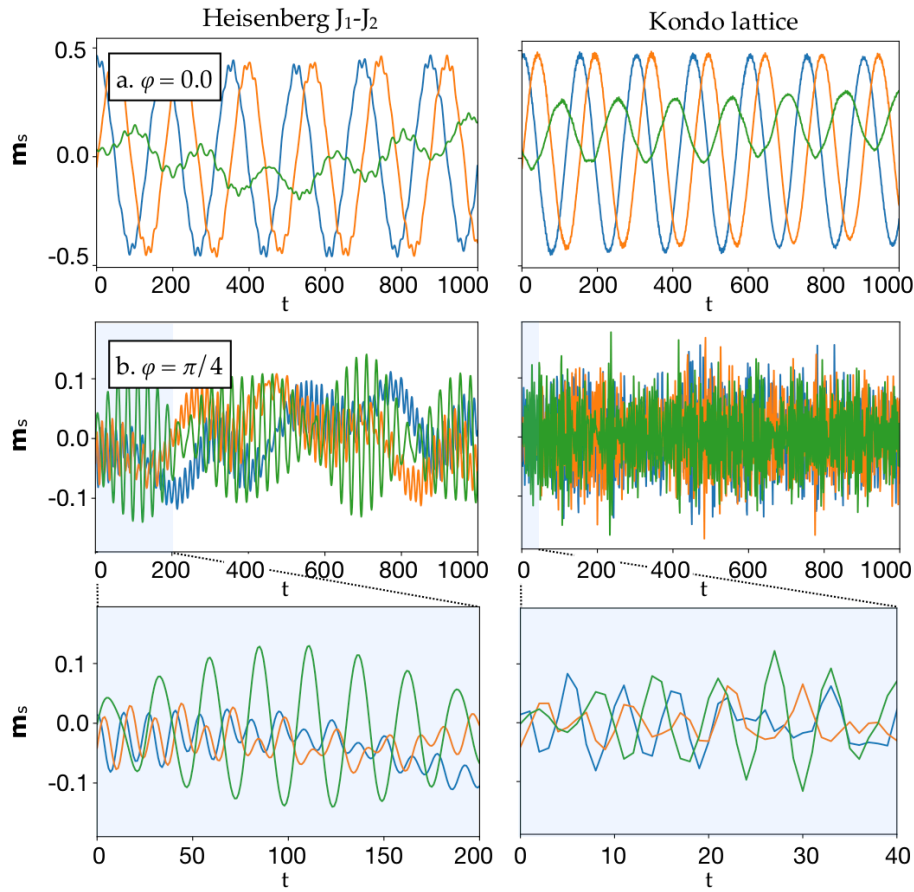
Figure 4.15.: Comparison between Dynamics in the Heisenberg J_1-J_2-model (left column) and the Kondo lattice (right column) for a. $\varphi = 0.0$ (top row) and b. $\varphi = \pi/4$ (middle and bottom row). Plotted are the components of the staggered magnetization per site m_s^x (blue), m_s^y (orange) and m_s^z (green). The bottom row shows a zoom of the middle row at different time scales for Heisenberg and Kondo model. All frames are calculations at $L = 6$ and $J = 15$ with identical initial conditions between left and right column.

In the Kondo lattice model, the only energy scale is given by the amplitude of the hopping t, time steps

are therefore given in units of inverse hoppings $1/t$. With $t_1 = t \cos \varphi$ and $t_2 = t \sin \varphi$, the dynamics in the Heisenberg model in Eq. (4.37) are effectively $\propto t^2/J$. A true comparison between dynamics in the two models is therefore impossible without adjusting the time scales. Numerical results show that the dynamics are indeed similar only if the time scale is adjusted. The exact adjustment-factor, however, is found to be non-trivial and not only to depend on J, but also to depend on φ.

Fig. 4.15 shows a comparison between dynamics in the J_1-J_2-Heisenberg model (left column) and the Kondo lattice (right column) for a system of size $L = 6$ with $J = 15$. The setting is again a slightly perturbed initial spin configuration, different for cases a. $\varphi = 0$ and b. $\varphi = \pi/4$ but same for the respective left and right panel comparing Heisenberg and Kondo model. In the first row, the dynamics is initiated by slightly perturbing the initial antiferromagnetic ground state. The components of the staggered magnetization per lattice site, defined as in Eq. (4.25), are plotted with blue lines showing m_s^x, orange lines m_s^y and green lines m_s^z. All are oscillating in the same way and with roughly the same frequency for both the Heisenberg and the Kondo model, without adjusting the time scale. In the second row, the perturbed initial configuration is the spin spiral ground state at $\varphi = \pi/4$. Here, the oscillation only look similar when comparing at different time scales as illustrated by the third row, that shows a zoom into time sections of the middle row, that are different in the Heisenberg and Kondo case. The Kondo lattice dynamics are apparently faster by roughly a factor of 5, but even after adjusting for time scales the similarities between Heisenberg and Kondo model are approximate at best. Note that even though the dynamics in the top row look rather regular, neither the Heisenberg nor the Kondo lattice are integrable in this parameter regime as mentioned above. This is only the case for the Heisenberg model at $L = 6$ and $\varphi = \pi/4$, i.e. the left panel of the middle and bottom row of Fig. 4.15.

The behavior after a parameter quench, as opposed to simply a slight perturbation, is in both models also only qualitatively similar. This is pictured in Fig. 4.16. Again, the left column shows the dynamics of the $J_1 - J_2$-Heisenberg model and the right column that of the Kondo lattice. Here, the initial configuration is the antiferromagnetic ground state at $\varphi_{\text{ini}} = 0.3$ in a system of size $L = 100$ with $J = 30 = \text{const.}$. Plotted are the dynamics of the components of the staggered magnetization per site m_s^x (blue), m_s^y (orange), and m_s^z (green), after a quench to $\varphi_{\text{f}} = 0.7$. The bottom row shows a zoom into different time sections of the Heisenberg and Kondo dynamics. Again, the Kondo lattice dynamics are faster than in the Heisenberg model, but in this case by a factor of roughly 10.

Comparing Fig. 4.16 to case b. of Fig. 4.15 (middle and bottom rows), it could be concluded that the Kondo lattice dynamics are generally faster by a factor of $J/3$. The first row of Fig. 4.15, however, shows that at $\varphi = 0$, both models are moving roughly at the same time scale. More calculations at different values of φ, that are for reasons of brevity not pictured here, confirm a nontrivial dependence on φ of the time scale of the dynamics. The influence of φ is not altogether surprising, seeing as it is defined as $\varphi = \arctan(t_2/t_1)$ in terms of the hopping amplitudes in the electron system of the Kondo lattice model, that has no equivalent in the Heisenberg model. The coupling constants resulting

from perturbation theory are $\propto t_1^2, t_2^2$, thus φ is not a very well defined measure of frustration in the Heisenberg model.
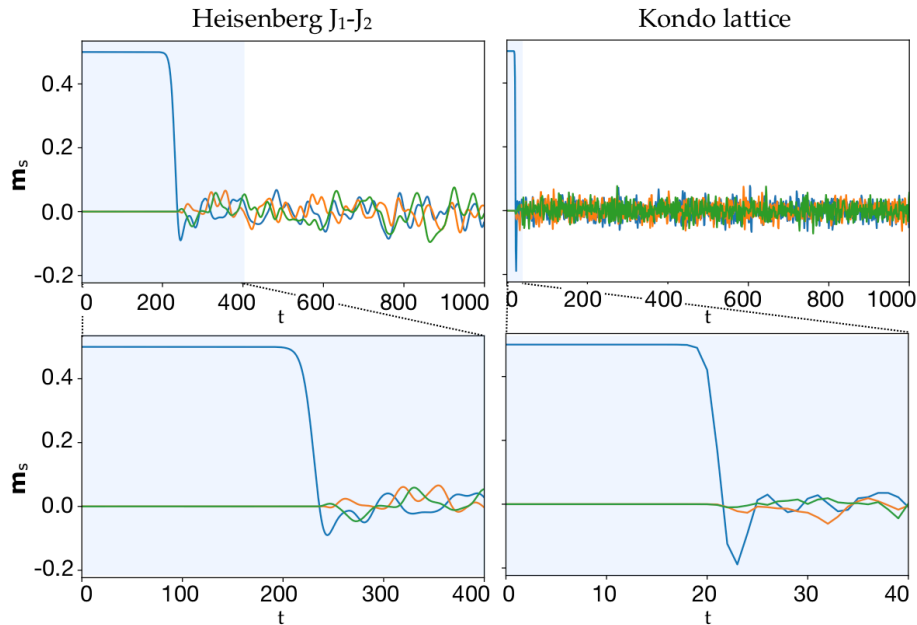

Figure 4.16.: Dynamics after a quench $\varphi = 0.3 \rightarrow 0.7$ in the J_1-J_2-Heisenberg model (left column) and the Kondo lattice (right column) for $L = 100$ and $J = 30$. Plotted are the components of the staggered magnetization per size m_s^x (blue), m_s^y (orange) and m_s^z (green). The bottom row shows a zoom of the top row at different time scales in the Heisenberg and Kondo model.

To conclude this section, neither the Heisenberg nor the Kondo lattice model on the zigzag ladder are integrable in general. The Heisenberg model with $L = 6$ sites and periodic boundary conditions, however, is integrable if $J_1 = J_2$. Although in equilibrium, the Kondo lattice on the zigzag ladder can be mapped onto the Heisenberg model in the strong coupling limit, a comparison between the two models cannot be generalized to non-equilibrium.

4.2.4. Linear Approximation and Spin-Wave-Like Excitations

In the problems from classical dynamics mentioned in Section 4.2.2, the ergodicity threshold was explained with a proximity to an integrable model. If this is the case here, then the Heisenberg $J_1 - J_2$-model was excluded as a possible candidate for such an integrable limit in the last section. In the FPU paradox introduced above, a non-linear perturbation is added to a linear model in order to observe ergodic behavior. Here, the starting point is the full system, but the backwards route is also possible - by linearizing the equations of motion. This is incidentally also done in classical spin wave theory

to describe low energy collective excitations of the Heisenberg model that are also known to destroy long range magnetic order in low dimensional systems. As shown in Chapter 3, the system considered here displays a magnetic long range order at $T = 0$. It seems therefore a worthwhile approach to look for corresponding spin-wave-like excitations, as spin-wave theory is a *linear* theory and thus derives from an integrable model, valid at very low excitation energies.

Before applying the linear approximation to the Kondo lattice, a short review of classical spin wave theory as known in the literature is presented. Again, the starting point will be the Heisenberg model, the paradigm model for localized magnetism. At zero temperature it describes a perfectly ordered ferromagnet or antiferromagnet, depending on the sign of the interactions. At finite temperature, this order is either decreased or, if the model is one or two dimensional, entirely destroyed as proven in the so-called *Mermin-Wagner-theorem* [55]. The order is destroyed by propagating spin waves with a gapless excitation spectrum, in the quantized version also called *magnons*. Their dispersion relation can be obtained in several ways, one of those being a linearization of the equations of motion. The equations of motion of the Heisenberg model

$$H = \sum_{i,j=1}^{N} J_{ij} \, \mathbf{S}_i \cdot \mathbf{S}_j \tag{4.38}$$

can be derived as in Section 4.1.1 using Eq. (4.2) and are given by

$$\frac{\mathrm{d}}{\mathrm{d}t} \mathbf{S}_i = \sum_{j=1}^{N} J_{ij} \, \mathbf{S}_j \times \mathbf{S}_i \,. \tag{4.39}$$

As this is the case of relevance here, the coupling constants considered will be $J_{ij} > 0$, for which the ground state is antiferromagnetic.

The premise of spin wave theory is a perturbation $\delta \mathbf{S}_i$ precessing around the ground state spin configuration $\{\mathbf{S}_0\}$, which is perfectly aligned along an arbitrarily chosen axis in space. Note that this type of excitation - an expansion around the initial configuration - agrees with the kind of dynamics observed in Section 4.2.1, where the system stays mostly aligned along the initially chosen axis of magnetization for energies below a certain threshold. Parts of the following spin wave theory review are taken from [84] and [85].

For the linearization of the Heisenberg model, the ansatz $\mathbf{S}_i \equiv \mathbf{S}_{i,0} + \delta \mathbf{S}_i$ is plugged into the equations of motion Eq. (4.39) to ultimately obtain a dispersion relation for the excitations. The initial spin configuration can be described by $\mathbf{S}_{i,0} = \mathbf{S}_0 e^{i \mathbf{k}_0 \cdot \mathbf{R}_i}$, where $\mathbf{S}_0$ is oriented along the chosen initial axis, $\mathbf{R}_i$ is the vector pointing to lattice site i and $\mathbf{k}_0$ is the wave vector characterizing the antiferromagnetic

order, which in the 1D case simply means $k_0 = \pi$. Eq. (4.39) then becomes

$$
\begin{aligned}
\frac{\mathrm{d}}{\mathrm{d}t}\delta \mathbf{S}_i &= \sum_j J_{ij}\left(\delta \mathbf{S}_i \times \mathbf{S}_{i,0} + \mathbf{S}_{i,0} \times \delta \mathbf{S}_i\right) \\
&= \sum_j J_{ij}\left(\delta \mathbf{S}_i \times \mathbf{S}_0 e^{i\mathbf{k}_0 \cdot \mathbf{R}_i} + \mathbf{S}_0 e^{i\mathbf{k}_0 \cdot \mathbf{R}_i} \times \delta \mathbf{S}_i\right).
\end{aligned}
\tag{4.40}
$$

From these equations of motion it can be seen that the motion of $\delta \mathbf{S}_i$ must be perpendicular to $\mathbf{S}_0$, it is therefore useful to define the variable $S_i^{\pm} = \delta S_i^x \pm i \delta S_i^y$, assuming $\mathbf{S}_0$ points in z-direction.

The solutions to Eq. (4.40) are then of the form

$$
\begin{aligned}
S_i^+ &= \sqrt{\frac{2}{N}}\sum_{\mathbf{k}}\left[A_{\mathbf{k}}e^{i(\mathbf{k}\cdot\mathbf{R}_i - \omega_{\mathbf{k}}t)} + B_{\mathbf{k}}e^{i((\mathbf{k}-\mathbf{k}_0)\cdot\mathbf{R}_i - \omega_{\mathbf{k}}t)}\right] \quad \text{and} \\
S_i^- &= \sqrt{\frac{2}{N}}\sum_{\mathbf{k}}\left[A_{\mathbf{k}}^*e^{-i(\mathbf{k}\cdot\mathbf{R}_i - \omega_{\mathbf{k}}t)} + B_{\mathbf{k}}^*e^{-i((\mathbf{k}-\mathbf{k}_0)\cdot\mathbf{R}_i - \omega_{\mathbf{k}}t)}\right].
\end{aligned}
\tag{4.41}
$$

This corresponds to two spin waves precessing around the initial magnetization axis with the same frequency $\omega_{\mathbf{k}}$ but different amplitudes $|A_{\mathbf{k}} + B_{\mathbf{k}}|$ and $|A_{\mathbf{k}} - B_{\mathbf{k}}|$ on the two sublattices given by the antiferromagnetic order as pictured in Fig. 4.17.

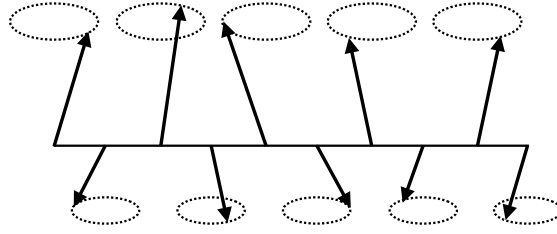**Figure 4.17.:** Spin wave in an antiferromagnetic Heisenberg model. After [84].

Using the Fourier transform of the interaction J_{ij}

$$
J(\mathbf{k}) = \sum_j J_{ij}e^{i\mathbf{k}\cdot(\mathbf{R}_j - \mathbf{R}_i)},
\tag{4.42}
$$

the frequency is found to be

$$
\omega_{\mathbf{k}} = \pm 2S\sqrt{(J(\mathbf{k}_0) - J(\mathbf{k}))(J(\mathbf{k}_0) - J(\mathbf{k} - \mathbf{k}_0))},
\tag{4.43}
$$

or, in the 1D nearest-neighbor case simply

$$\omega_k = \pm 2SJ\sqrt{1 - \cos^2(k)}\,. \tag{4.44}$$

Evidently, the long wavelength limit of the antiferromagnetic spin wave dispersion in the regular nearest-neighbor Heisenberg model is not, as in the ferromagnetic case, quadratic, but linear in k, i.e. $\omega_k \propto |k|$ for small values of k. For a frustrated model with nearest neighbor interactions J_1 and next-to-nearest neighbor interactions J_2 Eq. (4.43) becomes, within the antiferromagnetic phase with $k_0 = \pi$,

$$\begin{aligned}
\omega_k &= 2S\sqrt{(J_2 - J_1 - J_2\cos(2k))^2 - (J_1\cos(k))^2} \\
&\equiv 2SJ\sqrt{(\sin\Phi - \cos\Phi - \sin\Phi\cos(2k))^2 - (\cos\Phi\cos(k))^2}\,,
\end{aligned} \tag{4.45}$$

where in the last line the frustration is parameterized by $J_1 = J\cos\Phi$ and $J_2 = J\sin\Phi$. Fig. 4.18 shows the dispersion relation for different values of Φ, the case $\Phi = 0$ denoting the regular nearest-neighbor only case. Note that $\Phi \approx 0.245$ is the critical value above which the ground state transitions from antiferromagnetic order with $k_0 = \pi$ to spiral order with $k_0 \neq \pi$, more on the $J_1 - J_2$-Heisenberg model can be found in Appendix A.
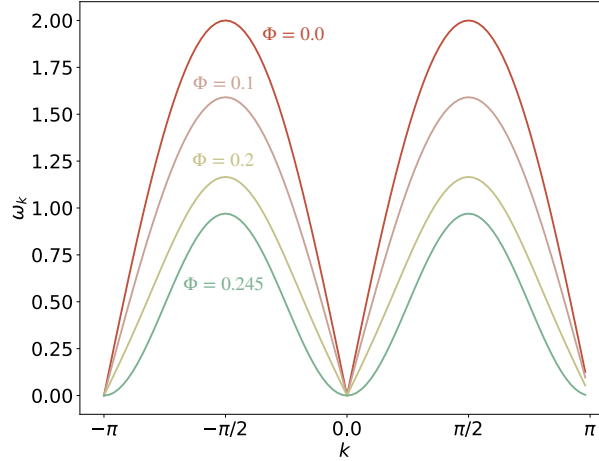
Figure 4.18.: Spin wave dispersion in the antiferromagnetic Heisenberg model Eq. (4.45) with coupling constants $J_1 \equiv J\cos\Phi$ and $J_2 \equiv J\sin\Phi$ for different values of frustration Φ. The red line ($\Phi = 0$) shows the dispersion of the regular nearest-neighbor chain Eq. (4.44).

Inspired by spin wave theory for the Heisenberg model, here too, the equations of motion can be linearized. The complete set of nonlinear differential equations describing the time evolution of the

Kondo lattice system as introduced in Section 4.1.1 is

$$\dot{\mathbf{S}}_i(t) = J\langle\mathbf{s}_i\rangle_t \times \mathbf{S}_i(t) \quad \text{and}$$
$$i\dot{\boldsymbol{\rho}}(t) = [\mathbf{t}_{\text{eff}}\left(\{\mathbf{S}_i\}\right),\boldsymbol{\rho}(t)] \tag{4.46}$$

where the effective hopping matrix

$$\mathbf{t}_{\text{eff}} = \mathbf{t}_{\text{hopp}} + \boldsymbol{\Sigma}\left(\{\mathbf{S}_i\}\right) \tag{4.47}$$

depends on the classical spin configuration $\{\mathbf{S}_i\}$ via the self-energy $\boldsymbol{\Sigma}$ with elements

$$\Sigma_{ii,\sigma\sigma'} = \frac{J}{2}\left(\mathbf{S}_i \cdot \boldsymbol{\sigma}\right)_{\sigma\sigma'}. \tag{4.48}$$

The expectation values of the electron spins $\langle\mathbf{s}_i\rangle$ can be expressed in terms of the one-particle reduced density matrix ρ as follows

$$\langle\mathbf{s}_i\rangle = \frac{1}{2}\text{Tr}\left[\boldsymbol{\sigma}\rho_i\right] = \frac{1}{2}\sum_{\sigma\sigma'}\boldsymbol{\sigma}_{\sigma\sigma'}\rho_{ii,\sigma'\sigma}. \tag{4.49}$$

The ansatz to linearize Eq. (4.46) is then simply

$$\mathbf{S}_i = \mathbf{S}_{0,i} + \delta\mathbf{S}_i \quad \text{and}$$
$$\boldsymbol{\rho} = \boldsymbol{\rho}_0 + \delta\boldsymbol{\rho}. \tag{4.50}$$

Letting ρ_i denote the 2×2 matrix block with entries $\rho_{ii\sigma\sigma'}$ and plugging Eq. (4.50) into Eq. (4.46), the equation of motion for the classical spins becomes, up to first order,

$$\delta\dot{\mathbf{S}}_i = \frac{J}{2}\text{Tr}\left[\boldsymbol{\sigma}\cdot(\boldsymbol{\rho}_{0,i} + \delta\boldsymbol{\rho}_i)\right] \times (\mathbf{S}_{0,i} + \delta\mathbf{S}_i)$$
$$= \frac{J}{2}\left(\text{Tr}(\boldsymbol{\sigma}\cdot\delta\boldsymbol{\rho}_i) \times \mathbf{S}_{0,i} + \text{Tr}(\boldsymbol{\sigma}\cdot\boldsymbol{\rho}_{0,i}) \times \delta\mathbf{S}_i\right), \tag{4.51}$$

where it was also used that $\langle\mathbf{s}_{0,i}\rangle \times \mathbf{S}_{i,0} = 0$ since in the initial state, electrons and classical spins are collinear per construction. The linearized equation of motion for the density matrix is

$$\delta\dot{\boldsymbol{\rho}} = -i[\mathbf{t}_{\text{eff}}\left(\{\mathbf{S}_0 + \delta\mathbf{S}\}\right),\boldsymbol{\rho}_0 + \delta\boldsymbol{\rho}]$$
$$= -i\left([\mathbf{t}_{\text{eff}}\left(\{\mathbf{S}_0\}\right),\delta\boldsymbol{\rho}] + [\boldsymbol{\Sigma}(\delta\mathbf{S}),\boldsymbol{\rho}_0]\right), \tag{4.52}$$

where $[\mathbf{T}_{\text{eff}}(\mathbf{S}_0),\boldsymbol{\rho}_0] = 0$, since $\boldsymbol{\rho}_0$ is a function of $\mathbf{T}_{\text{eff}}(\mathbf{S}_0)$, was used. Eqs. (4.51) and (4.52) can be written more compactly in matrix form

$$\dot{\mathbf{x}}(t) = \mathbf{M}\,\mathbf{x}(t), \tag{4.53}$$

where $\mathbf{x}(t) = (\delta\mathbf{S},\delta\boldsymbol{\rho})^T$ is the $(3L + 4L^2)$-dimensional vector of spin and electron degrees of freedom

and $\mathbf{M}$ is the $(3L + 4L^2) \times (3L + 4L^2)$-dimensional constant coefficient matrix. In block matrix form this can be written as

$$\begin{pmatrix} \delta\dot{\mathbf{S}} \\ \delta\dot{\boldsymbol{\rho}} \end{pmatrix} = \begin{pmatrix} \mathbf{M}_{SS} & \mathbf{M}_{SE} \\ \mathbf{M}_{ES} & \mathbf{M}_{EE} \end{pmatrix} \begin{pmatrix} \delta\mathbf{S} \\ \delta\boldsymbol{\rho} \end{pmatrix} \tag{4.54}$$

with matrix elements

$$M_{i\alpha,i'\alpha'}^{SS} = \frac{J}{2} \sum_{\sigma\sigma'} \sum_{\beta}^{xyz} \varepsilon_{\alpha\beta\alpha'} \sigma_{\sigma\sigma'}^{\beta} \rho_{0,ii\sigma\sigma'} \delta_{ii'}$$

$$M_{i\alpha,i'j'\sigma'\tau'}^{SE} = \frac{J}{2} \sum_{\beta\gamma}^{xyz} \varepsilon_{\alpha\beta\gamma} \sigma_{\sigma'\tau'}^{\beta} S_{0,i\gamma} \delta_{ii'} \delta_{i'j'}$$

$$M_{ij\sigma\tau,i'\alpha'}^{ES} = -i\frac{J}{2} \sum_{\mu} \sigma_{\sigma\mu}^{\alpha'} \rho_{0,i'j\mu\tau} \delta_{ii'} + i\frac{J}{2} \sum_{\mu} \sigma_{\mu\tau}^{\alpha'} \rho_{0,ii'\sigma\mu} \delta_{i'j} \tag{4.55}$$

$$M_{ij\sigma\tau,i'j'\sigma'\tau'}^{EE} = -it_{\text{hopp},ii'} \delta_{\sigma\sigma'} \delta_{\tau\tau'} \delta_{jj'} + it_{\text{hopp},j'j} \delta_{\sigma\sigma'} \delta_{\tau\tau'} \delta_{ii'}$$

$$\qquad\qquad - i\frac{J}{2} \sum_{\alpha} S_{0,i\alpha} \sigma_{\sigma\sigma'}^{\alpha} \delta_{ii'} \delta_{jj'} \delta_{\tau\tau'} + i\frac{J}{2} \sum_{\alpha} S_{0,i'\alpha} \sigma_{\tau'\tau}^{\alpha} \delta_{ii'} \delta_{jj'} \delta_{\sigma\sigma'} .$$

A system of coupled differential equations with constant coefficients of the form Eq. (4.53) has a fundamental system of solutions given by

$$\{\mathbf{v}_1 e^{\lambda_1 t}, ..., \mathbf{v}_n e^{\lambda_n t}\} , \tag{4.56}$$

where $\mathbf{v}_i$ are eigenvectors to the eigenvalues λ_i of $\mathbf{M}$ and the matrix dimension in this case is $n = 3L + 4L^2$. A solution to Eq. (4.53) can therefore be expressed as

$$\mathbf{x}(t) = \sum_{j=1}^{n} c_j \mathbf{v}_j e^{\lambda_j t} , \tag{4.57}$$

where the coefficients c_j need to be chosen to satisfy the initial condition $\mathbf{x}(t = 0) \equiv \mathbf{x}_0$, i.e.

$$\mathbf{V}\mathbf{c} = \mathbf{x}_0 \quad \text{or} \quad \mathbf{c} = \mathbf{V}^{-1}\mathbf{x}_0 . \tag{4.58}$$

The vector $\mathbf{c}$ is composed of coefficients c_j corresponding to the columns $\mathbf{v}_j$ of the matrix $\mathbf{V}$ that diagonalizes $\mathbf{M}$. Note that a peculiarity of the model here is that the matrix $\mathbf{M}$ is neither hermitian nor anti-hermitian since even though $\mathbf{M}_{SS}^{\dagger} = -\mathbf{M}_{SS}$ and $\mathbf{M}_{EE}^{\dagger} = -\mathbf{M}_{EE}$, it can be easily seen that $\mathbf{M}_{SE}^{\dagger} \neq -\mathbf{M}_{ES}$. A numerical diagonalization still shows only imaginary eigenvalues that occur in pairs $(\lambda_i, -\lambda_i)$, indicating the solutions are of the form

$$\mathbf{x}(t) = \sum_{i=1}^{n/2} \left(c_i \mathbf{v}_i e^{i\omega_i t} + c_{-i} \mathbf{v}_{-i} e^{-i\omega_i t} \right) , \tag{4.59}$$

and can thus be pictured as oscillations around $\mathbf{x}_0$ with frequencies $\omega_i \equiv \mathrm{Im}(\lambda_i)$. Just as for $\omega_{\mathbf{k}}$ in the solution of Heisenberg model spin waves in Eq. (4.43), here too, the spectrum is symmetric and for each frequency ω_i there are two solutions precessing in different directions around $\mathbf{x}_0$.
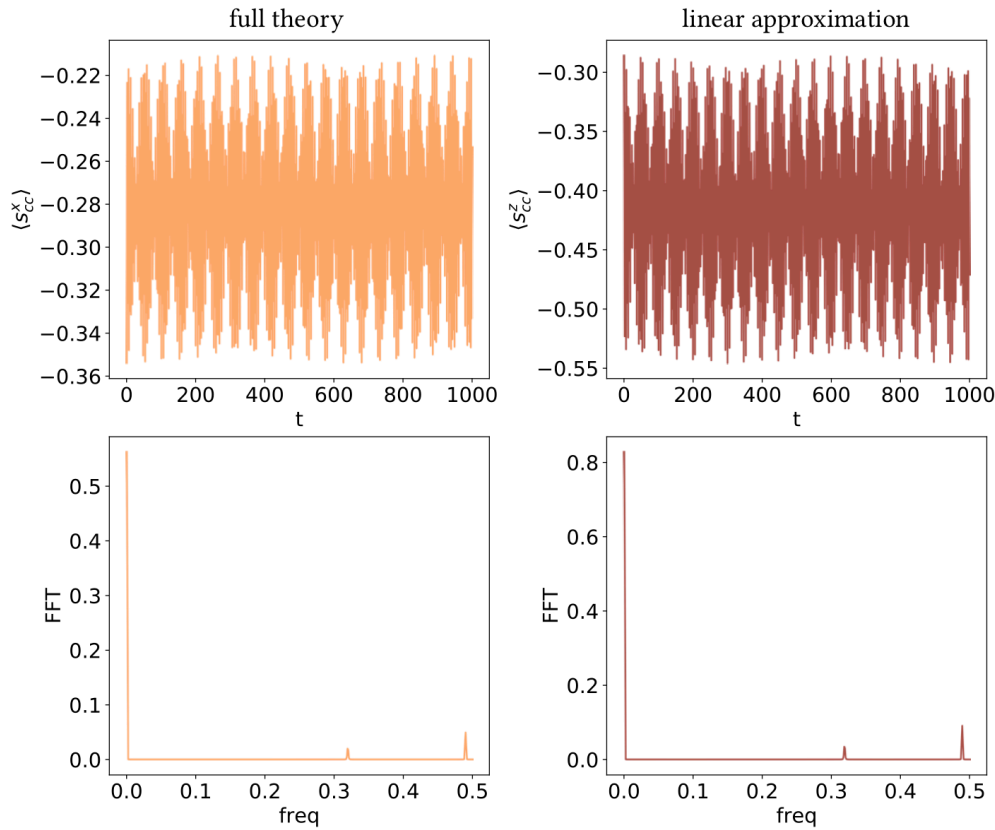

Figure 4.19.: Comparison between full theory (left column) and linear approximation (right column) for a lattice of size $L = 8$ at $\varphi = 0.0$ and $J = 3.0$. The upper left panel shows the time evolution of the electron spin component $\langle s_{cc}^x \rangle$ after a quench $J = 4.9 \to 3.0$, the lower left panel the corresponding numerical fast Fourier transform (FFT) plotted against frequencies. The upper right panel shows $\langle s_{cc}^z \rangle$ calculated from the solution $\delta\rho$ of the ode of the linear approximation Eq. (4.54), the lower right panel again the corresponding FFT against frequencies.

After finding the numerical solution $\mathbf{x}(t) = (\delta\mathbf{S}, \delta\boldsymbol{\rho})^T$ in this way, it can be used to calculate the time evolution of observables in the framework of the linear approximation. Fig. 4.19 shows a comparison of the time evolution of the full theory and the solution of the linear approximation differential equation Eq. (4.54). In both cases, all components of the classical spins are constant for all times, as are two of the electron spin expectation values. Only the component in the direction of the initial spin configuration - x in the full theory, z in the linear approximation - is fluctuating as a function of time, as plotted in the top row of Fig. 4.19. In the upper left panel, $\langle s_{cc}^x \rangle$ is plotted as a function of time for a system of size

$L = 8$ after a quench $J = 4.9 \rightarrow 3.0$ at $\varphi = 0$. The oscillation looks similar to the time evolution of $\langle s_{cc}^z \rangle$ resulting from the solution of the linear approximation $\delta\rho$ plotted in the upper right panel. This is confirmed by the numerical fast Fourier transform plotted in the bottom row for both cases, that show a similar frequency spectrum. The amplitude, however, does not match exactly. The amplitude of the oscillation of $\langle s_{cc}^x \rangle$ in the full theory depends on the size of the quench, i.e. the energy introduced into the system, the frequency spectrum is similar for all quenches below the critical energy E_{crit} above which the dynamics of the classical spins starts.

The linear approximation thus exactly reproduces the dynamics compatible with the equations of motion first discussed in Section 4.1.2, as it should. No chaotic motion can be expected from such an approximation and therefore no exponential sensitivity to perturbations that could potentially trigger any other dynamics than the one pictured in Fig. 4.19. Even though the derivation is similar and the models share the presence of classical spins, the "spin-wave-like" excitations here are of a different type than the well known ones found for the Heisenberg model. The linearized equations of motion Eq. (4.54) mix the classical spin and electron components, the nature of excitations is therefore of a fundamentally different nature than in the classical spin-only Heisenberg model.
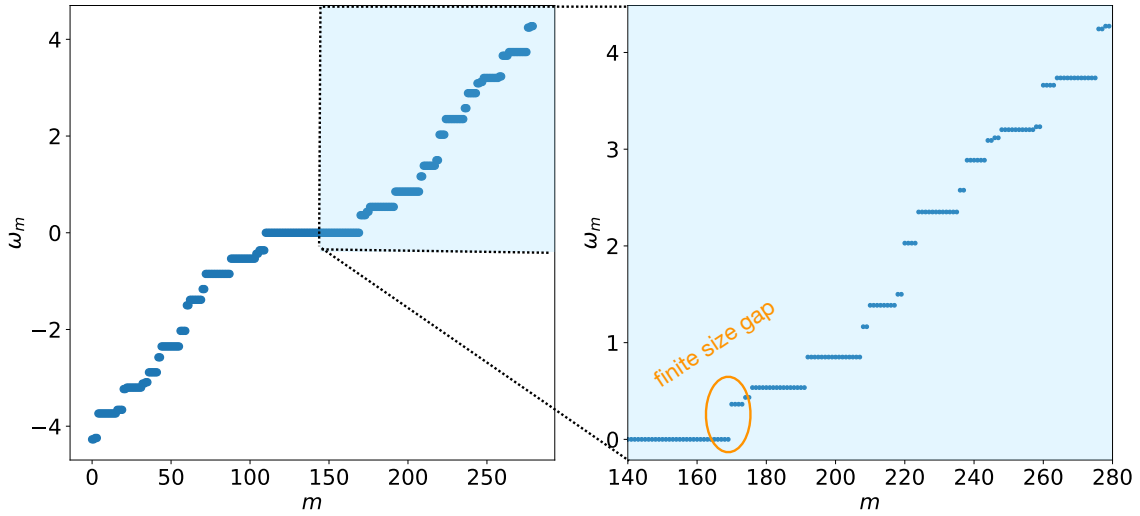

Figure 4.20.: Left panel: Full spectrum of eigenvalues $\omega_m \equiv \mathrm{Im}(\lambda_m)$ of coefficient matrix in Eq. (4.53) for a system with $L = 8$, $\varphi = 0$ and $J = 3$ plotted against diagonalization index m. Right panel: Zoom into $\omega_m > 0$ with (first) finite size gap marked in orange.

The entire spectrum of eigenvalues, or rather of the nonzero imaginary ones ω_m, is plotted against the diagonalization index m in Fig. 4.20 for a system with $L = 8$, $J = 3$ and $\varphi = 0$. The left panel shows the symmetry of eigenvalues, for each ω_m there is a corresponding $-\omega_m$, imaginary eigenvalues always come in pairs. There seems to be an additional symmetry, as each of the ω_m is at least doubly

degenerate. A plot in k-space, that is not available here, would perhaps show a similar symmetry around $k = 0$ as in the Heisenberg model in Fig. 4.18. The form of the dispersion ω_k seems to be more complex here, however, as the degeneracy is not uniform.

The degeneracy of the eigenvalue $\omega_m = 0$ is particularly high, even when accounting for the factor 2 of the $\pm$ symmetry. For a better understanding of what could be the cause, it might be useful to consider the simpler Heisenberg model. The solution of the spin wave theory presented above has $2L$ components, but if it would be restated in matrix form analogous to Eq. (4.54), the formal solution would have $3L$ components. The extra L components correspond to the components in the direction of the initial configuration. Since it was shown above, that the linear deviation $\delta\mathbf{S}$ must lie in the perpendicular plane, these L eigenvalues must therefore be zero. Here, the situation is much more complicated. If the logic of the Heisenberg model were applied, it would account for $5L$ of the degenerate eigenvalues, since without the exponential sensitivity on perturbations, which is absent in the linear approximation, all $3L$ components of the classical spin and $2L$ components of the local electron spin would be constant. In addition, there are in both cases "physical" zero modes that are also obtained by an analytical solution. In case of the Heisenberg model, the zero modes correspond to a collective uniform rotation of all spins that do not change the state, and are in fact the zero-frequency Goldstone modes connected to the breaking of the $SO(3)$ symmetry.
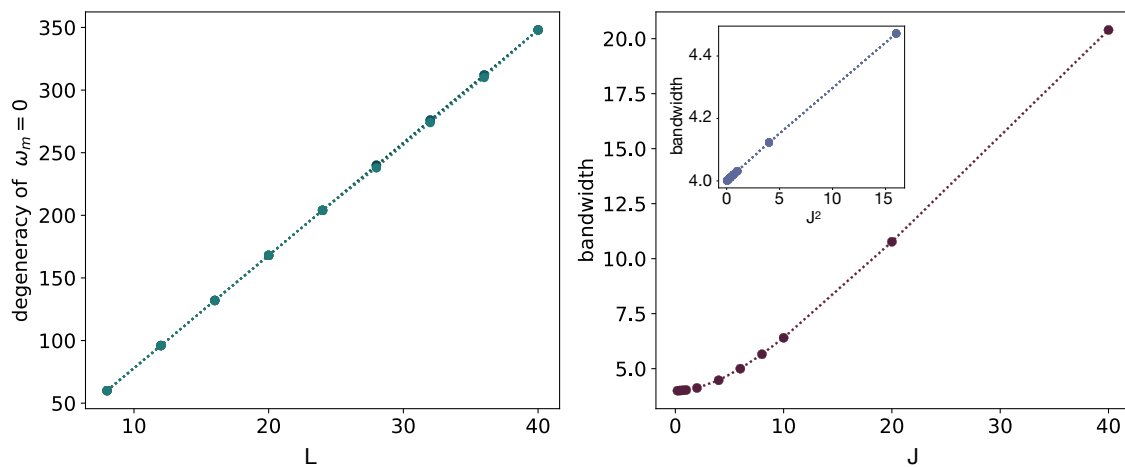

Figure 4.21.: Left panel: degeneracy of $\omega_m = 0$ as a function of L. Right panel: bandwidth of ω_m spectrum as a function of J. The inset shows the J^2 proportionality for small to medium J. Both panels are for $\varphi = 0$.

The degeneracy of $\omega_m = 0$ is plotted as a function of L in the left panel of Fig. 4.21. The proportionality is linear to L with the same factor for all values of J. The proportionality constant is larger than 5, there are therefore more L-dependent zero modes than the ones mentioned above. A further analysis is difficult, however, as the $4L^2$ elements of the density matrix $\boldsymbol{\rho}$ are with a few exceptions, such as the

components of $\langle \mathbf{s}_i \rangle$, not very intuitive degrees of freedom.

The right panel of Fig. 4.21 shows the bandwidth of the positive half of the spectrum, i.e. $\max(\omega_m)$, as a function of J. The minimum value at $J = 0$ is 4, which is just the 1D bandwidth of electronic excitations without the field induced by the classical spins. After an increase $\propto J^2$ shown also in the inset for small to medium values of J, in the strong coupling limit starting at $J \approx 10$ the bandwidth takes the value $J/2$, which is the "Slater gap" also encountered in Section 2.2.1 at the boundaries of the magnetic Brillouin zone for antiferromagnetic spin configurations. The spin-wave-like excitations therefore lie within the Slater gap, i.e. below the purely electronic excitations of the system. For all values of J, the bandwidth is independent of L.

In the thermodynamic limit $L \to \infty$, the spectrum ω_m becomes continuous and the energy needed to excite the first mode above the zero mode is infinitesimally small, the spectrum is said to be *gapless*. For finite L, this is not the case, as can be seen in Fig. 4.20 by the example of $L = 8$. The dependence of this finite size gap, which is marked in orange in Fig. 4.20, on L and J is shown in the left and right panel of Fig. 4.22, respectively.
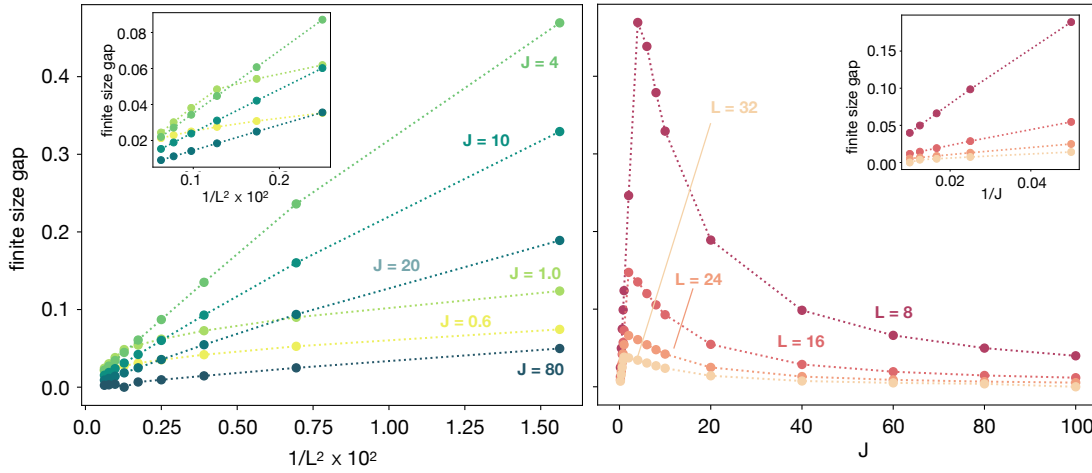

Figure 4.22.: Finite size gap (see orange marking in Fig. 4.20) as a function of $1/L^2$ (left panel) and J (right panel) for $\varphi = 0$. The inset in the left panel shows the linear behavior with $1/L^2$ for larger L. The inset in the right panel shows the $1/J$-proportionality for larger J.

The left panel shows that for all values of J, the gap is roughly proportional to $1/L^2$ for large L, in particular for larger values of L, which are shown also in the inset. For smaller values of J as indicated by the yellow and light green lines, the proportionality seems to change suddenly at some point, but even then the gap remains proportional to $1/L^2$. The spin wave spectrum in the Heisenberg model for the regular unfrustrated antiferromagnetic chain is linear for small values of k, which should result in a $1/L$ proportionality of the gap due to evenly spaced k-values. This stands in contrast to the results

found here, but in this case the excitations are a combination of classical spins and electrons and thus fundamentally different from the well known spin waves in the Heisenberg model, evidently they also result in a different, i.e. possibly quadratic dispersion for small k.

The J-dependence of the finite size gap is plotted in the right panel of Fig. 4.22. The qualitative behavior is similar for all values of L, with a stronger J-dependence for smaller values of L. This of course simply reflects the fact that the gap closes for $L \to \infty$. After a linear increase until $J \approx 5$, the gap then decreases as $\propto 1/J$ also shown in the inset, and ultimately, depending on L, nearly closes for very large J. For lattices with larger L, the dependence on J becomes smaller and smaller until eventually the gap will be closed for all values of J.

This finite size gap can help explain the ergodicity threshold that was found numerically in Section 4.2.1. Fig. 4.23 shows a comparison between the critical energy needed to start dynamics E_{crit} (blue) and the gap of the spectrum of linear excitations (orange). Both are, at least approximately, $\propto 1/L^2$ with the critical energy going to zero slightly faster with increasing L.
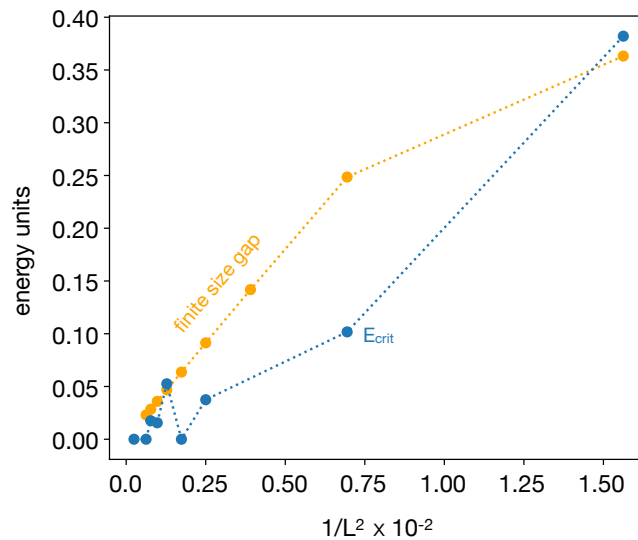

Figure 4.23.: Critical energy (blue) and finite size gap of the linear approximation (orange) plotted against $1/L^2$ for $J = 3$ and $\varphi = 0$.

Below the critical energy E_{crit}, the system is "trapped" in the linear regime and remains in the initial antiferromagnetic configuration forever. It is therefore trivially long-range ordered. The Mermin-Wagner theorem [55] rigorously proves the absence of long range ordered ferro- or antiferromagnetism in one and two dimensional systems at finite temperatures. For small but finite $T > 0$, the order is destroyed by the spin wave excitations that cost vanishingly small energy to excite and whose total number diverges for dimensions $d = 1$ and $d = 2$ [85]. For finite system sizes, however, the spin

wave spectrum is gapped, and the order-destroying excitations cost a finite amount of energy. Here, the order is eventually destroyed by the ergodic behavior of the system above the ergodicity threshold, which can also be seen as the excitation gap needed to excite the spin-wave-like excitations. The results presented here therefore do not contradict the Mermin-Wagner theorem. Another viewpoint is, that the Mermin-Wagner theorem only applies to ergodic systems, as it relies on the validity of the ergodic theorem Eq. (4.20) to provide valid expectation values for the Bogoliubov inequality.

Technically, the ergodicity threshold described here could be called a finite size effect. The same can, however, also be said of the stochasticity threshold of the FPU paradox mentioned in Section 4.2.2, that nevertheless was an important result and triggered much research on the connection between classical dynamics and statistical mechanics. The question of how many degrees of freedom are needed to expect statistical behavior is still difficult to answer and certainly depends on the specific situation. Fermi et. al. showed in their case, $n = 32, 64$ was not sufficient to trigger mixing and therefore statistic behavior. The results presented here indicate that, at least in this case, $L = 32, 64$ might also not be sufficient, but likewise $L = \mathcal{O}(10^{23})$ is far from necessary, as the ergodicity threshold closes very fast, i.e. as $1/L^2$. Another point could be made that even though the system above E_{crit} is ergodic in the limit $t \to \infty$, there is still a remnant of the linear regime present in form of the staggered magnetization m_{s} that is approximately conserved on long time scales as shown in Fig. 4.10 for $L = 96$.

4.3. Dimerization Transition

In the previous section, the dynamics following parameter quenches within the antiferromagnetic phase were found to be ergodic only above a critical energy. While they were found to be certainly non-ergodic below this threshold, even above the timescales were much too slow to actually observe a true covering of the entire phase space, an appropriate description would therefore be *weakly chaotic*. Some examples of truly chaotic dynamics can be obtained by quenches across phase boundaries, as will be demonstrated in this section by example of quenches across the antiferromagnetic-dimerization and spiral-dimerization transition illustrated in Fig. 4.2 and marked with ②.

After determining ergodic properties of a system, new questions arise. The focus in this section will be on whether or not the system reaches a new equilibrium state, i.e. thermalizes, on observable time scales, and the nature of this new equilibrium in particular concerning the presence or absence of long range order. Before discussing numerical results, the following sections first aim to introduce some important concepts such as phase transitions, long range order and thermalization.

4.3.1. Phase Transitions

A general, but precise definition of phase transitions or even simply a phase is difficult to state. Typically, a system is said to be in a certain *phase* if it is in an equilibrium state that can be characterized by

few thermodynamic variables. This can be a state of matter such as liquid, solid, etc., or more complex such as magnetic or superconducting. If by changing a system parameter - often, but not always the temperature - the general characteristics of the system change, it is said to undergo a *phase transition*. This is accompanied by non-analyticities of thermodynamic functions that characterize this transition. They can be broadly separated into two types: When the first derivative of a thermodynamic potential, such as the free energy, has a discontinuity at the point of the phase transition, it is said to be of *first order*. If, on the other hand, the discontinuity appears in one of the higher derivatives such as a susceptibility, it is called a *continuous phase transition*. In finite systems such as present here, there can be no real discontinuities and therewith no real phase transitions at finite temperatures. This can be illustrated by a short example taken from [86]. Consider the temperature dependent correlation length or spatial extent of fluctuations ξ of a physical quantity in the vicinity of a continuous phase transition. At the point of the phase transition, i.e. the critical temperature T_c, this correlation length ξ diverges to infinity. This is of course impossible in any finite system, as ξ naturally cannot exceed the system size L. The way in which it diverges can be characterized by a so-called critical exponent, which depends on very few system properties such as the dimensionality of the system and the range of interactions. Consider for example

$$\xi \approx \xi_0 t^{-2/3} \quad \text{with} \quad t \equiv \frac{T - T_c}{T_c} . \tag{4.60}$$

For a quantitative estimate of *how* infinite a system needs to be, consider $\xi_0 \approx 10$ Å the correlation length far away from the critical point. In this case, the correlation length reaches a system size of $L = 1$ cm at $t = 10^{-11}$, i.e. finite size effects are practically unobservable. This example saves the concept of phase transition at least for experimentalists, as it is not necessary to have a truly infinite sample, but for numerical calculations the problem remains and must be combatted with careful finite size scaling [86]. For the remainder of this thesis it is necessary to understand all phase transitions mentioned to be in fact more of a *crossover* from one phase to the next without a true non-analyticity, even though the term might sometimes be used for simplicity.

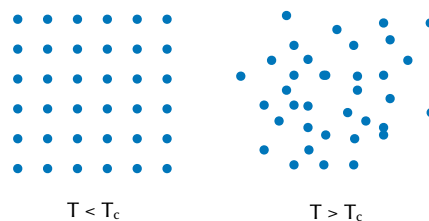$T < T_c$ $T > T_c$

Figure 4.24.: Schematic picture of a solid to liquid phase transition, where the system is ordered at low temperatures (left) and disordered at high temperatures (right) with T_c denoting the critical temperature.

Besides categorizing into first order and second order (continuous), there is another important quality that fundamentally distinguishes individual phase transitions. The phase transitions that can be experienced in everyday life, such as the melting of ice, are usually a function of temperature. By heating the ice, thermal fluctuations eventually destroy macroscopic order of the crystal structure as shown schematically in Fig. 4.24. The corresponding discussion relating to the symmetry of each phase will be continued in the next section. The point here is that there are also phase transitions that can take place entirely at zero temperature, then of course as a function of some non-thermal system parameter. In this case, the order is not destroyed by thermal but by quantum fluctuations, this class of transitions is therefore called *quantum phase transitions*. As the critical behavior in the vicinity of a transition taking place at finite temperature is dominated by the thermal fluctuations, all transitions taking place above $T = 0$ are generally called *classical* independent of other system characteristics [87].

Here, any transition that might be observed is induced by a parameter quench as introduced in Section 4.1.2. As any parameter quench will necessarily introduce energy ΔE as defined in Eq. (4.24) into the system, in this framework there are no zero temperature phase transitions. As finite temperature transitions are always *classical*, in spite of the system here being a *quantum-classical hybrid*, there are no quantum phase transitions to consider, at least as a consequence of parameter quenches. It is therefore important to realize that a parameter quench drawn in the flat $J - \varphi$ equilibrium phase diagram as pictured in Fig. 4.2 is not an accurate depiction of the resulting phase transition. A more authentic illustration of the quench is obtained by adding an extra dimension - the temperature - to the phase diagram as shown in Fig. 4.25.

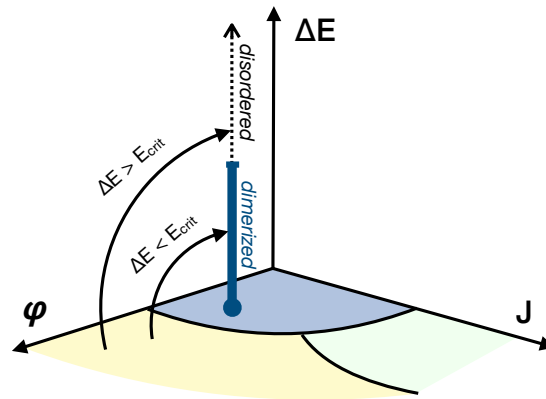**Figure 4.25.:** Schematic picture of quenches in the finite-temperature phase diagram. The corresponding zero temperature phase diagram is introduced in Chapter 3 and pictured in Fig. 3.3.

A quench starting in the spiral or antiferromagnetic and ending in the dimerized phase as shown in Fig. 4.25 is therefore not guaranteed to truly result in a dimerized phase after the system has thermalized

- if the energy is greater than a critical value connected to some unknown critical temperature, the outcome will simply be a disordered system.

4.3.2. Spontaneous Symmetry Breaking and Long Range Order

Intimately connected to the concept of phase transitions is the notion of *spontaneously broken symmetry*. The solid-liquid phase transition sketched schematically in Fig. 4.24 shows what is often the case for a phase transition - one phase has a different symmetry than the other. To be more precise, "having a symmetry" means that the system is invariant under symmetry operations. If this group contains a countable number of elements, it is called a *discrete symmetry*, such as the rotational symmetry of a cube, if it contains a continuum of elements, it is called a *continuous symmetry*, such as the rotational symmetry of a sphere [85]. In this case, the corresponding Hamiltonian commutes with the generators of respective symmetry group. In the picture in Fig. 4.24, the liquid phase on the right expresses a higher symmetry than the left, since no point in space is particularly special and any rotation or transposition will return a similar state. The solid on the left, however, has a discrete symmetry, where only rotations of exactly $90°$ and transformations according to the lattice spacing will leave the system invariant. If the low-temperature ground state of a system described with a Hamiltonian that has a higher symmetry such as pictured on the right in Fig. 4.24 "chooses" an alignment with a lower symmetry such as pictured on the left, the system is said to have *spontaneously broken symmetry*.

Example: The Ising Model

Consider the free energy of a system $F = E - TS$. At high temperatures, the second term will dominate and F is minimized by maximizing the entropy S. For low temperatures, however, it might be favorable to instead minimize the internal energy E. If the two resulting macroscopic states differ, then the system must have undergone a phase transition at some temperature T_c. To illustrate this concept, first an example of a system with discrete symmetry taken from [86] will be considered. The simplest imaginable model for magnetism and a paradigm for statistical properties of magnets is the Ising model that is described by

$$H = J \sum_{\langle ij \rangle} S_i S_j - B \sum_{i=1}^{N} S_i \tag{4.61}$$

where $\langle ij \rangle$ denotes the sum taken over nearest neighbors coupled with J and $S_i = \pm 1$ is a classical spin that can only take two values: up or down. At high temperatures, the free energy is minimized by maximum entropy that produces an entirely disordered state. At zero temperature, however, the free energy that is then just the internal energy E, is minimized by an ordered spin configuration that depends on the coupling constant J and external magnetic field B. By the above argument, this indicates the existence of a phase transition. It is, however, also possible to construct an argument against the existence of a phase transition, as will be shown in the following.

The external magnetic field B induces a magnetization per site M that can be obtained by differentiating the free energy

$$F = -k_B T \ln Z \quad \text{with} \quad Z = \text{Tr}\, e^{-\beta H} \tag{4.62}$$

with respect to B:

$$
\begin{aligned}
M &\equiv \frac{1}{N} \sum_{i=1}^{N} \langle S_i \rangle = -\frac{1}{N} \frac{\partial F}{\partial B} \quad \text{with} \\
\frac{\partial F}{\partial B} &= -k_B T \frac{1}{\text{Tr}\, e^{-\beta H}} \text{Tr}\, \frac{S_i}{k_B T} e^{-\beta H} = -\langle S_i \rangle\,.
\end{aligned}
\tag{4.63}
$$

Evidently, for $B > 0$ the ground state spin configuration is $S_i = +1 \; \forall i$ and thus $M = +1$, analogously $M = -1$ for $B < 0$. The system must therefore undergo a transition at $B = 0$.

It can easily be seen that the system is symmetric under up-down symmetry, also called time-reversal or Z_2 symmetry. Eq. (4.61) implies

$$H(B, J, \{S_i\}) = H(-B, J, \{-S_i\})\,. \tag{4.64}$$

For any function G depending on the spin configuration $\{S_i\}$

$$\sum_{\{S_i = \pm 1\}} G(\{S_i\}) = \sum_{\{S_i = \pm 1\}} G(\{-S_i\}) \tag{4.65}$$

holds. From both Eq. (4.64) and Eq. (4.65) it follows for the partition function Z:

$$
\begin{aligned}
Z(-B, J, T) &= \sum_{\{S_i = \pm 1\}} \exp[-\beta H(-B, J, \{S_i\})] \\
&= \sum_{\{S_i = \pm 1\}} \exp[-\beta H(-B, J, \{-S_i\})] \\
&= \sum_{\{S_i = \pm 1\}} \exp[-\beta H(B, J, \{S_i\})] \\
&= Z(B, J, T)\,,
\end{aligned}
\tag{4.66}
$$

and therefore for the free energy

$$F(B, J, T) = F(-B, J, T)\,. \tag{4.67}$$

Using this, the magnetization M in Eq. (4.63) becomes

$$NM(B) = -\frac{\partial F(B)}{\partial B} = -\frac{\partial F(-B)}{\partial B} = \frac{\partial F(-B)}{\partial(-B)} = -NM(-B)\,, \qquad (4.68)$$

which leads for $B = 0$ to the contradiction

$$M(0) = -M(0) = 0\,. \qquad (4.69)$$

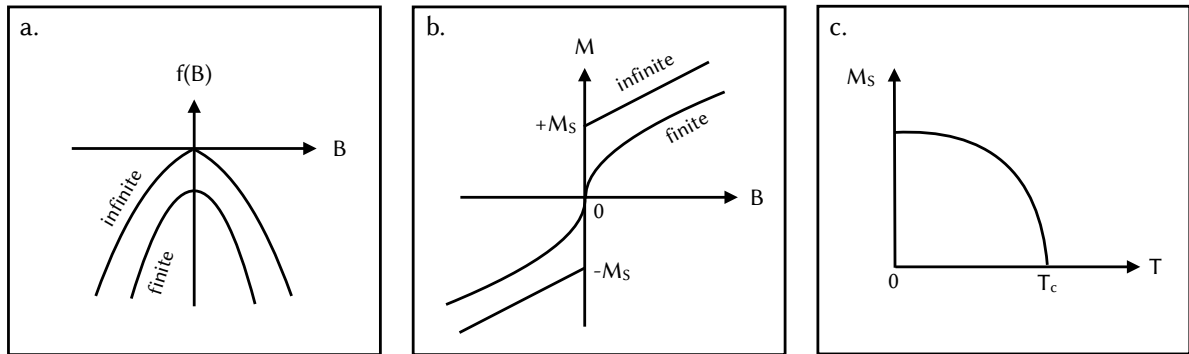There can thus be no magnetization in zero field and therefore no phase transition.

Figure 4.26.: a. Free energy density as a function of magnetic field B for finite and infinite systems and $T < T_c$. b. Magnetization M as a function of external magnetic field B. c. Spontaneous magnetization as a function of temperature. All plots after [86].

This is, however, only correct for finite systems. In the thermodynamic limit $N \to \infty$, the free energy density $f \equiv \frac{F}{N}$ can develop a discontinuity in its first derivative $\partial f / \partial B$. $f(B)$ is a convex up function, but $f(B) = f(-B)$ only implies $M(0) = 0$ if $f(B)$ is smooth at $B = 0$ and left and right derivatives are equal, as shown in Fig. 4.26 a. for a finite system. The behavior sketched in Fig. 4.26 satisfies all analytical properties of a free energy density but still allows for a phase transition in the thermodynamic limit. The magnetization as a function of the external field B is shown in Fig. 4.26 b. where the spontaneous magnetization $M(0) \equiv M_S$ is given by

$$M_S = \lim_{B \to 0^+} -\frac{\partial f(B)}{B} \quad \text{and} \quad -M_S = \lim_{B \to 0^-} -\frac{\partial f(B)}{B}\,. \qquad (4.70)$$

The paradox can therefore be resolved by the realization that the thermodynamic limit $N \to \infty$ does not necessarily commute with the limit $B \to 0$, i.e.

$$\lim_{N \to \infty} \lim_{B \to 0} \frac{1}{N} \frac{\partial F(B)}{\partial B} = 0 \quad \text{while} \quad \lim_{B \to 0} \lim_{N \to \infty} \frac{1}{N} \frac{\partial F(B)}{\partial B} \neq 0\,. \qquad (4.71)$$

At increasing temperature, the thermal fluctuations destroy the magnetic order, eventually leading to

$M_S = 0$ at T_c as shown in Fig. 4.26 c.. Below T_c, even though the Hamiltonian is invariant under time-reversal symmetry $\{S_i\} \to \{-S_i\}$, the statistical expectation values $\langle S_i \rangle \neq 0$ are not, which is an example of spontaneous symmetry breaking.

Strictly speaking, the plot of $M_S(T)$ in Fig. 4.26 c. is only correct for a system with dimension $d > 1$. For $T > 0$, there is no long range order in a one dimensional nearest-neighbor Ising model. In fact, there is a rather general argument for this given in [86,88]. Consider the ferromagnetic ground state with all spins aligned at $T = 0$. In this ordered state, the entropy is zero and the free energy thus given by

$$F_N = -NJ. \tag{4.72}$$

Increasing the temperature produces thermal fluctuations, i.e. spin flips. Now consider the state, where the spins are flipped such that there are two domains … ↑↑↑↓↓ … present in the system. The interface between them has an energy cost of $\Delta E = 2J$, for the internal energy of the domain state follows therefore

$$E_N = -NJ + 2J. \tag{4.73}$$

Because, in a system with periodic boundary conditions, this domain can be at any of the N sites, the corresponding entropy is given by

$$S_N = k_B \log N. \tag{4.74}$$

The difference in free energy between the ferromagnetic and the domain state is thus

$$\Delta F = (-NJ + 2J - k_B T \log N) - (-NJ) = 2J - k_B T \log N, \tag{4.75}$$

which, for any $T > 0$, goes to $\Delta F \to -\infty$ as $N \to \infty$. The system can therefore always lower the energy by creating a domain wall, and even further by splitting each domain in two and so on. This can be continued until the long range order is destroyed. There is thus no phase transition in the 1D Ising model for $T > 0$.

Quasi-Averages

The paradox of non-commuting limits can be stated in more general terms as done for example in [89]. In systems with spontaneous symmetry breaking, Bogoliubov proposed the concept of *quasi-averages* [90]. Normally, for a system in statistical equilibrium, the expectation value of an operator A is given by

$$\langle A \rangle \equiv \mathrm{Tr} \left(\rho A \right) = \mathrm{Tr} \left(e^{-\beta \mathcal{H}} A \right) \tag{4.76}$$

with the density operator $\rho = \exp(-\beta \mathcal{H})$ and grand-canonical Hamiltonian $\mathcal{H} = H - \mu \hat{N}$. Now taking the thermodynamic limit $N \to \infty$ turns out to be surprisingly non-trivial. Consider for example

a small perturbation ν added to the system via an addition $H_\nu = \nu H'$

$$\mathcal{H}_\nu = H + H_\nu - \mu \hat{N} \,. \tag{4.77}$$

Then taking again $\nu \to 0$ can result in a contradiction for the infinite system. For $\nu = 0$ the average in the infinite system is simply given by

$$\langle A \rangle = \lim_{N \to \infty} \text{Tr} \left(e^{-\beta \mathcal{H}} A \right) \,. \tag{4.78}$$

For the *quasi-average*, however, the limits are taken the other way around, i.e.

$$\langle A \rangle_q \equiv \lim_{\nu \to 0} \lim_{N \to \infty} \text{Tr} \left(e^{-\beta \mathcal{H}_\nu} A \right) \,. \tag{4.79}$$

Now suppose that the Hamiltonian $\mathcal{H}$ displays a continuous symmetry $\mathcal{S}$, i.e. it commutes with generators $\Gamma_{\mathcal{S}}^i$ of the corresponding symmetry group

$$[\mathcal{H}, \Gamma_{\mathcal{S}}^i] = 0 \,. \tag{4.80}$$

If some operator B is *not* invariant under $\mathcal{S}$ the commutator is nonzero

$$[B, \Gamma_{\mathcal{S}}^i] \equiv C^i \neq 0 \,. \tag{4.81}$$

Due to the cyclic invariance of the trace, the regular expectation value, i.e. Eq. (4.78), of C^i vanishes

$$\langle C^i \rangle = 0 \tag{4.82}$$

in contrast to the quasi-average

$$\langle C^i \rangle_q = \lim_{\nu \to 0} \lim_{N \to \infty} \text{Tr} \left(e^{-\beta \mathcal{H}_\nu} [B, \Gamma_{\mathcal{S}}^i] \right) \neq 0 \,. \tag{4.83}$$

Even though this last argument was given for quantum systems, the classical case can be argued very similarly. In the classical case, averages can be calculated just as in Eq. (4.76) with the ρ being the (classical) Boltzmann distribution. The same problem with the thermodynamic limit arises, since the symmetry of the Hamiltonian (and therewith ρ) determines the value of averages like Eq. (4.76) of observables like the magnetization. The solution are again quasi-averages where the thermodynamic limit together with the limit $\nu \to 0$ (e.g. $B \to 0^+$) is equivalent to setting $\nu = 0$ but only using a *restricted ensemble* where microstates contributing to all other degenerate values of the average (e.g. $-M_S$ in the Ising example above) are excluded thus allowing the symmetry of the average of the observable in question to deviate from the one exhibited by the system as a whole. The two limits $\nu \to 0$ and $N \to \infty$ at the same time thus require the definition of a new probability distribution where excluded states are

given zero weight [86]. For rigorous mathematical arguments on symmetry breaking and the meaning of probability in an infinite system see [91].

From a dynamical point of view, the argument of the restricted ensemble is closely related to the ergodicity breaking discussed in the previous section, as a non-ergodic system evidently also fails to sample the entire phase space. Spontaneously broken symmetry can therefore be approached either by the method of "small fields" $\nu \to 0$ or by restricted ensembles and ergodicity breaking [86].

Order Parameter

A phase transition connected to spontaneous symmetry breaking can be described by an order parameter whose (quasi) average vanishes on one side of the transition while it is finite on the other. The order parameter for magnetic order that is relevant here is the magnetization per site

$$m_{\mathbf{q}}^{\alpha} = \frac{1}{L} \langle S_{\mathbf{q}}^{\alpha} \rangle \, , \tag{4.84}$$

which is just the average over

$$S_{\mathbf{q}}^{\alpha} = \sum_i e^{i\mathbf{q} \cdot \mathbf{x}_i} S_i^{\alpha} \, , \tag{4.85}$$

where $\mathbf{q}$ is the ordering wave vector, e.g. $q = \pi$ for antiferromagnetic order, and $\alpha \in \{x, y, z\}$ labels the direction in space. Spontaneously broken symmetry, i.e. a non-vanishing quasi-average of Eq. (4.85), implies true long-range order in the correlation function

$$S^{\alpha\alpha}(\mathbf{q}) = \lim_{B \to 0^+} \frac{1}{NZ} \text{Tr} \left(e^{-\beta \mathcal{H}(B)} S_{\mathbf{q}}^{\alpha} S_{-\mathbf{q}}^{\alpha} \right) \tag{4.86}$$

i.e.

$$\lim_{N \to \infty} \left(\frac{1}{N} S_{\mathbf{q}}^{\alpha\alpha} \right) > 0 \, , \tag{4.87}$$

or, equivalently,

$$\lim_{|\mathbf{x}_i - \mathbf{x}_j| \to \infty} \lim_{N \to \infty} \langle \mathbf{S}_i \cdot \mathbf{S}_j \rangle \neq 0 \, , \tag{4.88}$$

where $|\mathbf{x}_i - \mathbf{x}_j|$ is the distance between sites i and j [92]. This is intuitively clear, since for long distances $\langle \mathbf{S}_i \cdot \mathbf{S}_j \rangle \to \langle \mathbf{S}_i \rangle \langle \mathbf{S}_j \rangle$ and the quasi average $\langle \mathbf{S}_i \rangle$ is only non-vanishing in case of broken symmetry. Note that Eqs. (4.87) and (4.88) can be applied similarly to any local order parameter O_i.

The previously mentioned Mermin-Wagner theorem rigorously proves there can be no spontaneous symmetry breaking (of a continuous symmetry) in one and two dimensions at finite temperatures [55], a result which is surprisingly general and can be applied to a myriad of different models and systems, see for example [89].

This has the consequence, that the antiferromagnetic and spiral phases in Fig. 3.3 cannot extend to

finite temperature and therefore no temperature dependent transitions as pictured for the dimerized phase in Fig. 4.25 are possible. Because the Mermin-Wagner theorem only forbids the breaking of a *continuous* symmetry, the only long range order that could possibly be observed is long range dimer order, which is connected to a *discrete* symmetry. The order parameter for the dimerized phase is

$$D_i \equiv \langle \mathbf{S}_i \cdot \mathbf{S}_{i+1} - \mathbf{S}_i \cdot \mathbf{S}_{i-1} \rangle . \tag{4.89}$$

Just as in the magnetic case, where long range order can be expressed as $\langle \mathbf{S}_i \rangle \neq 0$, long range dimer order is connected to $\langle D_i \rangle \neq 0$. These quantities are therefore the focus of the numerical results in Section 4.3.4.

4.3.3. Thermalization

The great achievement of statistical mechanics is the ability to describe the properties of a system without detailed knowledge of the microscopic behavior. Usually, keeping track of the trajectories of 10^{23} particles is not desired and would not add any more information than already given by the statistical perspective. But still, there must of course be a connection to the individual classical dynamics of the particles. The gap is bridged by the ergodic hypothesis shown in Eq. (4.20), which equates the long time dynamical average of an observable with its ensemble average. There are, however, requirements that must be met in order for the equality to apply. As the name states, the assumption is that only dynamical systems that after long enough periods of time cover the entire phase space, i.e. ergodic systems, can satisfy the ergodic hypothesis. But even when the ergodicity or non-ergodicity established, as was the focus of Section 4.2, the question remains what exactly is meant by *long-time* average. Naturally, the precise definition requires $t \to \infty$, but surely there are finite but long enough times that suffice to describe the average adequately well. Presumably, every ergodic system will eventually tend to some new equilibrium state. There are some exceptions, as mentioned in the beginning of Section 4.2, but generally this means that the dynamics must be chaotic. Once a new equilibrium is established, the system will merely fluctuate and the long time average cannot change significantly, even if the time is truly followed to infinity. The crux of the matter is therefore to determine when the system reaches such a new equilibrium, or, in other words, *thermalizes*. To do so precisely is not a trivial task, but there are certainly indications that point towards the thermalization of a dynamical state.

One of the hallmarks of chaotic motion is irreversibility. This is a key piece of the puzzle of how to connect deterministic equations of motion with statistical behavior and therefore the second law of thermodynamics. Important for this is the exponential sensitivity on perturbations as mentioned in Section 4.1.2. A new equilibrium state can therefore not depend on the specific initial conditions and can in fact be defined as just that. Concretely, when following the dynamics after a parameter quench, a system described with a certain energy E must yield the same average values of observables, no matter what the initial conditions for the perturbations were.

Fig. 4.27 shows three trajectories following three different quenches with different initial conditions but same $\Delta\varepsilon$ introduced into the system. From left to right, the observables shown in the three panels are:

- average nearest neighbor correlations

$$\langle C_i^{\mathrm{nn}} \rangle = \frac{1}{LS^2} \sum_i \mathbf{S}_i \cdot \mathbf{S}_{i+1} \tag{4.90}$$

- average dimerization order parameter

$$\langle D_i \rangle = \frac{1}{LS^2} \sum_i |\mathbf{S}_i \cdot (\mathbf{S}_{i+1} - \mathbf{S}_{i-1})| \tag{4.91}$$

- average spin-electron correlation

$$\langle C_i^{\mathrm{se}} \rangle = \frac{1}{L} \sum_i \mathbf{S}_i \cdot \langle \mathbf{s}_i \rangle \tag{4.92}$$
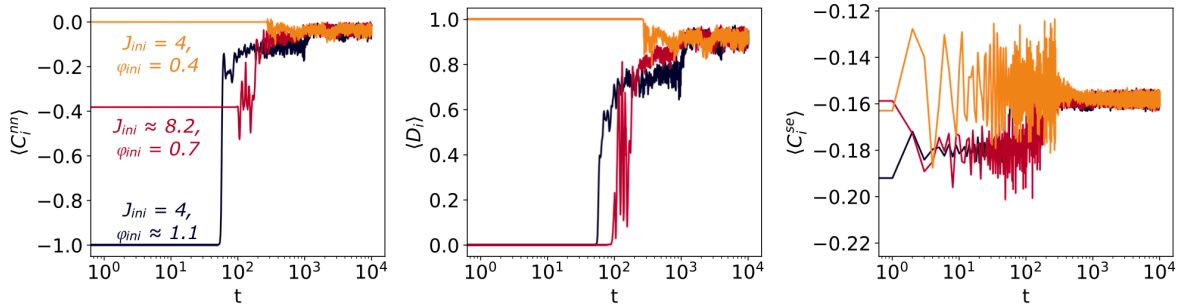

Figure 4.27.: Comparison of different quenches with the same energy of $\Delta\varepsilon \approx 0.08$ but different initial conditions for a system of size $L = 32$. The final state in all cases is $J_f = 4.0$, $\varphi_f = 0.7$. The pink line shows a J-quench with initial condition $J_{ini} \approx 8.2$, the blue and orange lines are φ-quenches with initial conditions $\varphi_{ini} \approx 1.1$ and $\varphi_{ini} = 0.4$, respectively. The three panels show, from left to right, the average nearest neighbor correlations $\langle C_i^{nn} \rangle$ defined in Eq. (4.90), the average dimerization order parameter defined in Eq. (4.91) and the average spin-electron correlation $\langle C_i^{se} \rangle$ defined in Eq. (4.92).

Evidently, for all observables, dynamics with the same $\Delta\varepsilon$ relax towards the same mean value independent of individual initial conditions. The relaxation happens rather quickly, within about $t \approx 1000$ time steps. For true statistical properties, however, the averages must be taken over even longer times to account for fluctuations. One indication that the time scales are long enough to witness true thermalization is the applicability of the central limit theorem from statistical mechanics. The central limit

theorem states that for an extensive thermodynamic variable

$$X = \sum_{i=1}^{N} X_i \tag{4.93}$$

with independent microvariables X_i the mean X/N follows a normal distribution. This in turn implies that for the standard deviation

$$\sigma_X = \sqrt{\langle X^2 \rangle - \langle X \rangle^2} \tag{4.94}$$

and the relative standard deviation $\sigma_X/\langle X \rangle$ the N-dependency is given by

$$\sigma_X = \mathcal{O}(\sqrt{N}) \quad \text{and} \quad \frac{\sigma_X}{\langle X \rangle} = \mathcal{O}\left(\frac{1}{\sqrt{N}}\right), \tag{4.95}$$

which in particular means $\sigma_X/\langle X \rangle \to 0$ for $N \to \infty$, i.e. (thermal) fluctuations around the mean value disappear in the thermodynamic limit.
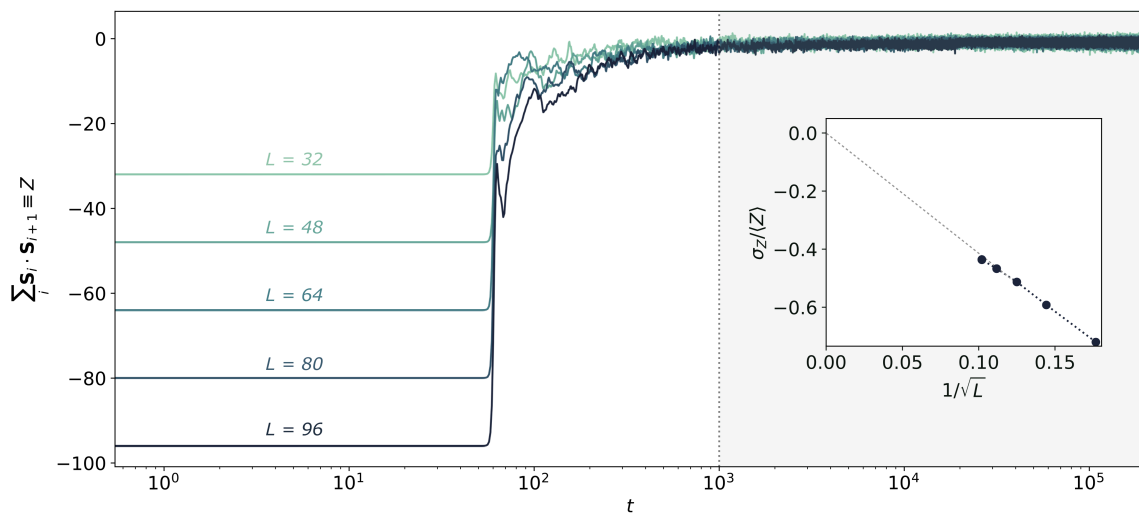

Figure 4.28.: The sum of nearest neighbor correlations (here abbreviated Z) as a function of time for different lattice sizes after a quench $\varphi = 0.3 \to 0.8$ at $J = 3$ (main figure) and relative standard deviation $\sigma_Z/\langle Z \rangle$ in the thermal regime, i.e. $t \approx 10^3 \to 10^5$ shaded in light green, as a function of $1/\sqrt{L}$ (inset). The dashed grey line in the inset extrapolates for $L \to \infty$, see discussion in text.

This is tested in Fig. 4.28, where the same φ-quench from $\varphi = 0.3 \to 0.8$ at $J = 3$ is repeated for $L = 32, 48, 64, 80$ and $L = 96$. The main figure shows the time evolution of the sum of nearest

neighbor correlations, here for simplicity abbreviated as

$$Z = \sum_i \mathbf{S}_i \cdot \mathbf{S}_{i+1} \,.$$

(4.96)

When averaged over $5 \cdot 10^4$ time steps, the inset of Fig. 4.28 shows the behavior of the relative standard deviation $\sigma_Z / \langle Z \rangle$ with the lattice size L. As required, the relative standard deviations goes to zero for $L \to \infty$ as indicated by the extrapolated dashed grey line, and is $\propto 1/\sqrt{L}$. This also implies, that for sufficiently large systems, the notion of *typicality* can be applied, i.e. one "typical" dynamical state displays the same properties as a state from an equilibrium statistical ensemble.

Note that for shorter times, the above considerations do not hold, true thermalization in the present context must therefore be considered realized at the earliest at $t \approx \mathcal{O}(10^4)$ or even $t \approx \mathcal{O}(10^5)$ depending on the particular case. This could also be the reason why the last data point with $L = 96$ does not quite align with the rest, a longer averaging time would be needed in this case.

One other thing that immediately catches the attention in Fig. 4.28 is the long time until the dynamics starts. Only after $t \approx 60$ time steps do the trajectories seem to leave the initial configuration. This is due to the in Section 4.1.2 mentioned fact, that initially, the classical spins are collinear to the electrons and the equations of motion yield $\dot{\mathbf{S}}_i = 0$. If the system is ergodic, however, it is exponentially sensitive to perturbations as discussed in Section 4.2, and therefore at some point will depart. Once the collinearity is destroyed, the equations of motion yield $\dot{\mathbf{S}}_i \neq 0$ and the dynamics start. As the following dynamics will all be ergodic, there is no further physical meaning to obtain from this initiation time and it will thus often be omitted from any following time dependent plots.

4.3.4. Emergence of Long Range Dimer Order

After the presentation of some theoretical background and terminology in the preceding sections, this one will now cover the main numerical results related to the dimerization in non-equilibrium. In order to test the existence of a dimerized phase that extends beyond zero temperature, the trajectory of the dimerization order parameter D_i will be traced after several parameter quenches into the dimerized phase. In particular, it will be investigated if and how the dimerization persists after a quench as a function of quench energy $\Delta \varepsilon$, that to some extent will play the role of "temperature". The ultimate aim is here to find the transition point between the disordered phase at high temperatures and a dimerized phase as shown in Fig. 4.25, and to determine whether or not the dimerized phase is stable above zero temperature at all. Of interest are also the timescales on which the system thermalizes. Another question is whether the semiclassical system, in contrast to mean-field theories, respects the Mermin-Wagner theorem [55]. The latter excludes spontaneously broken *continuous* symmetry, but makes no such statement regarding *discrete* symmetries. In order to be compliant with Mermin-Wagner, the system must therefore show the absence of long range magnetic order, but could possibly display long

range dimer order.

To focus the discussion, in the following the final state for all quenches into the dimerized phase will be fixed at $\varphi_f = 0.8$, $J_f = 3$. There are of course two possibilities to arrive at this point, starting in the antiferromagnetic phase and performing a φ-quench, as well as a J-quench from the spiral phase as sketched in Fig. 4.2 with ②. The dimerization transition that is searched for depends on the quench energy $\Delta\varepsilon$, before deciding which quenches are most suited for a systematic analysis, it is therefore necessary to inspect the $\Delta\varepsilon$-dependence of potential initial conditions. A similar analysis was already done for a final state within the antiferromagnetic phase in Section 4.2 in Fig. 4.5. The corresponding plot with $\varphi_f = 0.8$, $J_f = 3$ is shown in Fig. 4.29 for φ-quenches (left) and J-quenches (right) with the final state marked with a red dot in both cases.

Because of the peculiarity of 'quasi-adiabaticity' for φ-quenches within the antiferromagnetic phase already mentioned in Section 4.2.1, the φ-quenches from the antiferromagnetic phase into the dimerized phase are all very similar in energy. This can be seen in the left panel of Fig. 4.29, where the energy per lattice site introduced into the system $\Delta\varepsilon$ is plotted against initial condition φ_{ini} for $J = $ const.. Another observation is the discontinuity at the point of the AF-DIM equilibrium phase transition marked with a dashed line. This feature was also present in Fig. 4.5, where it was already observed that this feature originates in the final quench energy

$$E_f = \mathrm{Tr} \left[\boldsymbol{\rho}_0 \cdot \mathbf{t}'_{\mathrm{eff}} \right] , \qquad (4.97)$$

where the expectation value of the quenched effective hopping matrix $\mathbf{t}'_{\mathrm{eff}}$ is calculated in the state $\boldsymbol{\rho}_0$, both of which depend on the initial spin configuration.
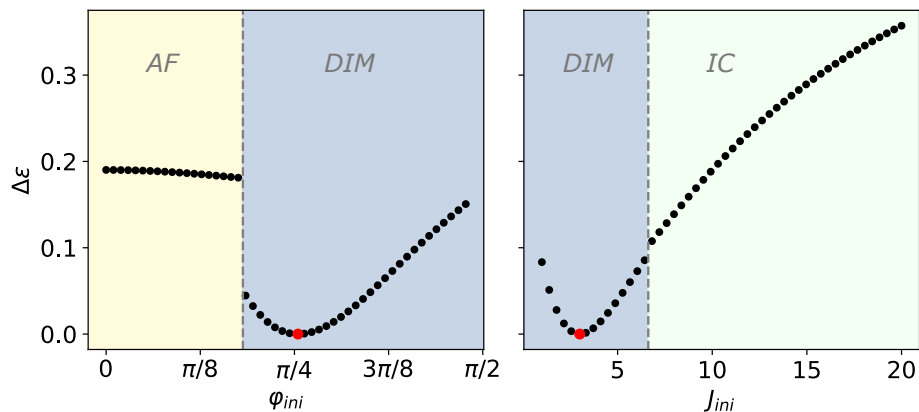

Figure 4.29.: Energy $\Delta\varepsilon = \Delta E / L$ of φ-quenches (left panel) and J-quenches (right panel) as a function of initial condition. Final state in all cases is ($\varphi = 0.8$, $J = 3.0$) as indicated by red dots. The grey dashed lines mark the boundaries between equilibrium phases.

Such a discontinuity can also be seen in the right panel, where the energy $\Delta\varepsilon$ of a J-quench into the dimerized phase is shown as a function of initial condition J_{ini} and $\varphi = $ const., at the point of the DIM-IC equilibrium phase transition again marked with a dashed line. In this case, however, the jump is considerably smaller, which might be due to the fact the here, neither phase exhibits a nearly flat dependence of $\Delta\varepsilon$ on J_{ini}, but follows the more expected behavior of a roughly continuous increase of $\Delta\varepsilon$ with increasing $\Delta J \equiv |J_{\mathrm{f}} - J_{\mathrm{ini}}|$. As opposed to the φ-quenches, where the range of $\Delta\varepsilon$ is limited by the range of possible φ-values as $\varphi \in (0, \pi/2)$, the energy induced by a J-quench seems to diverge for $J_{\mathrm{ini}} \to \infty$. All in all, the energy dependence of J-quenches seems to be better suited for a systematic investigation of the dimerization.

As introduced in Section 4.3.2, the presence or absence of long range order can be revealed by observing whether the real space correlation $\langle O_i O_j \rangle$ between any local order parameter O_i with $i, j \in (1, \ldots, L)$ goes to zero in the limit of long distances $|i - j| \to \infty$. Performing J-quenches of different energy $\Delta\varepsilon$, there seems to be indeed a qualitative difference in this behavior depending on the size of $\Delta\varepsilon$.

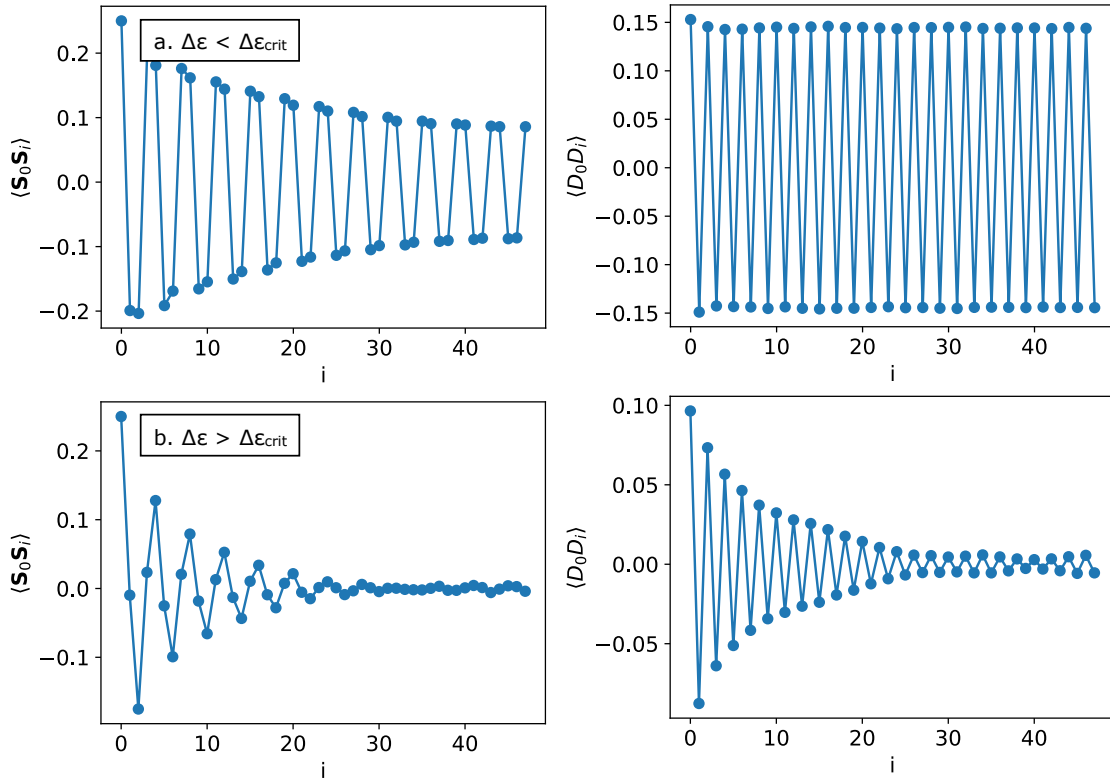

Figure 4.30.: Long time average of real-space correlations $\langle \mathbf{S}_i \mathbf{S}_j \rangle$ (Eq. (4.98)) and $\langle D_i D_j \rangle$ (Eq. (4.99)) for $i = 0$ (first site) as a function of distance for a system with $L = 96$ both below (top row) and above (bottom row) $\Delta\varepsilon_{crit}$. Because of periodic boundary conditions, the distance is only plotted until $L/2$.

To test for both magnetic and dimer long range order, Fig. 4.30 shows the long time average of the real space correlations between spins

$$\langle \mathbf{S}_i \mathbf{S}_j \rangle \equiv \frac{1}{t} \int_0^t \mathbf{S}_i(t') \cdot \mathbf{S}_j(t') \, \mathrm{d}t' \,, \tag{4.98}$$

as well as the correlations of the dimerization order parameter

$$\langle D_i D_j \rangle \equiv \frac{1}{t} \int_0^t D_i(t') \cdot D_j(t') \, \mathrm{d}t' \,, \tag{4.99}$$

which is defined as

$$D_i = \mathbf{S}_i \cdot (\mathbf{S}_{i+1} - \mathbf{S}_{i-1}) \,, \tag{4.100}$$

for two different J-quenches.

The top row shows a lower energy quench $\Delta\varepsilon \approx 0.38$ with spin correlations between spins on lattice sites 0 and i $\langle \mathbf{S}_0 \mathbf{S}_i \rangle$ on the left and dimer correlations $\langle D_0 D_i \rangle$ on the right as a function of distance i for a system with $L = 96$. In both cases, the long time average was taken over $t = 2 \cdot 10^5$ time steps. The spin correlations on the left can be seen to significantly decrease as a function of distance, whereas the dimer correlations on the right stay approximately constant throughout the entire lattice. Note that because of periodic boundary conditions, the longest possible distance is actually only $i = L/2$. The bottom row in Fig. 4.30 shows the same quantities after a quench with $\Delta\varepsilon \approx 0.44$ and reveals different behavior in both. The spin correlations $\langle \mathbf{S}_0 \mathbf{S}_i \rangle$ on the left drop to zero rather quickly. The dimer correlations $\langle D_0 D_i \rangle$ on the right are a little slower, but also go nearly to zero before reaching the maximum distance $L/2$. The difference in behavior between the top and bottom row suggests the presence of some critical energy $\Delta\varepsilon_{\mathrm{crit}}$ in between below which the system retains long range dimer order as seen in the top right panel of Fig. 4.30.

Unfortunately, however, the lattice is either too small or the averaged time not long enough to witness a truly zero spin correlation $\langle \mathbf{S}_0 \mathbf{S}_i \rangle$ for $i \to \infty$ in the top left panel of Fig. 4.30 below the critical energy $\Delta\varepsilon_{\mathrm{crit}}$. Instead of performing very time and memory intensive calculations of $\langle \mathbf{S}_0 \mathbf{S}_i \rangle$ with larger lattices for longer times, there is another indication that can be used for presence or absence of long range order that is more accessible. For large distances $|i - j| \to \infty$, any correlation between local observables $\langle O_i O_j \rangle$ is expected to separate into the individual components $\langle O_i \rangle \langle O_j \rangle$. In order to show the absence of long range magnetic order, it is therefore equivalent to show that $\langle \mathbf{S}_i \rangle \to 0$ for all $i \in (1, \ldots, L)$. In the same manner, the presence of long range dimer order would imply $\langle D_i \rangle \neq 0$.
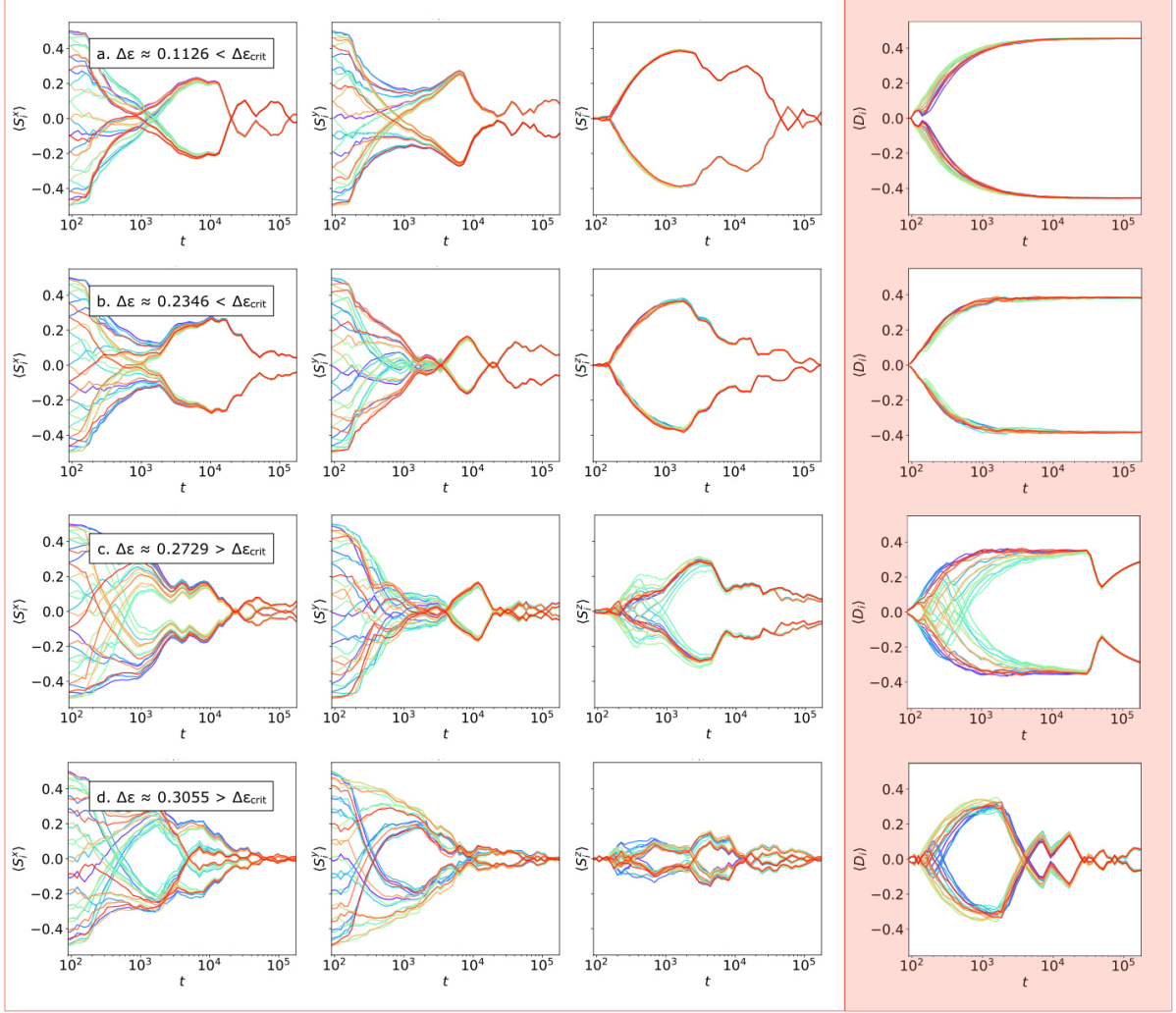
Figure 4.31.: Time averages of magnetic and dimer order parameter as defined in Eqs. (4.101) and (4.102) as a function of time for four J-quenches with different energies $\Delta\varepsilon$ (rows) for a lattice of size $L = 32$. The first three columns show the components of the magnetic order parameter $\langle S_i^\alpha \rangle$ with $\alpha = x, y, z$, the rightmost column shaded in red the dimerization order parameter $\langle D_i \rangle$. Each lattice site i is plotted separately as a different line. Final state is in all cases $J_f = 3$, $\varphi_f = 0.8 = $ const.

The corresponding time averages of magnetic and dimerization order parameter are defined as

$$\langle S_i^\alpha \rangle_t \equiv \frac{1}{t} \int_0^t S_i^\alpha(t') \, \mathrm{d}t', \quad \text{with} \quad \alpha \in \{x, y, z\}, \tag{4.101}$$

and

$$\langle D_i \rangle_t \equiv \frac{1}{t} \int_0^t D_i(t') \, \mathrm{d}t'. \tag{4.102}$$

A true *long time average* should of course not depend on t anymore. As the limit $t \to \infty$ might not be quite in reach within this theory, it is useful to analyze this dependence and perhaps extrapolate.

Fig. 4.31 shows $\langle S_i^\alpha \rangle_t$ and $\langle D_i \rangle_t$ as a function of time for four different J-quenches for a system with $L = 32$. The top row shows a quench from $J_{\mathrm{ini}} = 7$ to $J_{\mathrm{f}} = 3$ with quench energy $\Delta\varepsilon \approx 0.1126$. The components of the magnetic order parameter $\langle S_i^\alpha \rangle$ with $\alpha = x, y, z$ are plotted in the first three columns. The initial spin configuration at $J_{\mathrm{ini}} = 7, \varphi_{\mathrm{ini}} = 0.8$ is a spin spiral in the $x - y$ plane, as can be seen by the distribution of $\langle S_i^x \rangle$ and $\langle S_i^y \rangle$ for small times t. Note that as mentioned above, the initiation time discussed in Section 4.1.2, where the system stays in the initial configuration, is cut off, and all plots start at $t \approx 10^2$. The z-component $\langle S_i^z \rangle$ is zero at first, but then tends to zero again, as do the other two. None of them are completely converged at $t = 2 \cdot 10^5$, which is the last plotted time, but the oscillation is expected to decrease on very long time scales and yield $\langle S_i^\alpha \rangle = 0$ for $t \to \infty$. Striking is the apparent coherence between the spins at later times, as the lines that start apart eventually converge into almost two single oscillations. This is an indication of the *short range order*, that can of course be present even without long range order, and that apparently separates the lattice into two sublattices of roughly (short range) aligned spins. Finally, the rightmost column shows the time averaged dimerization order parameter $\langle D_i \rangle$ as a function of time. In the initial spiral configuration, it is $\langle D_i \rangle = 0$ for all i, but then continuously increases until it converges to either $\langle D_i \rangle \approx +0.45$ or $\langle D_i \rangle \approx -0.45$. A perfectly dimerized spin configuration with an exact $\uparrow\uparrow\downarrow\downarrow$-alignment would, with D_i as defined as in Eq. (4.100), alternate between $D_i = +0.5$ and $D_i = -0.5$, the converged time averages of the top row are therefore fairly close to the ground state configuration. Now it is also clear, that the components of $\langle S_i^\alpha \rangle$ seem to align into two different sublattices - one with a tendency to "$\uparrow$" the other "$\downarrow$".

The second row of Fig. 4.31 shows a quench with $J_{\mathrm{ini}} = 12$ to $J_{\mathrm{f}} = 3$ and $\Delta\varepsilon \approx 0.2346$. Qualitatively, the behavior of both $\langle S_i^\alpha \rangle$ and $\langle D_i \rangle$ is similar to the row above, with the components of $\langle S_i^\alpha \rangle$ oscillating towards zero and $\langle D_i \rangle$ converged, this time to a value slightly below 0.4. A very noticeable difference can be seen in the third row, where the quench is from $J_{\mathrm{ini}} = 14$ to $J_{\mathrm{f}} = 3$ with $\Delta\varepsilon \approx 0.2729$. The spin components $\langle S_i^\alpha \rangle$ still oscillate towards zero, but are now not nearly as aligned as in the two rows above, as can be seen by the multiple lines that are still present at larger times. The dimerization order parameter, after initially seeming to converge, breaks apart at around $t \approx 3 \cdot 10^4$. The observable time scale, however, is too short to determine with certainty whether $\langle D_i \rangle$ will eventually converge to zero.
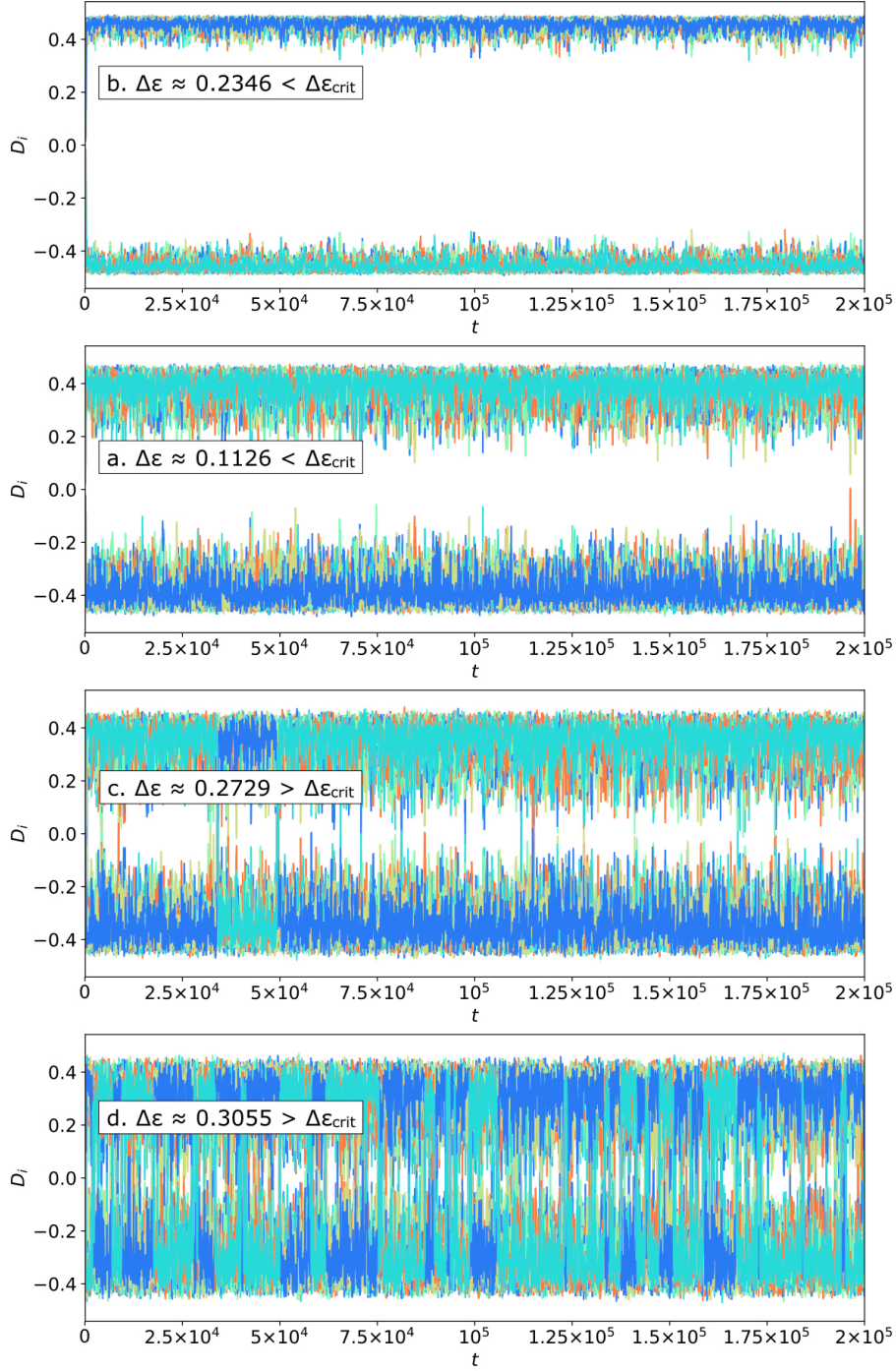
Figure 4.32.: Dimerization order parameter D_i plotted for each lattice site i for quenches with $J_{\mathrm{ini}} = 7, 12, 14$ and 16 (top to bottom row) and $J_{\mathrm{f}} = 3$ for $L = 32$ and $\varphi = 0.8$. For better visibility, each D_i was averaged over a moving window of $t = 100$ time steps to reduce the temporal fluctuations slightly.

This is more unambiguous in the last row, where the quench is taken from $J_{\text{ini}} = 16$ to $J_{\text{f}} = 3$ with $\Delta \varepsilon \approx 0.3055$. The dimerization parameter $\langle D_i \rangle$ also first rises, but then breaks off and starts oscillating around $\langle D_i \rangle = 0$ with increasingly smaller oscillation amplitude. The spin components $\langle S_i^\alpha \rangle$ are much more converged with the final value at $t = 2 \cdot 10^5$ around $\langle S_i^\alpha \rangle \approx \mathcal{O}(10^{-3})$ compared to $\langle S_i^\alpha \rangle \approx \mathcal{O}(10^{-2})$ in the top two rows. As indicated by the row labels, a tentative definition of *critical energy* $\Delta \varepsilon_{\text{crit}}$ is for now

$$
\begin{aligned}
\Delta \varepsilon < \Delta \varepsilon_{\text{crit}} &\Leftrightarrow \langle D_i \rangle = \text{converged} \neq 0 \quad \text{and} \\
\Delta \varepsilon > \Delta \varepsilon_{\text{crit}} &\Leftrightarrow \langle D_i \rangle \begin{cases} \text{not converged or} \\ \text{converged} = 0 \,, \end{cases}
\end{aligned}
\tag{4.103}
$$

where the Δ indicating the energy is *added* to the system by the quench is dropped for simplicity.

A more detailed plot of the individual dimerization parameter D_i without the long time average can be found in Fig. 4.32. The only average taken in this plot is a moving window average over $t = 100$ time steps to reduce the significant temporal fluctuations slightly and improve visibility. Shown are the same calculations as in Fig. 4.31 with $J_{\text{ini}} = 7, 12, 14, 16$ from top to bottom and energies as indicated. The first two rows, with $\Delta \varepsilon < \Delta \varepsilon_{\text{crit}}$, show that each D_i fluctuates with an amplitude that increases with $\Delta \varepsilon$ but otherwise stays constant. The third row reveals the origin of the kink in $\langle D_i \rangle$ that appears in the third row of Fig. 4.31 at around $t \approx 3 \cdot 10^4$, which appears to be caused by a temporary flip of the dimerization order. Simply speaking, this amounts to a shift from ... ↑↑↓↓↑↑ ... to ... ↓↑↑↓↓↑ and back, and could be seen as an unlikely macroscopic fluctuation close to the phase transition. In the bottom row, where the energy is well above $\Delta \varepsilon_{\text{crit}}$, this happens continuously, until each D_i covers nearly the entire value range randomly.

For a more systematic approach it is useful to determine collective order parameters that describe the behavior for all $i \in (1, \ldots, L)$. The order parameter for magnetic long range order, which needs to capture the behavior of all three components of the magnetic order parameter $\langle \mathbf{S}_i \rangle$, can therefore be defined as an average "length" of the thermalized spin

$$
O_M(t) \equiv \frac{1}{L} \sum_{i=1}^{L} \sqrt{\langle S_i^x \rangle_t^2 + \langle S_i^y \rangle_t^2 + \langle S_i^z \rangle_t^2} \,,
\tag{4.104}
$$

where the $\langle S_i^\alpha \rangle_t$ are the time averages as defined in Eq. (4.101), with the time t denoting the time over which the average is taken.

As the dimerization order parameter defined in Eq. (4.100) is already a scalar, there is no need to calculate an effective "length". There is, however, another subtlety to mind before averaging over the lattice. As mentioned above, a dimerized spin configuration consists of *alternating* values $D_i = \pm 0.5$,

an average is thus best defined as the average of the absolute value or a staggered average

$$O_D(t) \equiv \frac{1}{L}\sum_{i=1}^{L}(-1)^i \langle D_i \rangle_t \,,\tag{4.105}$$

where the overall sign is chosen such that $O_D > 0$ and again, $\langle D_i \rangle_t$ denotes the time average as defined in Eq. (4.102) as a function of averaging time t.
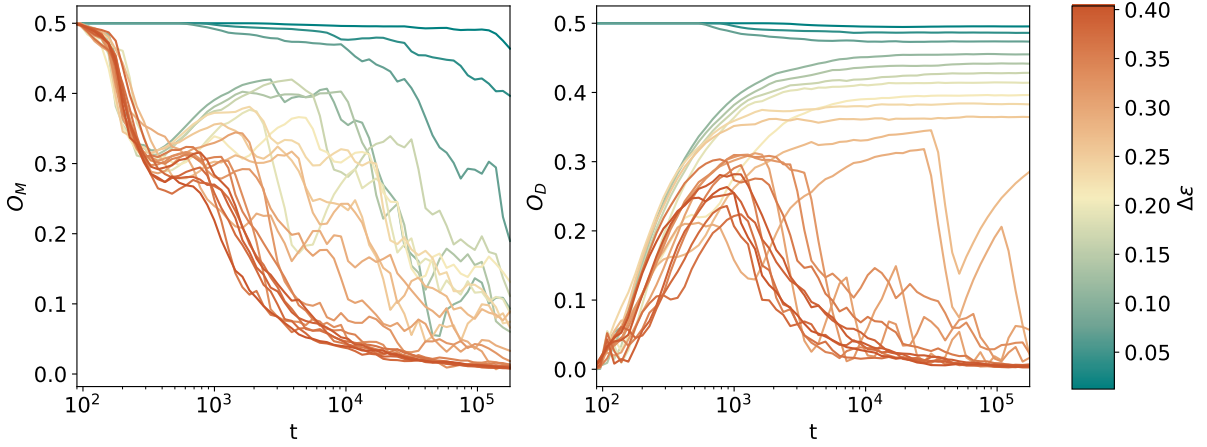

Figure 4.33.: Average magnetic (left panel) and dimerized (right panel) order parameter as defined in Eqs. (4.104) and (4.105), respectively, for quenches with different energies $\Delta\varepsilon$ as indicated by the colorbar for a lattice with $L = 32$. Blue-green indicates energies below the dimerization transition, orange-red above the dimerization transition and yellow those near it.

Fig. 4.33 shows $O_M(t)$ in the left panel and $O_D(t)$ in the right panel as a function of time for different J-quenches with $J_{\text{ini}} \in (4, \ldots, 25)$ and energies $\Delta\varepsilon$ as indicated by different colors according to the colorbar. Blue-green colored lines correspond to quenches with $\Delta\varepsilon < \Delta\varepsilon_{crit}$ orange-red colored lines to quenches with $\Delta\varepsilon > \Delta\varepsilon_{crit}$ and yellow lines to $\Delta\varepsilon \approx \Delta\varepsilon_{crit}$ with the critical dimerization energy $\Delta\varepsilon_{\text{crit}}$ as defined in Eq. (4.103). The magnetic order parameter O_M in the left panel suggests $O_M(t) \to 0$ for $t \to \infty$ in all cases, even though particularly the lower energy quenches are far from converged on observable time scales. Evidently the time scale of thermalization is hugely dependent on the energy $\Delta\varepsilon$ with the quenches above the dimerization transition $\Delta\varepsilon_{crit}$ decaying noticeably faster than the ones below.

The lowest energy quenches with $J_{\text{ini}} = 4, 5, 6$ start from within the dimerized phase as can be seen in the right panel of Fig. 4.33 as the dark green lines. In this case, the energy $\Delta\varepsilon$ added by the quench only leads to slightly decreased final value of O_D that seems perfectly converged on observable time scales. Increasing J_{ini} and therewith $\Delta\varepsilon$ shifts the initial spin configuration into the spiral phase with an initial $O_D(t=0) = 0$. The quenches with energy below the critical energy $\Delta\varepsilon_{\text{crit}}$ start to converge

around $t \approx \mathcal{O}(10^3)$ to a constant final value of O_D, which decreases with increasing energy $\Delta\varepsilon$. Those with energies close to and above $\Delta\varepsilon_{\mathrm{crit}}$, however, cannot really be said to display a definite convergence behavior. The higher energy quenches in red clearly tend to $O_D(t) \to 0$ for $t \to \infty$, but closer to the transition this cannot be said with certainty. Either the dimerization order parameter will eventually go to zero as well, just on very long time scales, or it will converge to another nonzero value below the already converged final values of O_D. The latter case would mean, of course, that these quenches are still technically *below* the critical energy if it was defined as a true transition energy between disordered and dimerized phase. The critical energy $\Delta\varepsilon_{\mathrm{crit}}$ as defined in Eq. (4.103) would then actually be a lower bound for the transition energy that is most probably higher in the infinite time limit.
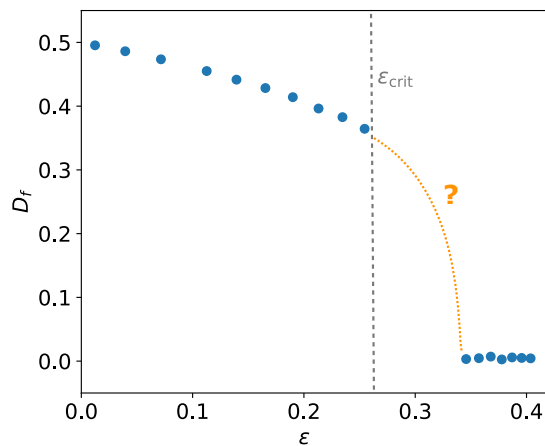

Figure 4.34.: Converged long time limit of the dimerization order parameter D_{f} as a function of quench energy $\Delta\varepsilon$. The critical energy $\Delta\varepsilon_{\mathrm{crit}}$ according to the tentative definition in Eq. (4.103) shown as a dashed grey line, denotes the boundary above which the dimerization order parameter O_D is either not converged or zero. The dotted orange line is a speculation for the infinite time limit $t \to \infty$.

This assumption is substantiated when the converged values of O_D are plotted as a function of energy. Let

$$D_{\mathrm{f}} \equiv \lim_{t\to\infty} O_D(t) \tag{4.106}$$

denote the final, converged value of the dimerization order parameter O_D. Fig. 4.34 shows D_{f} as a function of quench energy $\Delta\varepsilon$ for the same calculations shown in Fig. 4.33. It smoothly decreases from the maximum value of $D_{\mathrm{f}} = 0.5$ until the convergence boundary $\Delta\varepsilon_{\mathrm{crit}}$ marked with a dashed grey line is hit at $D_{\mathrm{f}} \approx 0.35$. For larger energies $\Delta\varepsilon$, where the lines in Fig. 4.33 are converged, $D_{\mathrm{f}} = 0$ can be safely assumed, so these points are included in Fig. 4.34. For all quenches with energies in between, however, there cannot be a certainty on whether the final value will tend to $D_{\mathrm{f}} \to 0$ and lead to a discontinuous transition, or some other nonzero value which could lead to a continuous transition

as sketched with an orange dotted line. Note the similarity to the magnetization as a function of temperature in panel c. of Fig. 4.26 in the Ising model. As thermal phase transitions are usually, but not always, of second order, i.e. continuous phase transitions, the latter case seems more likely. This cannot be decided using the present method, however, as the accessible time scales are far too low.
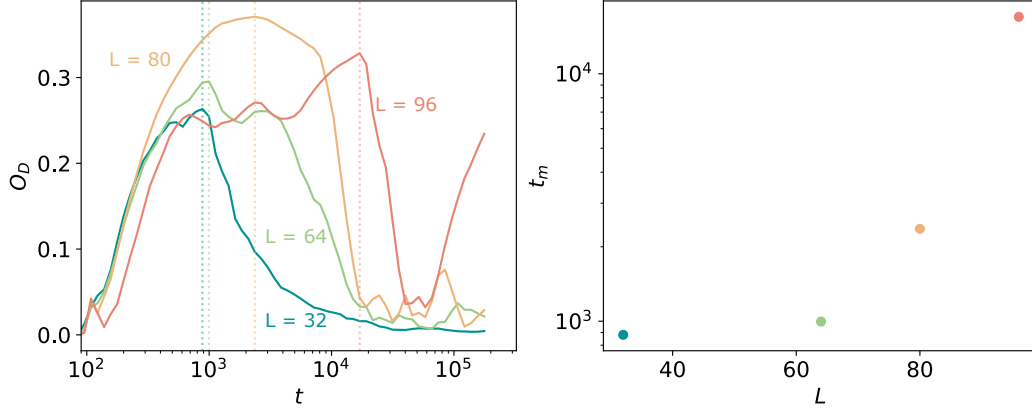

Figure 4.35.: Left panel: dimerization order parameter $O_D(t)$ (as defined in Eq. (4.105)) for a J-quench with $\Delta \varepsilon \approx 0.404$ for different lattice sizes as indicated. Right panel: time at which the maximum of O_D is reached as a function of lattice size L, also plotted in the left panel as a dotted line in the corresponding color.

One important aspect that has not yet been mentioned in this section, is of course the thermodynamic limit $L \to \infty$. As introduced in Sections 4.3.1 and 4.3.2, strictly speaking there are no phase transitions and no spontaneous symmetry breaking in finite systems. It cannot, however, be denied, that large but finite systems often yield adequate results with respect to such phenomena, after all, "real" material samples are also finite and still exhibit for example ferromagnetic order. There are several approaches to reconcile spontaneous symmetry breaking in finite systems. One assumption is, that while the system as a whole cannot exhibit a symmetry broken, long range ordered state, it still can spend long times in such a state [94].

The left panel of Fig. 4.35 shows the dimerization order parameter O_D as a function of time, as defined in Eq. (4.105), after a quench with the same energy of $\Delta \varepsilon \approx 0.404$ above the critical energy $\Delta \varepsilon_{\mathrm{crit}}$ for different lattice sizes L as indicated. The time at which the maximum value is reached and the order parameter starts to break down is marked with a dotted line in the individual colors. The dependence of this time t_m is then shown in the right panel as a function of lattice size L. Evidently, a quench with the same energy $\Delta \varepsilon$ seems to lead to a quicker decrease of O_D for smaller lattice sizes. Some authors have found a transition period $\propto \exp(\sqrt{L})$ between the degenerate symmetry broken states [95,96], but here there are not enough data points and too low time scales to conclude a definite dependence

of the "lifetime" of the symmetry broken dimerized phase as a function of lattice size.
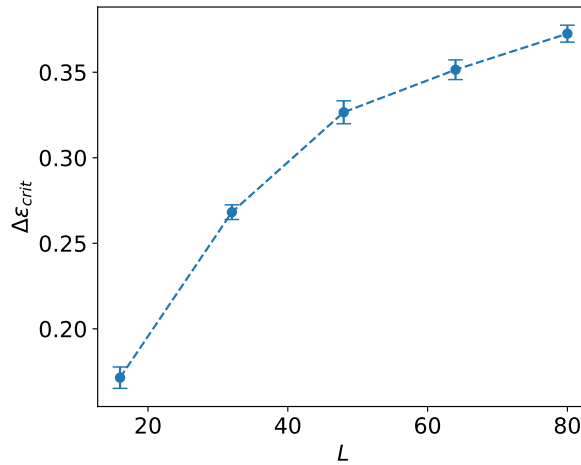

Figure 4.36.: Critical dimerization energy $\Delta\varepsilon_{\text{crit}}$ as a function of lattice size L. Upper error bar denotes the first $\Delta\varepsilon$ at which the dimerization parameter O_D is not converged, lower error bar the last $\Delta\varepsilon$ at which O_D is converged to a nonzero value.

Another indication of possibly longer stability of the dimerized phase for larger lattice sizes is the critical energy $\Delta\varepsilon_{\text{crit}}$ below which the dimerization parameter O_D is converged to a nonzero value on observable time scales. Fig. 4.36 shows $\Delta\varepsilon_{\text{crit}}$ as a function of lattice size L. The error bars are meant as a region of uncertainty, the location of the upper error bar denotes the first $\Delta\varepsilon$ at which O_D is not converged, the lower error bar the last $\Delta\varepsilon$ for which it is converged to $D_f \neq 0$. As discussed above, some of the calculations above the error bar are far from converged and could in theory still thermalize to a value $D_f \neq 0$. This means that the critical energy plotted here simply stands for the energy below which dimerization is very likely present. Evidently, $\Delta\varepsilon_{\text{crit}}$ increases with increasing lattice size. The slope decreases with increasing L, suggesting there might be a limit that will be approached in the thermodynamic limit.

As a consistency check, there will now be a short discussion of a few results for a quench into the antiferromagnetic phase. Section 4.2 was concerned with quenches within the antiferromagnetic phase, and Fig. 4.5 showed the quench energies $\Delta\varepsilon$ as a function of initial condition $\varphi_{\text{ini}}, J_{\text{ini}}$ for a final state $\varphi_f = 0.4, J_f = 3$. It was shown that J-quenches within the antiferromagnetic phase do not result in ergodic behavior unless the energy is sufficiently high, and even then the dynamics were merely weakly chaotic. φ-quenches from the dimerized into the antiferromagnetic phase show a steeper increase in $\Delta\varepsilon$.

The response of the system to a quench into the antiferromagnetic phase will here be demonstrated by the example of three φ-quenches with $\varphi_{\text{ini}} = 0.6, 0.8, 1.2$ and final state $\varphi_f = 0.4, J_f = 3$. Fig. 4.37

shows again the magnetic and dimer order parameter O_M and O_D as defined above in Eqs. (4.104) and (4.105), respectively. The left panel shows O_M as a function of time for the three different quenches with energies as indicated. The largest quench $\varphi = 1.2 \to 0.4$ shown in dark red shows a longer initiation time compared with the other two quenches, but then drops to zero rather quickly. The smallest quench $\varphi = 0.6 \to 0.4$ on the other hand, shows a quicker start of the dynamics but then the order parameter starts to fluctuate with a slow frequency and an increasing tendency to zero. A similarly slow convergence of the magnetic order parameter to zero could be witnessed above for the quenches into the dimerized phase, when the energy $\Delta\varepsilon$ was low. The same difference in initiation time between the quenches of different energies can also be seen in the right panel of Fig. 4.37 where the dimer order parameter O_D is shown as a function of time for the same quenches. In this case, however, there are nearly no fluctuations at all and all quenches result in a quick convergence to $D_f = 0$. The antiferromagnetic phase therefore shows no indications of either magnetic or dimerized long range order at any energy scales.
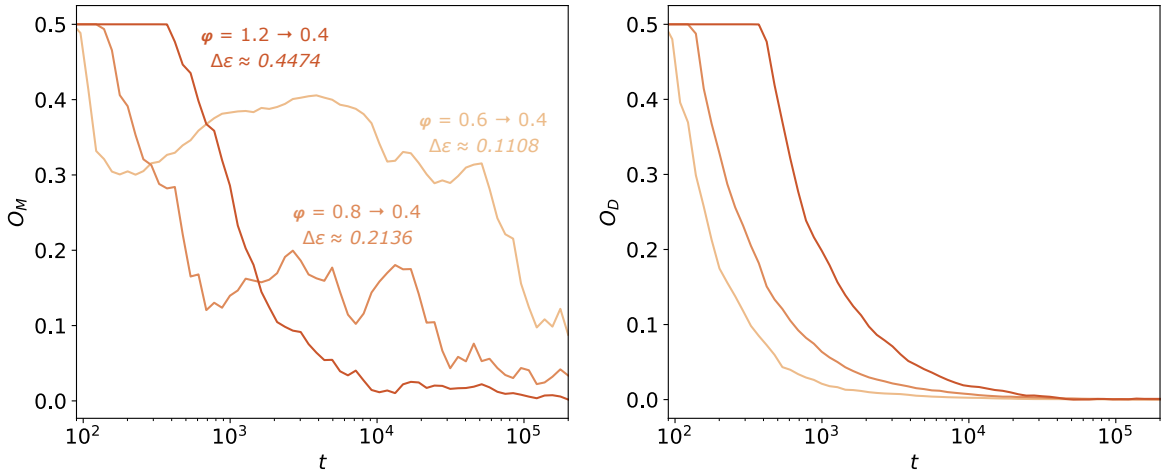

Figure 4.37.: Magnetic and dimer order parameter as a function of time for φ-quenches with $\varphi_{ini} = 1.2, 0.8, 0.6$ from the dimerized into the antiferromagnetic phase with different energies $\Delta\varepsilon$ as indicated. The final state in all cases is $\varphi_f = 0.4, J_f = 3$ with $L = 32$.

In conclusion, some questions posed at the beginning of this section can now be answered. One of these questions concerned the presence or absence of long range dimer order. The Mermin-Wagner theorem, that forbids spontaneous symmetry breaking of a continuous symmetry above $T = 0$ is respected within this semiclassical framework. For both quenches into the dimerized phase and into the antiferromagnetic phase, the long time average of the order parameter of long range magnetic order $\langle \mathbf{S}_i \rangle$ goes to zero in the long time limit. This underlines the difference to mean field theories, which in the equilibrium framework do look similar to this semi-classical viewpoint. Note that a mean

field theory *would* wrongly predict long range order even for $T > 0$.

The Mermin-Wagner theorem only makes predictions about the breaking of a continuous symmetry. The symmetry connected with the dimerization order parameter is, however, discrete. A long range *dimer* order is thus in principle possible. Below a certain critical energy, the long time average of the dimerization order parameter $\langle D_i \rangle$ is indeed found to converge to a finite value. With increasing energy, there is initially a regime where $\langle D_i \rangle$ is not converged at all on observable time scales, followed by $\langle D_i \rangle \to 0$ for very large energies $\Delta \varepsilon$. The shape of the final, converged value $D_f(\Delta \varepsilon)$ is reminiscent of a second order phase transition like the magnetization of a ferromagnet $M(T)$, even though $\Delta \varepsilon$ is of course not a *real* temperature, but only related to it in an unknown manner. Because of missing convergence in the vicinity of $\Delta \varepsilon_{\text{crit}}$, critical exponents cannot be calculated here, although this should in principle be possible with much larger lattice sizes and longer times.

There is no long range order for $T > 0$ in the one dimensional Ising model as is well known and shown heuristically in Section 4.3.2. The argument only uses the fact that domain walls can be created. This could therefore also apply to the dimerized phase although a detailed analytical consideration of this specific case will not be given here. Technically, even though the numerical results show a tendency towards a stable long range dimer order at $L \to \infty$, this could very well not be the case after all. The lattice sizes shown here are still too small to show this effect, however, as the entropy of the domain wall state increases only with $\propto \log N$. It therefore cannot be decided here and would require further investigations.

Another question posed in the beginning of this section was about the speed of thermalization. Numerical results imply that here, the time scales for thermalization are rather long, unless the energy $\Delta \varepsilon$ is very large. For both the quench into the dimerized and into the antiferromagnetic phase, $\langle \mathbf{S}_i \rangle$ is especially slow to thermalize. The dimerization order parameter $\langle D_i \rangle$, however, converges rather quickly to zero after a quench into the antiferromagnetic phase, regardless of energy. A quench into the dimerized phase results either in a rather fast thermalization to a finite value below the critical energy, a much more slow convergence close to but above the critical energy, or a quicker thermalization to $\langle D_i \rangle \to 0$ well above the critical energy.

5. Conclusions, Summary and Perspectives

This thesis covers many aspects of the Kondo lattice model with classical spins on the zigzag ladder both in equilibrium and beyond. One of the central results is the discovery of a novel dimerized phase. In the equilibrium part of this thesis, both strong and weak coupling perturbation theory were found to agree well with the results, but fail to explain the dimerized phase. Hence, this seems to be a nonperturbative effect.

DMRG calculations by Matthias Peschke found a similar phase in the fully quantum mechanical Kondo model [20,21]. Although the quantum mechanical and semiclassical phase diagram share many similarities, there are notable differences. Quantum fluctuations destroy any long range order associated with an order parameter that does not commute with the Hamiltonian in the ground state of the quantum mechanical system and only allow the distinction between different kinds of short range order - here spiral or antiferromagnetic - whereas the classical model variant, lacking both quantum and thermal fluctuations at $T = 0$, does feature true long range order. In addition, there is a purely quantum mechanical phase that has no classical analogue, found *within* the dimerized phase in the DMRG phase diagram. This is a quasi-long-range spiral with a peak at $Q = \pi/2$ in the spin-structure factor.

In summary, the equilibrium phase diagram on the zigzag ladder is very rich and includes a novel dimerized phase that in both the quantum and classical case can be seen as a way of alleviating the frustration. This alleviation seems to pave the way for magnetic quasi-long-range order in the quantum mechanical model. While the quantum mechanical model still leaves some open questions - apart from perhaps employing higher order perturbative approaches to capture the dimerization after all - the semiclassical phase diagram is more or less understood.

The knowledge of the equilibrium phase diagram is then used in the next part of this thesis, where several non-equilibrium phenomena following parameter quenches are analyzed in detail. The first finding is the existence of a non-ergodic regime. For lattices of finite size and at low energies, a *threshold of ergodicity* is found. Below a certain critical energy E_{crit}, there is no observable dynamics besides a weak longitudinal fluctuation of the local magnetic moment in the electronic system $\langle \mathbf{s}_i \rangle_t$. Even above but close to this threshold, the classical spins $\mathbf{S}_i(t)$ stay more or less aligned in the axis of the initial configurations for considerably long times. It can therefore be said that the staggered magnetization per site $\mathbf{m}_\text{s}$ becomes an *emergent (approximate) conserved quantity*. The lack of ergodicity in the low energy regime is known from classical mechanics in research connected to the so-called *FPU-problem*

and the *KAM theorem*. There, in short, it is the proximity to an integrable model that results in regular dynamics even in a non-integrable model. In the search for such an integrable model, the $J_1 - J_2$-Heisenberg model proves to be integrable at least in the limiting case $J_1 = J_2$ and $L \leq 6$. But even though the Kondo lattice was found to map exactly onto this effective spin-only model for $J \to \infty$ in equilibrium, the connection is lost in non-equilibrium.

There is, however, another approach that yields a plausible integrable model. By linearizing the equations of motion analogous to standard spin-wave theory a spectrum of magnon-like excitations is found. The solution to the linearized equations of motion is found to agree qualitatively with the solution of the full problem. In addition, the finite size gap between the zero mode $\omega = 0$ and the first spin-wave excitation with $\omega \neq 0$ can serve as an explanation of the ergodicity threshold for finite lattices. In the thermodynamic limit $L \to \infty$, any arbitrarily small energy results in excitations, whose number diverges in one and two dimensions and which over time destroy the initial long range order. In a finite system, however, the excitation spectrum is not continuous but rather a collection of discrete values. The initial excitation energy is thus not arbitrarily small as in the thermodynamic limit, but displays a finite size gap, which is found to agree qualitatively with the critical energy E_{crit}. As the system is finite, the number of excitations does not *truly* diverge, which is why even above the threshold the system is only weakly ergodic. Even though in principle, the ergodicity threshold could be classified as a finite size effect, the weakly ergodic regime with nearly conserved $\mathbf{m}_{\text{s}}$ persists for numerically large lattices and extremely long propagation times.

The second result concerning the real-time dynamics considers parameter quenches well above the ergodicity threshold. Starting with an initial spin configuration within the spiral phase and then quenching the coupling constant J to a value within the dimerized phase, it can be observed that long range magnetic spiral order is destroyed over time and long range dimer order appears, if the quench energy $\Delta \varepsilon$ is small enough. Increasing the size of the J-quench and thus the energy, the dimer order eventually breaks down. Even though the dimerization order parameter O_D decreases continuously with increasing energy and therefore suggests a second order phase transition, the exact trend cannot be determined because of poor convergence close to the transition energy $\Delta \varepsilon_{\text{crit}}$ between dimerized and disordered phase. In addition, the relation between $\Delta \varepsilon$ and temperature T is unknown, and therefore no true $O_D(T)$ dependence can be established here. For both $L \to \infty$ and $t \to \infty$ critical exponents are in principle expected to be in reach to the numerical analysis based on real-time dynamics rather than on ensemble averages. Much larger system sizes than accessible here are also needed for results closer to the actual transition point and for a true finite size scaling of the dimerization transition. It should also be noted that the comparatively simple ansatz with only two parameters θ and $\Delta\theta$ for describing ground state spin configurations to derive the equilibrium phase diagram seems to be confirmed, as only those $\theta, \Delta\theta$-states are produced in the thermalization process.

While the results here certainly stand on their own, further avenues of research are still open. As much

of the discussion here covered the effects of a finite system size, the most obvious extension would be to extend the analysis to even larger systems. Substantially larger systems, however, can with this method only really be feasible with more advanced computing technology, i.e. more parallelization and perhaps the use of GPU computing also for the non-equilibrium results. The same evidently holds true for longer propagation times. As the main part of the time propagation contains a matrix multiplication, the computational effort scales, depending on the algorithm used, from at worst L^3 for a naive implementation to at best L^2, which is a lower bound for numerical matrix multiplication. The results in this thesis have been calculated using GPU computing for equilibrium and regular multi-core CPU parallelization for non-equilibrium calculations, with the latter running for one to several days on standard CPUs depending on the number of cores used.

Next to the technical aspects, there are also many more possibilities of further physically interesting research. All results here have been obtained for a half-filled electron band. It would be interesting to discover both a new equilibrium phase diagram as well as non-equilibrium properties of the system away from half-filling. The focus within this thesis has been very much on the classical spins, there might be still interesting phenomena left to learn about the electronic system. Another straightforward extension is also the generalization to other lattice geometries, in particular other frustrated ones such as the triangular lattice. Spin-charge coupled systems, frustrated spin models and non-equilibrium many-body systems are all research topics that will undoubtedly continue to produce compelling research in the future.

Many of the questions posed in the beginning are much too large to be answered by a single work, but still there are insights to be gained from this thesis which hope to add another piece to the puzzle. In particular, the results presented here are another indication that equilibrium statistical properties *can* be observed even in systems of relatively small size. Indispensable for the thermalization of the system, however, is overcoming an energy threshold which separates a static region from the ergodic regime. The time scales to observe the equilibrium necessary to connect to statistical mechanics are rather long, yet still accessible within this semiclassical framework, and actually only in the semiclassical setup. Studying similar questions for the case of a quantum-spin model appears completely out of reach in the foreseeable future, even though a speedup of thermalization due to quantum fluctuations is to be expected.

A. Heisenberg $J_1 - J_2$ Model on a Zigzag Ladder

This section is a small excursion on the Heisenberg $J_1 - J_2$-model on a zigzag ladder with classical spins. The goal here will be to derive the ground state energy and spin configuration. The Hamiltonian of the system is

$$H = \sum_{ij} J_{ij} \mathbf{S}_i \cdot \mathbf{S}_j \, , \tag{A.1}$$

where J_{ij} is the coupling constant between spins. As pictured in Fig. A.1, on the zigzag ladder, $J_{ij} = J_1$ between nearest and $J_{ij} = J_2$ between next-to-nearest neighbors, i.e. rungs and legs of the zigzag ladder. The energy of the system is then

$$E = J_1 \sum_{nn} \langle \mathbf{S}_i \mathbf{S}_j \rangle + J_2 \sum_{nnn} \langle \mathbf{S}_i \mathbf{S}_j \rangle \tag{A.2}$$

where, as $\mathbf{S}_i$ are just classical angular momentum vectors, $\langle \mathbf{S}_i \mathbf{S}_j \rangle = |\mathbf{S}|^2 \cos \alpha$ with $\alpha = $ (angle between $\mathbf{S}_i, \ \mathbf{S}_j$).
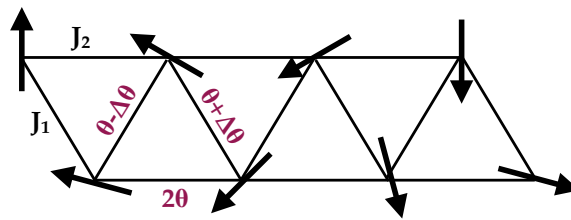

Figure A.1.: Heisenberg model on a zigzag ladder. Coupling between nearest neighbors J_1, between next to nearest neighbors J_2. Shown in red are the angles between neighboring spins, $\theta \pm \Delta\theta$ on the rungs and 2θ on the legs of the ladder, or, equivalently, nearest and next-to-nearest neighbors, respectively.

Using the parameterization of angles between nearest and next to nearest neighbors as shown in

Fig. A.1, Eq. (A.2) becomes

$$E(\theta, \Delta\theta) = L\,S^2 \left(\frac{1}{2} J_1 \cos\left(\theta + \Delta\theta\right) + \frac{1}{2} J_1 \cos\left(\theta - \Delta\theta\right) + J_2 \cos 2\theta \right)$$
$$= L\,S^2 \left(J_1 \cos\theta \cos\Delta\theta + J_2 \cos 2\theta \right)$$

(A.3)

where in the last line $\cos\left(x \pm y\right) = \cos x \cos y \mp \sin x \sin y$ was used.

The ground state energy, i.e. the minimal energy with respect to $(\theta, \Delta\theta)$, can be found by simple derivation.

Both $\partial E / \partial \theta$ and $\partial E / \partial \Delta\theta$ need to vanish, i.e.

$$\frac{\partial E(\theta, \Delta\theta)}{\partial\theta} = L\,S^2 \left(-J_1 \sin\theta \cos\Delta\theta - 2J_2 \sin 2\theta \right)$$
$$= L\,S^2 \left(-J_1 \sin\theta \cos\Delta\theta - 4J_2 \sin\theta \cos\theta \right)$$
$$= -L\,S^2 \sin\theta \left(J_1 \cos\Delta\theta + 4J_2 \cos\theta \right) \overset{!}{=} 0,$$

where $\sin 2x = 2\sin x \cos x$ was used, and

$$\frac{\partial E(\theta, \Delta\theta)}{\partial\Delta\theta} = -L\,S^2 J_1 \cos\theta \sin\Delta\theta \overset{!}{=} 0. \tag{A.4}$$

Eq. (A.4) is satisfied if either

$$\sin\theta = 0 \qquad \text{or}$$
$$J_1 \cos\Delta\theta + 4J_2 \cos\theta = 0, \tag{A.5}$$

yielding the two conditions

$$\theta = n\pi \quad (n \in \mathbb{N}), \quad \Delta\theta = \text{arbitrary}$$
$$\cos\theta = -\frac{J_1}{4J_2} \cos\Delta\theta \tag{A.6}$$

The first condition plugged into Eq. (A.4) gives

$$\frac{\partial E}{\partial\Delta\theta} = \pm L\,S^2 J_1 \sin\Delta\theta \overset{!}{=} 0, \tag{A.7}$$

which is satisfied for $\Delta\theta = n\pi$ $(n \in \mathbb{N})$. One solution $(\theta, \Delta\theta)$ to give an extremum of $E(\theta, \Delta\theta)$ is therefore

$$(\theta = n\pi, \quad \Delta\theta = m\pi), \quad \text{with} \quad n, m \in \mathbb{N}. \tag{A.8}$$

Plugging the second condition in Eq. (A.6) into Eq. (A.4) gives

$$\frac{\partial E}{\partial \Delta\theta} = L\,S^2 \frac{J_1^2}{4J_2} \cos\Delta\theta \sin\Delta\theta \stackrel{!}{=} 0\,, \tag{A.9}$$

which is satisfied for both $\Delta\theta = n\pi$ and $\Delta\theta = n\pi/2$ ($n \in \mathbb{N}$). For the second line in Eq. (A.6) follows therefore

$$\cos\theta = \begin{cases} \pm J_1/4J_2, & \text{for} \quad \Delta\theta = n\pi \\ 0, & \text{for} \quad \Delta\theta = n\pi/2\,. \end{cases} \tag{A.10}$$

From this, two more solutions $(\theta, \Delta\theta)$ that give an extremum of $E(\theta, \Delta\theta)$ are found:

$$\left(\theta = \arccos\left(\pm\frac{J_1}{4J_2} \right), \quad \Delta\theta = n\pi \right) \quad \text{and}$$
$$\left(\theta = n\frac{\pi}{2}, \quad \Delta\theta = m\frac{\pi}{2} \right), \quad n, m \in \mathbb{N}\,. \tag{A.11}$$

There are thus all in all three solutions that satisfy both $\partial E/\partial\theta = 0$ and $\partial E/\partial\Delta\theta = 0$, given by Eq. (A.8) and Eq. (A.11). To further analyse whether these points are in fact minima or maxima, the Hessian matrix

$$H_E(\theta, \Delta\theta) = \begin{pmatrix} \frac{\partial^2 E}{\partial\theta^2} & \frac{\partial^2 E}{\partial\theta\partial\Delta\theta} \\ \frac{\partial^2 E}{\partial\Delta\theta\partial\theta} & \frac{\partial^2 E}{\partial\Delta\theta^2} \end{pmatrix} \tag{A.12}$$

is needed, where the second derivatives are

$$\frac{\partial^2 E}{\partial\theta^2} = -L\,S^2 (J_1 \cos\theta \cos\Delta\theta + 4J_2 \cos 2\theta)$$
$$\frac{\partial^2 E}{\partial\Delta\theta^2} = -L\,S^2 J_1 \cos\theta \cos\Delta\theta \tag{A.13}$$
$$\frac{\partial^2 E}{\partial\Delta\theta\partial\theta} = \frac{\partial^2 E}{\partial\theta\partial\Delta\theta} = L\,S^2 J_1 \sin\Delta\theta \sin\theta\,.$$

The first solution in Eq. (A.8) gives

$$H_E(\theta = n\pi, \Delta\theta = m\pi) = LS^2 \begin{pmatrix} \pm J_1 - 4J_2 & 0 \\ 0 & \pm J_1 \end{pmatrix}\,. \tag{A.14}$$

For a minimum, the Hessian matrix needs to be positive definite. Given that $J_1, J_2 > 0$, this implies that

$\cos\theta\cos\Delta\theta \equiv -1$ and therefore either $(\theta = \pi, \Delta\theta = 0)$ or $(\theta = 0, \Delta\theta = \pi)$, both of which describe the same spin configuration - an antiferromagnet along the rungs. Furthermore, from $J_1 - 4J_2 > 0$ follows the additional condition $J_1 > 4J_2$.

For the first line in Eq. (A.11), the off-diagonal elements of the Hessian matrix vanish again. The matrix positive definite and the solution therefore a minimum if

$$
\begin{aligned}
\frac{\partial^2}{\partial\theta^2} & E\left(\theta = \arccos(-J_1/4J_2),\ \Delta\theta = 0\right) \\
&= -LS^2\left[-\frac{J_1^2}{4J_2} + 4J_2\left(2\frac{J_1^2}{4^2 J_2^2} - 1\right)\right] \\
&= -LS^2\left[-\frac{J_1^2}{4J_2} + 2\frac{J_1^2}{4J_2} - 4J_2\right] \\
&= -LS^2\left[\frac{J_1^2}{4J_2} - 4J_2\right] > 0 \quad\text{and} \\
\frac{\partial^2}{\partial\Delta\theta^2} & E\left(\theta = \arccos(-J_1/4J_2),\ \Delta\theta = 0\right) \\
&= LS^2\frac{J_1^2}{4J_2} > 0 \,,
\end{aligned}
$$

where $\cos 2x = 2\cos^2 x - 1$ was used in the first line. The solution is therefore a minimum if $J_1 < 4J_2$.

Finally, the second line in Eq. (A.11) gives

$$
H_E(\theta = \pi/2, \Delta\theta = \pi/2) = LS^2\begin{pmatrix} 4J_2 & J_1 \\ J_1 & 0 \end{pmatrix}. \tag{A.15}
$$

Here, the off-diagonal elements do not vanish, and to determine the positive definiteness of the matrix, the eigenvalues need to be found by diagonalization. The characteristic polynomial is

$$
\begin{aligned}
\det(H_E - \lambda) = LS^2\begin{vmatrix} 4J_2 - \lambda & J_1 \\ J_1 & -\lambda \end{vmatrix} &= LS^2\left((-\lambda)(4J_2 - \lambda) - J_1^2\right) \\
&= LS^2(\lambda^2 - 4J_2\lambda - J_1^2)\,,
\end{aligned} \tag{A.16}
$$

which gives the eigenvalues

$$\lambda_{1,2} = -\frac{(-4J_2)}{2} \pm \sqrt{\frac{(4J_2)^2}{4} + J_1^2}$$
$$= 2J_2 \pm \sqrt{4J_2^2 + J_1^2} \overset{!}{>} 0. \tag{A.17}$$

This cannot be satisfied, $(\theta = \pi/2, \Delta\theta = \pi/2)$ is therefore neither minimum nor maximum but a saddle point.

In summary, the energy $E(\theta, \Delta\theta)$ has the minima

$$\begin{aligned} \theta = \pi, \ \Delta\theta = 0 && \text{if } J_1 > 4J_2 \\ \theta = \arccos\left(-\tfrac{J_1}{4J_2}\right), \ \Delta\theta = 0 && \text{if } J_1 < 4J_2. \end{aligned} \tag{A.18}$$

B. Perturbation Theory in t_1

The Kondo lattice on a zigzag ladder has, depending on the Kondo coupling J and the frustration φ, two fundamentally different ground states. For large J, there is only a spiral phase with a constant nearest-neighbor angle θ, depending on φ either $\theta = \pi$, i.e. an antiferromagnetic, or $\pi > \theta > \pi/2$, an incommensurate spiral configuration. For small and medium values of J, however, there is an additional possibility - the *dimerized* phase. Here, two angles are necessary to describe the spin configuration. In the main part of the thesis, this is parameterized by two angles θ and $\Delta\theta$. Near $\varphi = \pi/2$, that is for $t_2 \gg t_1$, there is a J-dependent transition from a dimerized phase with $(\theta = \pi/2, \Delta\theta = \pi/2)$ to a 90° spiral phase with $(\theta = \pi/2, \Delta\theta = 0)$. The idea is now to illuminate this transition and perhaps even generate a critical value of J by applying perturbation theory in t_1. For this purpose, the parameterization of angles is slightly different in this section than in the rest of the thesis. Here, the starting point is two decoupled chains, each with an antiferromagnetic spin configuration as pictured in Fig. B.1. The angle labeled θ here denotes the angle between these two chains, where $\theta = \pi/2$ describes the homogenous 90° spiral phase and all $\theta \neq \pi/2$ would be classified as dimerized. For $t_1 = 0$ this is evidently infinitely degenerate. The question now arises, whether this is true even when t_1 is turned on as a small perturbation.
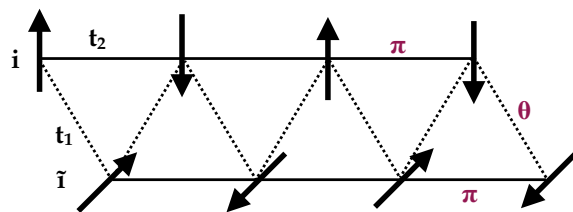

Figure B.1.: Starting point for the perturbation theory in t_1, i.e. two decoupled chains with nearest neighbor hopping t_2 and an angle of π between neighboring spins. Between the two chains, there is a global angle θ. If $\theta = \pi/2$, this configuration would depict a 90° spiral, all other values of θ constitute a dimerized configuration. Note that the picture is simplified and the hopping is of course actually between the underlying electrons. Indices on chain 1 are labelled with i, indices on chain 2 with $\tilde{i}$.

The Hamiltonian for two decoupled chains with sites i in chain 1 and sites $\tilde{i}$ in chain 2 is

$$H_0 = t_2 \sum_{\langle ij \rangle, \sigma} c_{i\sigma}^\dagger c_{j\sigma} + J \sum_i \boldsymbol{s}_i \boldsymbol{S}_i + t_2 \sum_{\langle \tilde{i}\tilde{j} \rangle, \sigma} \tilde{c}_{\tilde{i}\sigma}^\dagger \tilde{c}_{\tilde{j}\sigma} + J \sum_{\tilde{i}} \tilde{\boldsymbol{s}}_{\tilde{i}} \tilde{\boldsymbol{S}}_{\tilde{i}} \tag{B.1}$$

with classical spins $\boldsymbol{S}_i$ (or analogously $\tilde{\boldsymbol{S}}_{\tilde{i}}$)

$$\boldsymbol{S}_i = (-1)^i S \boldsymbol{n}, \tag{B.2}$$

where $\boldsymbol{n}$ is the unit vector in the direction of the antiferromagnetic spin configuration and S is the length of the classical spins. The Hamiltonian on chain $a \in (1,2)$ can thus be written as:

$$H_0^{(a)} = \sum_{ij\sigma\sigma'} \left(t_{ij} \delta_{\sigma\sigma'} + \delta_{ij} \frac{JS}{2} (-1)^i (\boldsymbol{n} \cdot \boldsymbol{\sigma})_{\sigma\sigma'} \right) c_{i\sigma}^\dagger c_{j\sigma'} \tag{B.3}$$

where $t_{ij} = t_2 \neq 0$ only for nearest neighbors on the same chain and with the spherical angles ϑ, φ

$$\boldsymbol{n} = \begin{pmatrix} \sin\vartheta \cos\varphi \\ \sin\vartheta \sin\varphi \\ \cos\vartheta \end{pmatrix} \quad \text{and} \quad \boldsymbol{n} \cdot \boldsymbol{\sigma} = \begin{pmatrix} \cos\vartheta & \sin\vartheta\, \mathrm{e}^{-i\varphi} \\ \sin\vartheta\, \mathrm{e}^{i\varphi} & -\cos\vartheta \end{pmatrix} \tag{B.4}$$

restricting the spins to the $x - y$-plane eliminates φ so that $\mathrm{e}^{-i\varphi} = \mathrm{e}^{i\varphi} = 1$. Furthermore, since only the orientation of the chains relative to each other is important here, not their absolute angle in space, we can set $\vartheta^{(i)} \equiv \theta$ and $\vartheta^{(\tilde{i})} \equiv 0$.

The hopping term of the free Hamiltonian is diagonalized by a Fourier transform to momentum space

$$H_{\mathrm{hopp}} = \sum_{k\sigma} \varepsilon_k c_{k\sigma}^\dagger c_{k\sigma}$$

$$\text{with} \quad c_{k\sigma} = \frac{1}{\sqrt{L}} \sum_j \mathrm{e}^{-ijk} c_{j\sigma} \equiv \sum_j U_{jk}^\dagger c_{j\sigma} \tag{B.5}$$

$$\text{and} \quad \varepsilon_k = -2t_2 \cos(k)$$

with this and $(-1)^i = \mathrm{e}^{i\pi}$, the entire free Hamiltonian of chain 1 can be written in momentum space in matrix form as

$$H_0 = \sum_k \begin{pmatrix} c_{k,\uparrow}^\dagger & c_{k,\downarrow}^\dagger & c_{k+\pi,\uparrow}^\dagger & c_{k+\pi,\downarrow}^\dagger \end{pmatrix} M \begin{pmatrix} c_{k,\uparrow} \\ c_{k,\downarrow} \\ c_{k+\pi,\uparrow} \\ c_{k+\pi,\downarrow} \end{pmatrix} \quad \text{where} \quad M = \begin{pmatrix} -\varepsilon_k & 0 & \Delta\cos\theta & \Delta\sin\theta \\ 0 & -\varepsilon_k & \Delta\sin\theta & -\Delta\cos\theta \\ \Delta\cos\theta & \Delta\sin\theta & \varepsilon_k & 0 \\ \Delta\sin\theta & -\Delta\cos\theta & 0 & \varepsilon_k \end{pmatrix}$$

$$\text{(B.6)}$$

with $\Delta = JS/2$. The matrix M is diagonalized by

$$V^\dagger M V = \lambda \quad \text{with Eigenvalues} \quad \lambda = \pm\sqrt{\Delta^2 + \varepsilon_k^2} \equiv \pm E_k$$

$$\text{and} \quad V = \begin{pmatrix} -\dfrac{B_{k-}\sin\theta}{N_{k-}} & -\dfrac{B_{k-}\sin\theta}{N_{k-}} & \dfrac{B_{k+}\sin\theta}{N_{k+}} & \dfrac{B_{k+}\cos\theta}{N_{k+}} \\ \dfrac{B_{k-}\cos\theta}{N_{k-}} & -\dfrac{B_{k-}\cos\theta}{N_{k-}} & -\dfrac{B_{k+}\cos\theta}{N_{k+}} & \dfrac{B_{k+}\sin\theta}{N_{k+}} \\ 0 & 1/N_{k-} & 0 & 1/N_{k+} \\ 1/N_{k-} & 0 & 1/N_{k+} & 0 \end{pmatrix}$$

$$\equiv \begin{pmatrix} v_1 & v_2 & v_3 & v_4 \end{pmatrix}$$

$$\text{(B.7)}$$

with the abbreviations $B_{k\pm} = (E_k \pm \varepsilon_k)/\Delta$ and $N_{k\pm} = \sqrt{B_{k\pm}^2 + 1}$, where v_1, v_2 are eigenvectors to the eigenvalue $-E_k$ and v_3, v_4 to $+E_k$.

The diagonalized Hamiltonian can thus be written as

$$H_0 = \sum_{k,m,\mu} \mu E_k \Psi_{k\mu m}^\dagger \Psi_{k\mu m}$$

$$\text{where} \quad m = 1,2 \text{ if } \mu = +, \quad m = 3,4 \text{ if } \mu = -$$

$$\text{and} \quad -\pi/2 < k \leq \pi/2, \quad \Delta k = 2\pi/L$$

$$\text{(B.8)}$$

with quasiparticle operators Ψ_k that are given by

$$\Psi_k = V^\dagger c_k \quad \text{where} \quad c_k = \begin{pmatrix} c_{k,\uparrow} \\ c_{k,\downarrow} \\ c_{k+\pi,\uparrow} \\ c_{k+\pi,\downarrow} \end{pmatrix}$$

$$\text{(B.9)}$$

and can be used to express the ground state as

$$|G\rangle = \prod_{k,m} \left(\Psi^\dagger_{km-}|0\rangle \check{\Psi}^\dagger_{km-}|\tilde{0}\rangle \right)$$

$$\text{where} \quad -\pi/2 < k \leq \pi/2 \quad \text{and} \quad m = 1, 2$$

(B.10)

i.e. the lower band with energy $-E_k$ is completely filled, and the upper band with $+E_k$ completely empty at half-filling.

Perturbation theory is now performed by slowly turning on the hopping t_1 between the two 1D chains. The perturbation is given by

$$H_1 = \sum_{\langle i\tilde{i} \rangle} t_{i\tilde{i}} c^\dagger_{i\sigma} \tilde{c}_{\tilde{i}\sigma} + h.c.$$

(B.11)

where $\langle i\tilde{i} \rangle$ denotes neighboring sites from chain 1 to chain 2 and vice versa.

For convenience, a notation is introduced to keep track of created and destroyed particles in the two chains. Let $|1, -1\rangle$ denote the state where one particle is created in chain 1 and one destroyed in chain 2. With this:

$$H_1|G\rangle \propto t_1|1, -1\rangle + t_1| -1, 1\rangle$$

(B.12)

The first order correction to the ground state energy is given by

$$\Delta E^{(1)} = \langle G|H_1|G\rangle,$$

(B.13)

which evidently vanishes, since $\langle 0, 0| -1, 1\rangle = \langle 0, 0|1, -1\rangle = 0$.

The second order correction to the ground state energy is

$$\Delta E^{(2)} = \sum_n \frac{|\langle G|H_1|n\rangle|^2}{E_n - E_0}$$

(B.14)

where $\sum_n$ is over all excited states n that result in a non-vanishing matrix element. The only states that achieve this are the one-particle excitations

$$H_1|1, -1\rangle \propto t_1|0, 0\rangle + t_1|2, -2\rangle,$$
$$H_1| -1, 1\rangle \propto t_1|0, 0\rangle + t_1| -2, 2\rangle.$$

(B.15)

More precisely,

$$|1,-1\rangle = |k\tilde{k}m\tilde{m}\rangle = \Psi^\dagger_{km+}\tilde{\Psi}_{\tilde{k}\tilde{m}-}|G\rangle \quad \text{where} \quad \tilde{m} = 1,2 \quad \text{and} \quad m = 3,4 \tag{B.16}$$

Rewriting the Fourier transformation as

$$\begin{aligned}
c^\dagger_{j\sigma} &= \frac{1}{\sqrt{L}} \sum_{-\pi/2 < k \leq \pi/2} \left(e^{-ikj} c^\dagger_{k\sigma} + e^{-i(k+\pi)j} c^\dagger_{k+\pi,\sigma} \right) \\
&\equiv \sum_{-\pi/2 < k \leq \pi/2} (U^\dagger_{jk} c^\dagger_k)_\sigma \\
&\equiv \sum_{\substack{k'=k,k+\pi \\ -\pi/2 < k \leq \pi/2}} U^\dagger_{jk'\sigma} c^\dagger_{k'\sigma}
\end{aligned} \tag{B.17}$$

with

$$\boldsymbol{U}^\dagger_{jk} = \begin{pmatrix} U^\dagger_{jk\uparrow} & U^\dagger_{jk\downarrow} & U^\dagger_{j(k+\pi)\uparrow} & U^\dagger_{j(k+\pi)\downarrow} \end{pmatrix} \tag{B.18}$$

where $U^\dagger_{jk\uparrow} = U^\dagger_{jk\downarrow} = \frac{1}{\sqrt{L}} e^{-ikj}$ and $U^\dagger_{j(k+\pi)\uparrow} = U^\dagger_{j(k+\pi)\downarrow} = \frac{1}{\sqrt{L}} e^{-i(k+\pi)j}$.

The perturbation Eq. (B.11) can thus be written as

$$\begin{aligned}
H_1 &= t_1 \sum_{\langle i\tilde{i}\rangle \sigma k'\tilde{k}'} U^\dagger_{ik'\sigma} c^\dagger_{k'\sigma} \tilde{U}_{\tilde{i}\tilde{k}'\sigma} \tilde{c}_{\tilde{k}'\sigma} + h.c. \\
&= t_1 \sum_{\langle i\tilde{i}\rangle \sigma k'\tilde{k}'} U^\dagger_{ik'\sigma} V^\dagger_{k'\sigma,\mu m} \Psi^\dagger_{k,\mu m} \tilde{U}_{\tilde{i}\sigma\tilde{k}'} \tilde{V}_{\tilde{k}'\sigma,\tilde{\mu}\tilde{m}} \tilde{\Psi}_{\tilde{k},\tilde{\mu}\tilde{m}} + h.c.
\end{aligned} \tag{B.19}$$

Together with Eq. (B.16), the non-vanishing matrix elements from Eq. (B.14) can be calculated

$$\begin{aligned}
\langle G|H_1|q\tilde{q}n\tilde{n}\rangle &= \langle G| \left(t_1 \sum_{\langle i\tilde{i}\rangle \sigma k'\tilde{k}'} U^\dagger_{ik'\sigma} V^\dagger_{k'\sigma,\mu m} \Psi^\dagger_{k,\mu m} \tilde{U}_{\tilde{i}\sigma\tilde{k}'} \tilde{V}_{\tilde{k}'\sigma,\tilde{\mu}\tilde{m}} \tilde{\Psi}_{\tilde{k},\tilde{\mu}\tilde{m}} \right) \left(\tilde{\Psi}^\dagger_{\tilde{q}\tilde{n}+} \Psi_{qn-}|G\rangle \right) \\
&= \langle G|t_1 \sum_{\langle i\tilde{i}\rangle \sigma k'\tilde{k}'} U^\dagger_{ik'\sigma} V^\dagger_{k'\sigma,\mu m} \tilde{U}_{\tilde{i}\sigma\tilde{k}'} \tilde{V}_{\tilde{k}'\sigma,\tilde{\mu}\tilde{m}} \Psi^\dagger_{k,\mu m} \tilde{\Psi}_{\tilde{k},\tilde{\mu}\tilde{m}} \tilde{\Psi}^\dagger_{\tilde{q}\tilde{n}+} \Psi_{qn-}|G\rangle \\
&= \langle G|t_1 \sum_{\langle i\tilde{i}\rangle \sigma k'\tilde{k}'} U^\dagger_{ik'\sigma} V^\dagger_{k'\sigma,\mu m} \tilde{U}_{\tilde{i}\sigma\tilde{k}'} \tilde{V}_{\tilde{k}'\sigma,\tilde{\mu}\tilde{m}} \delta_{\mu-}\delta_{\tilde{\mu}+}\delta_{kq}\delta_{mn}\delta_{\tilde{k}\tilde{q}}\delta_{\tilde{m}\tilde{n}}|G\rangle \\
&= t_1 \sum_{\langle i\tilde{i}\rangle \sigma} U^\dagger_{iq'\sigma} V^\dagger_{q'\sigma,-n} \tilde{U}_{\tilde{i}\sigma\tilde{q}'} \tilde{V}_{\tilde{q}'\sigma,+\tilde{n}} ,
\end{aligned} \tag{B.20}$$

or, explicitly,

$$\langle G|H_1|q\tilde{q}n\tilde{n}\rangle = \frac{t_1}{L} \sum_{\langle j\tilde{j}\rangle} \left[\begin{pmatrix} e^{-iqj} \\ e^{-iqj} \\ e^{-i(q+\pi)j} \\ e^{-i(q+\pi)j} \end{pmatrix} \cdot v_n \right] \cdot \left[\begin{pmatrix} e^{i\tilde{q}\tilde{j}} \\ e^{i\tilde{q}\tilde{j}} \\ e^{i(\tilde{q}+\pi)\tilde{j}} \\ e^{i(\tilde{q}+\pi)\tilde{j}} \end{pmatrix} \cdot \tilde{v}_{\tilde{n}} \right] \tag{B.21}$$

where $n = 1,2$ and $\tilde{n} = 3,4$ since $\mu = -$ and $\tilde{\mu} = +$. The second-order contribution from Eq. (B.14) includes the sum over all $q, \tilde{q}, n, \tilde{n}$:

$$\Delta E^{(2)} = \sum_{q\tilde{q}n\tilde{n}} \frac{|\langle G|H_1|q\tilde{q}n\tilde{n}\rangle|^2}{E_{q\tilde{q}n\tilde{n}} - E_0} . \tag{B.22}$$

The energy difference in the denominator is simply

$$E_{q\tilde{q}n\tilde{n}} - E_0 = \sum_{\substack{-\pi/2 < k \leq \pi/2 \\ k \neq q}} (-E_k) + E_{\tilde{q}} - \left(\sum_{-\pi/2 < k \leq \pi/2} (-E_k) \right) \tag{B.23}$$

$$= E_{\tilde{q}} + E_q .$$

The numerator in Eq. (B.22) contains four matrix elements per $(q, \tilde{q})$ stemming from the combinations of $(v_n, \tilde{v}_{\tilde{n}})$.

The first is $(v_1, \tilde{v}_3)$

$$\frac{t_1}{L} \sum_{\langle j\tilde{j}\rangle} \left[\begin{pmatrix} e^{-iqj} \\ e^{-iqj} \\ e^{-i(q+\pi)j} \\ e^{-i(q+\pi)j} \end{pmatrix} \cdot v_1 \right] \cdot \left[\begin{pmatrix} e^{i\tilde{q}\tilde{j}} \\ e^{i\tilde{q}\tilde{j}} \\ e^{i(\tilde{q}+\pi)\tilde{j}} \\ e^{i(\tilde{q}+\pi)\tilde{j}} \end{pmatrix} \cdot \tilde{v}_3 \right]$$

$$= \frac{t_1}{LN_q^- N_{\tilde{q}}^+} \sum_{\langle j\tilde{j}\rangle} \left[\begin{pmatrix} e^{-iqj} \\ e^{-iqj} \\ e^{-i(q+\pi)j} \\ e^{-i(q+\pi)j} \end{pmatrix} \cdot \begin{pmatrix} -B_q^- \sin\theta \\ B_q^- \cos\theta \\ 0 \\ 1 \end{pmatrix} \right] \cdot \left[\begin{pmatrix} e^{i\tilde{q}\tilde{j}} \\ e^{i\tilde{q}\tilde{j}} \\ e^{i(\tilde{q}+\pi)\tilde{j}} \\ e^{i(\tilde{q}+\pi)\tilde{j}} \end{pmatrix} \cdot \begin{pmatrix} 0 \\ -B_{\tilde{q}}^+ \\ 0 \\ 1 \end{pmatrix} \right] \tag{B.24}$$

$$= \frac{t_1}{LN_q^- N_{\tilde{q}}^+} \sum_{\langle j\tilde{j}\rangle} \left[-B_q^- \sin\theta e^{-iqj} + B_q^- \cos\theta e^{-iqj} + e^{-i(q+\pi)j} \right]$$

$$\cdot \left[-B_{\tilde{q}}^+ e^{i\tilde{q}j} + e^{i(\tilde{q}+\pi)j} \right]$$

using $\cos(x) - \sin(x) = \sqrt{2}\cos(x + \pi/4) \equiv \sqrt{2}\cos(\tilde{x})$:

$$\frac{t_1}{LN_q^- N_{\tilde{q}}^+} \sum_{\langle j\tilde{j}\rangle} \left[-B_q^- \sin\theta e^{-iqj} + B_q^- \cos\theta e^{-iqj} + e^{-i(q+\pi)j} \right]$$
$$\cdot \left[-B_{\tilde{q}}^+ e^{i\tilde{q}j} + e^{i(\tilde{q}+\pi)j} \right] \tag{B.25}$$
$$= \frac{t_1}{LN_q^- N_{\tilde{q}}^+} \sum_{\langle j\tilde{j}\rangle} \left[B_q^- \sqrt{2}\cos\tilde{\theta} e^{-iqj} + e^{-i(q+\pi)j} \right] \cdot \left[-B_{\tilde{q}}^+ e^{i\tilde{q}j} + e^{i(\tilde{q}+\pi)j} \right] \; .$$

This differs from the expression for $(v_1, \tilde{v}_4)$ only by a sign in the second bracket:

$$\frac{t_1}{L} \sum_{\langle j\tilde{j}\rangle} \left[\left(\begin{pmatrix} e^{-iqj} \\ e^{-iqj} \\ e^{-i(q+\pi)j} \\ e^{-i(q+\pi)j} \end{pmatrix} \cdot v_1 \right) \cdot \left(\begin{pmatrix} e^{i\tilde{q}\tilde{j}} \\ e^{i\tilde{q}\tilde{j}} \\ e^{i(\tilde{q}+\pi)\tilde{j}} \\ e^{i(\tilde{q}+\pi)\tilde{j}} \end{pmatrix} \cdot \tilde{v}_4 \right) \right]$$
$$= \frac{t_1}{LN_q^- N_{\tilde{q}}^+} \sum_{\langle j\tilde{j}\rangle} \left[\left(\begin{pmatrix} e^{-iqj} \\ e^{-iqj} \\ e^{-i(q+\pi)j} \\ e^{-i(q+\pi)j} \end{pmatrix} \cdot \begin{pmatrix} -B_q^- \sin\theta \\ B_q^- \cos\theta \\ 0 \\ 1 \end{pmatrix} \right) \cdot \left(\begin{pmatrix} e^{i\tilde{q}\tilde{j}} \\ e^{i\tilde{q}\tilde{j}} \\ e^{i(\tilde{q}+\pi)\tilde{j}} \\ e^{i(\tilde{q}+\pi)\tilde{j}} \end{pmatrix} \cdot \begin{pmatrix} B_{\tilde{q}}^+ \\ 0 \\ 1 \\ 0 \end{pmatrix} \right) \right] \tag{B.26}$$
$$= \frac{t_1}{LN_q^- N_{\tilde{q}}^+} \sum_{\langle j\tilde{j}\rangle} \left[B_q^- \sqrt{2}\cos\tilde{\theta} e^{-iqj} + e^{-i(q+\pi)j} \right] \cdot \left[B_{\tilde{q}}^+ e^{i\tilde{q}\tilde{j}} + e^{i(\tilde{q}+\pi)\tilde{j}} \right]$$

For $\epsilon = \pm 1$ these matrix elements are

$$\frac{t_1}{LN_q^- N_{\tilde{q}}^+} \sum_{\langle j\tilde{j}\rangle} \left[B_q^- \sqrt{2}\cos\tilde{\theta} e^{-iqj} + e^{-i(q+\pi)j} \right] \cdot \left[\epsilon B_{\tilde{q}}^+ e^{i\tilde{q}j} + e^{i(\tilde{q}+\pi)\tilde{j}} \right]$$
$$= \frac{t_1}{LN_q^- N_{\tilde{q}}^+} \sum_{\langle j\tilde{j}\rangle} \left[B_q^- B_{\tilde{q}}^+ \sqrt{2}\cos\tilde{\theta} e^{i(\tilde{q}\tilde{j}-qj)} + B_q^- \sqrt{2}\cos\tilde{\theta} e^{i((\tilde{q}+\pi)\tilde{j}-qj)} \right. \tag{B.27}$$
$$\left. + \epsilon B_{\tilde{q}}^+ e^{i(\tilde{q}\tilde{j}-(q+\pi)j)} + e^{i[(\tilde{q}+\pi)\tilde{j}-(q+\pi)j]} \right] \; .$$

The sites j and $\tilde{j}$ on the two chains that are adjacent can be labeled as $\tilde{j} = j$ and $\tilde{j} = j+1$. This leads

to

$$\frac{t_1}{LN_q^- N_{\tilde{q}}^+} \sum_j \left[B_q^- B_{\tilde{q}}^+ \sqrt{2} \cos \tilde{\theta} e^{i(\tilde{q}-q)j} \left(1 + e^{i\tilde{q}}\right) + B_q^- \sqrt{2} \cos \tilde{\theta} e^{i((\tilde{q}+\pi)-q)j} \left(1 + e^{i(\tilde{q}+\pi)}\right) \right.$$

$$\left. + \epsilon B_{\tilde{q}}^+ e^{i(\tilde{q}-(q+\pi))j} \left(1 + e^{i\tilde{q}}\right) + e^{i[(\tilde{q}+\pi)-(q+\pi)]j} \left(1 + e^{i(\tilde{q}+\pi)}\right) \right]$$

$$= \frac{t_1}{N_q^- N_{\tilde{q}}^+} \left[B_q^- B_{\tilde{q}}^+ \sqrt{2} \cos \tilde{\theta} \delta_{q,\tilde{q}} \left(1 + e^{i\tilde{q}}\right) + B_q^- \sqrt{2} \cos \tilde{\theta} \delta_{q,(\tilde{q}+\pi)} \left(1 - e^{i\tilde{q}}\right) \right.$$

$$\left. + \epsilon B_{\tilde{q}}^+ \delta_{(q+\pi),\tilde{q}} \left(1 + e^{i\tilde{q}}\right) + \delta_{q,\tilde{q}} \left(1 - e^{i\tilde{q}}\right) \right]$$

$$= \frac{t_1}{N_q^- N_{\tilde{q}}^+} \left[\delta_{q,\tilde{q}} \left(B_q^- B_{\tilde{q}}^+ \sqrt{2} \cos \tilde{\theta} + 1 + e^{i\tilde{q}} \left(B_q^- B_{\tilde{q}}^+ \sqrt{2} \cos \tilde{\theta} - 1 \right) \right) \right.$$

$$\left. + \delta_{q,(\tilde{q}+\pi)} \left(B_q^- \sqrt{2} \cos \tilde{\theta} + \epsilon B_{\tilde{q}}^+ + e^{i\tilde{q}} \left(\epsilon B_{\tilde{q}}^+ - B_q^- \sqrt{2} \cos \tilde{\theta} \right) \right) \right]$$

where $\frac{1}{L} \sum_j e^{i(k-q)j} = \delta_{k,q}$ and $e^{i\pi} = -1$ was used. The whole expression in Eq. (B.28) then needs to be squared. Terms containing both $\delta_{q,\tilde{q}}$ and $\delta_{q,(\tilde{q}+\pi)}$ would not survive the momentum sum since they cannot be simultaneously satisfied, it is therefore enough to square the terms $\propto \delta_{q,\tilde{q}}$ and $\propto \delta_{q,(\tilde{q}+\pi)}$ individually. Using $(a + be^{ix})(a + be^{-ix}) = a^2 + b^2 + 2\cos(x)ab$, the term $\propto \delta_{q,\tilde{q}}$ squared is

$$\left[\frac{t_1}{N_q^- N_{\tilde{q}}^+} \right]^2 \left[\left(B_q^- B_{\tilde{q}}^+ \sqrt{2} \cos \tilde{\theta} + 1 \right)^2 + \left(B_q^- B_{\tilde{q}}^+ \sqrt{2} \cos \tilde{\theta} - 1 \right)^2 \right.$$

$$\left. + 2\cos(\tilde{q}) \left(B_q^- B_{\tilde{q}}^+ \sqrt{2} \cos \tilde{\theta} + 1 \right) \left(B_q^- B_{\tilde{q}}^+ \sqrt{2} \cos \tilde{\theta} - 1 \right) \right]$$

$$= 2 \left[\frac{t_1}{N_q^- N_{\tilde{q}}^+} \right]^2 \left[2(B_q^- B_{\tilde{q}}^+)^2 \cos^2 \tilde{\theta} + 1 + \cos(\tilde{q}) \left(2(B_q^- B_{\tilde{q}}^+)^2 \cos^2 \tilde{\theta} - 1 \right) \right]$$

while the term $\propto \delta_{q,(\tilde{q}+\pi)}$ squared is

$$\left[\frac{t_1}{N_q^- N_{\tilde{q}}^+} \right]^2 \left[\left(B_q^- \sqrt{2} \cos \tilde{\theta} + \epsilon B_{\tilde{q}}^+ \right)^2 + \left(\epsilon B_{\tilde{q}}^+ - B_q^- \sqrt{2} \cos \tilde{\theta} \right)^2 \right.$$

$$\left. + 2\cos(\tilde{q}) \left(B_q^- \sqrt{2} \cos \tilde{\theta} + \epsilon B_{\tilde{q}}^+ \right) \left(\epsilon B_{\tilde{q}}^+ - B_q^- \sqrt{2} \cos \tilde{\theta} \right) \right]$$

$$= 2 \left[\frac{t_1}{N_q^- N_{\tilde{q}}^+} \right]^2 \left[2(B_q^-)^2 \cos^2 \tilde{\theta} + (B_{\tilde{q}}^+)^2 + \cos(\tilde{q}) \left((B_{\tilde{q}}^+)^2 - 2(B_q^-)^2 \cos^2 \tilde{\theta} \right) \right]$$

after evaluating the sum over $\tilde{q}$ and noting that $B_{q+\pi}^+ = B_q^-$, $E_{q+\pi} = E_q$ and $N_{q+\pi}^+ = N_q^-$ this yields for $n = 1$ and $\tilde{n} = 3, 4$

$$|\langle G|H_1|q\tilde{q}n = 1, \tilde{n} = 3\rangle|^2 + |\langle G|H_1|q\tilde{q}n = 1, \tilde{n} = 4\rangle|^2$$

$$= 4\left[\left[\frac{t_1}{N_q^- N_{\tilde{q}}^+}\right]^2 + \left[\frac{t_1 B_q^-}{(N_q^-)^2}\right]^2\right]\left(2\cos^2\tilde{\theta} + 1 + \cos(q)\left(2\cos^2\tilde{\theta} - 1\right)\right).$$

The case $n = 2$ and $\tilde{n} = 3, 4$ is very similar.

All in all, the $(n, \tilde{n})$ sum in the numerator in Eq. (B.22) gives:

$$\sum_{n,\tilde{n}}|\langle G|H_1|q\tilde{q}n\tilde{n}\rangle|^2$$

$$= K(q) \cdot \left[2(\cos^2\tilde{\theta} + \sin^2\tilde{\theta}) + 2 + \cos(q) \cdot \left(2(\cos^2\tilde{\theta} + \sin^2\tilde{\theta}) - 2\right)\right] \tag{B.28}$$

$$= 4 \cdot K(q),$$

where $K(q)$ is a prefactor depending only on q. As the energy difference in the denominator also only depends on q and not on θ, unfortunately, this result shows, that up to $\mathcal{O}(t_1^2)$ the homogenous spiral and dimerized spin configurations are degenerate for all values of J. Hope of calculating a critical value of J therefore lies in fourth order perturbation theory at the earliest, since it is apparent by looking at non-vanishing matrix elements, that the third order correction entirely vanishes. As the second order correction was already very computationally intensive, however, this does not seem very practical.

Bibliography

1. P. W. Anderson, Science **177**, 393 (1972).

2. M. Tinkham, *Introduction to Superconductivity*, 2. ed (Dover Publ, Mineola, NY, 2004).

3. L. Savary and L. Balents, Rep. Prog. Phys. **80**, 016502 (2016).

4. J. K. Asbóth, L. Oroszlány, and A. Pályi, *A Short Course on Topological Insulators* (Springer International Publishing, Cham, 2016).

5. G. H. Wannier, Phys. Rev. **79**, 357 (1950).

6. A. Yoshimori, J. Phys. Soc. Jpn. **14**, 807 (1959).

7. J. Villain, J. Phys. Chem. Solids **11**, 303 (1959).

8. T. A. Kaplan, Phys. Rev. **116**, 888 (1959).

9. E. Dagotto, *Nanoscale Phase Separation and Colossal Magnetoresistance: The Physics of Manganites and Related Compounds* (Springer, London, 2011).

10. S. Yunoki, J. Hu, A. L. Malvezzi, A. Moreo, N. Furukawa, and E. Dagotto, Phys. Rev. Lett. **80**, 845 (1998).

11. Y. Tokura, A. Urushibara, Y. Moritomo, T. Arima, A. Asamitsu, G. Kido, and N. Furukawa, J. Phys. Soc. Jpn. **63**, 3931 (1994).

12. W. Nolting, G. G. Reddy, A. Ramakanth, and D. Meyer, Phys. Rev. B **64**, (2001).

13. I. Martin and C. D. Batista, Phys. Rev. Lett. **101**, (2008).

14. S. Kumar and J. van den Brink, Phys. Rev. Lett. **105**, (2010).

15. Y. Akagi, M. Udagawa, and Y. Motome, Phys. Rev. Lett. **108**, (2012).

16. Y. Akagi and Y. Motome, J. Phys. Soc. Jpn. **79**, 083711 (2010).

17. Y. Kato, I. Martin, and C. D. Batista, Phys. Rev. Lett. **105**, 266405 (2010).

18. K. Barros, J. W. F. Venderbos, G.-W. Chern, and C. D. Batista, Phys. Rev. B **90**, (2014).

19. Y. Tokiwa, J. J. Ishikawa, S. Nakatsuji, and P. Gegenwart, Nat. Mater. **13**, 356 (2014).

20. M. Peschke, R. Rausch, and M. Potthoff, Phys. Rev. B **97**, (2018).

21. M. Peschke, L.-M. Woelk, and M. Potthoff, Phys. Rev. B **99**, 085140 (2019).

22. V. I. Yukalov, Laser Phys. Lett. **8**, 485 (2011).

23. A. V. Gorshkov, M. Hermele, V. Gurarie, C. Xu, P. S. Julienne, J. Ye, P. Zoller, E. Demler, M. D. Lukin, and A. M. Rey, Nat. Phys. **6**, 289 (2010).

24. M. Foss-Feig, M. Hermele, V. Gurarie, and A. M. Rey, Phys. Rev. A **82**, (2010).

25. M. Foss-Feig, M. Hermele, and A. M. Rey, Phys. Rev. A **81**, 051603 (2010).

26. S. Dörscher, A. Thobe, B. Hundt, A. Kochanke, R. Le Targat, P. Windpassinger, C. Becker, and K. Sengstock, Rev. Sci. Instrum. **84**, 043109 (2013).

27. A. Kochanke, Towards Quantum Simulation of the Kondo-Lattice-Model, PhD Thesis, Universität Hamburg, 2017.

28. L. Riegger, N. D. Oppong, M. Höfer, D. R. Fernandes, I. Bloch, and S. Fölling, Phys. Rev. Lett. **120**, 143601 (2018).

29. M. Rigol, V. Dunjko, and M. Olshanii, Nature **452**, 854 (2008).

30. M. Rigol and M. Srednicki, Phys. Rev. Lett. **108**, 110601 (2012).

31. M. Heyl, A. Polkovnikov, and S. Kehrein, Phys. Rev. Lett. **110**, 135704 (2013).

32. C. Karrasch and D. Schuricht, Phys. Rev. B **87**, 195104 (2013).

33. E. Canovi, P. Werner, and M. Eckstein, Phys. Rev. Lett. **113**, 265702 (2014).

34. M. Kollar, F. A. Wolf, and M. Eckstein, Phys. Rev. B **84**, 054304 (2011).

35. T. Langen, T. Gasenzer, and J. Schmiedmayer, J. Stat. Mech. **2016**, 064009 (2016).

36. D. Fausti, R. I. Tobey, N. Dean, S. Kaiser, A. Dienst, M. C. Hoffmann, S. Pyon, T. Takayama, H. Takagi, and A. Cavalleri, Science **331**, 189 (2011).

37. P. Coleman, in *Handbook of Magnetism and Advanced Magnetic Materials* (American Cancer Society, 2007).

38. J. R. Schrieffer and P. A. Wolff, Phys. Rev. **149**, 491 (1966).

39. D. I. Khomskii, *Basic Aspects of the Quantum Theory of Solids: Order and Elementary Excitations* (Cambridge University Press, Cambridge, 2010).

40. Y. Akagi and Y. Motome, J. Korean Phys. Soc. **63**, 405 (2013).

41. K. Ohgushi, S. Murakami, and N. Nagaosa, Phys. Rev. B **62**, R6065 (2000).

42. Y. I. Dublenych, Phys. Rev. B **93**, (2016).

43. M. A. Ruderman and C. Kittel, Phys. Rev. **96**, 99 (1954).

44. T. Kasuya, Prog Theor Phys **16**, 45 (1956).

45. K. Yosida, Phys. Rev. **106**, 893 (1957).

46. L.-M. Gebauer, Semiclassical Dynamics and Thermodynamics in the Kondo Lattice Model, Master Thesis, Universität Hamburg, 2015.

47. H. Tsunetsugu, M. Sigrist, and K. Ueda, Rev. Mod. Phys. **69**, 809 (1997).

48. G. F. Giuliani, G. Vignale, and T. Datta, Phys. Rev. B **72**, (2005).

49. Y. Yafet, Phys. Rev. B **36**, 3948 (1987).

50. S. R. White, Phys. Rev. Lett. **69**, 2863 (1992).

51. S. R. White, Phys. Rev. B **48**, 10345 (1993).

52. U. Schollwöck, Ann. Phys. **326**, 96 (2011).

53. K. A. Hallberg, Adv. Phys. **55**, 477 (2006).

54. U. Schollwöck and S. R. White, AIP Conference Proceedings **816**, 155 (2006).

55. N. D. Mermin and H. Wagner, Phys. Rev. Lett. **17**, 1133 (1966).

56. E. Pavarini and I. for Advanced Simulation, editors, *Emergent Phenomena in Correlated Matter: Lecture Notes of the Autumn School Correlated Electrons 2013 at Forschungszentrum Jülich, 23 − 27 September 2013* (Forschungszentrum Jülich, Jülich, 2013).

57. P. Henelius and A. W. Sandvik, Phys. Rev. B **62**, 1102 (2000).

58. V. I. Arnol′d, V. V. Kozlov, and A. I. Neĭshtadt, *Mathematical Aspects of Classical and Celestial Mechanics*, 3rd [rev. and exp.] ed (Springer, Berlin ; New York, 2006).

59. J. R. Dormand and P. J. Prince, J. Comput. Appl. Math. **6**, 19 (1980).

60. E. Jones, T. Oliphant, P. Peterson, and and others, *SciPy: Open Source Scientific Tools for Python* (2001−).

61. W. H. Press, editor, *Numerical Recipes: The Art of Scientific Computing*, 3rd ed (Cambridge University Press, Cambridge, UK ; New York, 2007).

62. H. G. Schuster and W. Just, *Deterministic Chaos: An Introduction*, 4., rev. and enl. ed (Wiley-VCH, Weinheim, 2005).

63. *Private Communication with Michael Potthoff* (2019).

64. H. Römer and T. Filk, *Statistische Mechanik* (VCH, Weinheim, 1994).

65. S. Wimberger, *Nonlinear Dynamics and Quantum Chaos* (Springer International Publishing, Cham, 2014).

66. V. I. Arnold, *Mathematical Methods of Classical Mechanics*, 2. ed (Springer, New York, NY, 2010).

67. J. L. McCauley, *Classical Mechanics: Transformations, Flows, Integrable, and Chaotic Dynamics* (Cambridge University Press, Cambridge ; New York, 1997).

68. B. K. Shivamoggi, *Nonlinear Dynamics and Chaotic Phenomena: An Introduction* (Springer Netherlands, Dordrecht, 2014).

69. J. L. McCauley, *Chaos, Dynamics, and Fractals: An Algorithmic Approach to Deterministic Chaos* (Cambridge University Press, Cambridge ; New York, NY, 1993).

70. R. Steinigeweg, Zur Dynamik von Klassischen Heisenberg-Systemen: Klassen Integrabler Systeme Und Symplektische Integratoren Für Nicht Integrable Systeme, Diplomarbeit, Universität Osnabrück, 2005.

71. E. Fermi, P. Pasta, S. Ulam, and M. Tsingou, *Studies of the Nonlinear Problems* (Los Alamos Scientific Lab., N. Mex., 1955).

72. N. J. Zabusky and M. D. Kruskal, Phys. Rev. Lett. **15**, 240 (1965).

73. C. S. Gardner, J. M. Greene, M. D. Kruskal, and R. M. Miura, Phys. Rev. Lett. **19**, 1095 (1967).

74. R. M. Miura, C. S. Gardner, and M. D. Kruskal, J. Math. Phys. **9**, 1204 (1968).

75. A. Kolmogorov, in *Proc. Intl. Congress of Math., Amsterdam* (1954), pp. 315–333.

76. J. Moser, Nachr Akad Wiss Gött. II 1 (1962).

77. V. I. Arnol'd, Russ. Math. Surv. **18**, 9 (1963).

78. F. Izrailev and B. Chirikov, in *Soviet Physics Doklady* (1966), p. 30.

79. E. A. Jackson, J. Math. Phys. **4**, 551 (1963).

80. E. A. Jackson, J. Math. Phys. **4**, 686 (1963).

81. H. Bethe, Z. Physik **71**, 205 (1931).

82. R. Steinigeweg and H.-J. Schmidt, Math. Phys. Anal. Geom. **12**, 19 (2009).

83. A. S. de Wijn, B. Hess, and B. V. Fine, Phys. Rev. Lett. **109**, (2012).

84. J. Sólyom, *Fundamentals of the Physics of Solids: Structure and Dynamics* (Springer, Berlin ; New York, 2007).

85. S. Blundell, *Magnetism in Condensed Matter* (Oxford University Press, Oxford ; New York, 2001).

86. N. Goldenfeld, *Lectures on Phase Transitions and the Renormalization Group* (Addison-Wesley, Advanced Book Program, Reading, Mass, 1992).

87. M. Vojta, Rep. Prog. Phys. **66**, 2069 (2003).

88. R. B. Griffiths, in *Phase Transitions and Critical Phenomena. Vol. 1: Exact Results* (Acad. Press, London, 1976).

89. A. Gelfert and W. Nolting, J. Phys. Condens. Matter **13**, R505 (2001).

90. N. N. Bogoliubov, Phys. Abhandl. SU **6**, 113 (1962).

91. J. Glimm and A. Jaffe, *Quantum Physics: A Functional Integral Point of View*, 2nd ed (Springer-Verlag, New York, 1987).

92. A. Auerbach, *Interacting Electrons and Quantum Magnetism.* (Springer, New York, 2012).

93. C. Noce and M. Cuoco, Phys. Rev. B **59**, 7409 (1999).

94. J. D. Fraser, Philos. Sci. **83**, 585 (2016).

95. R. Kindermann and J. L. Snell, *Markov Random Fields and Their Applications* (American Mathematical Society, 1980).

96. J. L. Lebowitz, Stat. Mech. **71**, 12 (1999).

List of Publications

The first part of this thesis concerning the equilibrium phase diagram (Chapter 3) is based on the following publication:

Peschke, M., Woelk, L.-M., Potthoff, M., 2019. *Phase diagram of the Kondo model on the zigzag ladder.* Phys. Rev. B 99, 085140. https://doi.org/10.1103/PhysRevB.99.085140

Eidesstattliche Versicherung / Declaration on oath

Hiermit versichere ich an Eides statt, die vorliegende Dissertationsschrift selbst verfasst und keine anderen als die angegebenen Hilfsmittel und Quellen benutzt zu haben.

Die eingereichte schriftliche Fassung entspricht der auf dem elektronischen Speichermedium.

Die Dissertation wurde in der vorgelegten oder einer ähnlichen Form nicht schon einmal in einem früheren Promotionsverfahren angenommen oder als ungenügend beurteilt.

Hamburg, den 03/10/2019